UCLouvain

epl

École polytechnique de Louvain

Nanoparticles for paper-based biosensors and environmental impact assessment

Author: **Josquin Vandeputte**
Supervisor: **Jean-Pierre Raskin**
Readers: **Sophie Hermans, Grégoire Le Brun, Julien Mahy**
Academic year 2020–2021
Master [120] in Chemical and Materials Engineering

Acknowledgements

First, I want to thank Prof. Jean-Pierre Raskin, my supervisor, for making this master thesis possible, for his continuous trust and support throughout the year and for his careful listening and constructive comments during and after my endless presentations.

I also want to thank Prof. Sophie Hermans for accepting to be part of my jury, for having welcomed me in her laboratories so easily and for the wonderful collaboration that I hope will continue in the future.

I sincerely want to thank Grégoire Le Brun for involving me in his thrilling research, for his immeasurable support, availability and contagious enthusiasm from day one, and for his constructive feedback. It was a real pleasure to work with him, especially while watching cycling races. I wish him all the best with his biological friends and in Barcelona and I hope he will go through the project at the end of his PhD.

I also want to express my dearest gratitude to Julien Mahy for his invaluable support in the laboratory, for teaching me so many things from his research experience, for his excellent and rapid feedback, and for his patience and availability throughout the year. I wish him all the best in his future projects and I sincerely hope he will enjoy it.

I warmly thank Margo Hauwaert for her help and encouragement throughout the year and for her feedback when writing my thesis. I wish her all the best with her PhD and hope she will enjoy it as much as her master thesis.

I want to express my gratitude to Tommy Haynes for all these precious hours spent at the TEM and for his help in the lab.
I also thank Delphine Magnin for the SEM images and for her enthusiasm for our project.

I want to thank Noan Nivarlet for his advice and his generosity regarding the supply of the material, Prof. Laurent Francis for the "master thesis follow-up" sessions, Clara, Ramy, Roselien, Romain and Rafael for the pleasant atmosphere that prevailed in the lab and during the afterworks and Louise Lejeune for her nice entertainment in the lab and during the writing of this thesis.

I am also thankful to Prof. Alain Jonas, coordinator of my master program, for his help regarding my enrollment to the FAME+ master and when I was in Darmstadt.

Last but not least, I warmly thank my fantastic parents and my three fantastic sisters for their unconditional support from the first to the last day of my studies. I could never have done it without them.

Abstract

Along with climate change, population growth and intensive agriculture, water pollution is responsible for the 2.4 billion people living in water shortage areas. In such places, frequent water quality assessments are crucial to identify, control and prevent water sources contaminated with infectious diseases. To meet this need, point-of-care biosensors have the potential to bring rapid, inexpensive, and precise detection of hazardous contents in water samples. The power of such tests has been recently evidenced by the COVID-19 pandemic since they are the only reliable autotests available on the market.

The project that led to this master thesis aims at developing paper-based biosensors for bacteria detection in remote area water samples. To this end, nanoparticles are used to detect the presence of such harmful organisms and send a signal to the user. Their unique properties significantly improve the performance of the tests and allow for quantitative bacteria sensing in water samples.

In this work, gold and magnetic nanoparticles are investigated to open new electrical and magnetic detection opportunities for paper-based biosensors. Both were successfully synthesized, characterized, compared with commercial samples, and made ready for further conjugation with bioreceptors. Hybrids of both nanoparticles revealed very promising properties in terms of further detection possibilities. Furthermore, the analysis of the microfluidic behavior of nanoparticles in different papers revealed important non-specific binding with the fibers.

Finally, to anticipate the adverse effects of such biosensors on human health and ecosystems when produced on an industrial scale, the environmental impacts of the papers, nanoparticles and plastics used were assessed at large scale. Nanoparticles were observed not to be the most impacting component of the biosensor and to only have significant toxic effects at very high concentrations. In addition, eco-design solutions were proposed to push the biosensors towards a more responsible solution to the urgent situation of global water scarcity.

Acronyms

γ-Fe$_2$O$_3$ Maghemite.

Ab Antibody.

AC Adhesive Card.

AgNP Silver Nanoparticle.

AH Ammonium Hydroxide.

AP Absorbent Pad.

AuNP Gold Nanoparticle.

BSA Bovine Serum Albumin.

CED Cumulative Energy Demand.

CFU Colony-Forming Unit.

CL Control Line.

CNP Carbon Nanoparticle.

CP Conjugate Pad.

DA Detection Area.

DI Deionized.

DLS Dynamic Light Scattering.

DNA Deoxyribonucleic Acid.

EDX Energy-dispersive X-ray Spectroscopy.

EIS Electrical Impedance Spectroscopy.

EoL End-of-Life.

EtOH Ethanol.

Fe$_3$O$_4$ Magnetite.

FTIR Fourier-Transform Infrared Spectroscopy.

GMR Giant Magnetoresistance.

HAuCl$_4$ Gold Precursor.

HC Housing Cassette.

Ig Immunoglobin.

LB Latex Bead.

LCA Life-Cycle Assessment.

LFA Lateral Flow Assay.

LoD Limit of Detection.

M Membrane.

MB Membrane Backing.

MFM Magnetic Force Microscopy.

MNP Magnetic Nanoparticle.

MNP @AuNP Magnetic Nanoparticle covered by Gold Nanoparticles.

MNP @SiO$_2$ Magnetic Nanoparticle coated with Silica.

MNP-CP Magnetic Nanoparticle synthesized by direct Co-Precipitation.

MNP-H Magnetic Nanoparticle synthesized by Hydrothermal method.

MNP-TD Magnetic Nanoparticle synthesized by Thermal Decomposition.

MPQ Magnetic Particle Quantification.

MR Molar Ratio.

NaCt Sodium Citrate.

NC Nitrocellulose.

NP Nanoparticle.

OD Optical Density.

PCR Polymerase Chain Reaction.

PoC Point of Care.

QD Quantum Dot.

RL Release Liner.

ROS Reactive Oxygen Species.

SEM Scanning Electron Microscopy.

SiO_2 Silica.

SP Sample Pad.

SPGE Screen-Printed Gold Electrode.

SPR Surface Plasmon Resonance.

SQUID Superconducting Quantum Interference Device.

TEM Transmission Electron Microscopy.

TEOS Silica Precursor.

TL Test Line.

TMR Tunnel Magnetoresistance.

UCNP Upconverting Nanoparticle.

UV-Vis Ultraviolet-Visible.

VFA Vertical Flow Assay.

WHO World Health Organization.

XPS X-ray Photoelectron Spectroscopy.

XRD X-ray Diffraction.

Contents

Introduction

Water scarcity means insufficient availability of water sources to meet the water demands within a region [1, 2]. In 1980, over 900 million people were living in water-scarce areas. In 40 years, this number has dramatically increased to 2.4 billion and is expected to triple by 2030 [3]. Moreover, nearly two-thirds of the population experience severe water shortages during at least one month of the year [4]. Along with climate change, population growth and intensive agriculture, water pollution is one of the main causes leading to this worldwide increasing water scarcity. Pesticides discharged from farms, untreated human sewage and industrial waste all contaminate water sources with harmful bacteria or toxic substances and make them unfit for drinking or even swimming [5]. Therefore, frequent water quality assessments are needed to identify, control and prevent polluted water sources.

Nowadays, most of the techniques for analyzing water quality are laboratory-based, leading to slow (> 1 day) and expensive (> 50 €) tests (e.g. Polymerase Chain Reaction (PCR) tests). Developing countries, where such tests are the most requested, lack the funds to afford such expensive equipment and to train people to analyze water sources several times a week [6, 7]. Instead, the development of low-cost (< 1 €), precise (< 1 CFU/mL)[1], reliable, simple, rapid (< 20 min) and portable (< 1 kg) point-of-care (PoC) tests could provide significant tools to fight water pollution [8].

To this end, paper-based biosensors and especially Lateral Flow Assays (LFAs) are very promising. They are widely used for pregnancy tests and, more recently, for SARS-CoV-2 autotests. Although less accurate than PCR tests (80 vs. 98%), the latter provide cheap and user-friendly interfaces with results in less than 15 minutes, without the need for laboratories or other expensive equipment. The fact that they are the only autotests available to anyone in the current pandemic show the power and potential of LFAs [9, 10]. As a matter of fact, LFAs are one of the few diagnostic tests to meet the ASSURED criteria defined by the World Health Organization (WHO), standing for Affordable, Sensitive, Specific, User-friendly, Rapid and robust, Equipment free and Deliverable to end-users [11–13]. However, SARS-CoV-2 tests provide only qualitative results (Am I infected or not?) while quantitative results (How bad is my water polluted?) are crucial for water quality assessments. Indeed, the level of contamination admitted in water varies according to the local legislations, the intended use of the water (drinking, swimming, ...) and the harmful character of the bacteria or toxic substance [14, 15].

Such qualitative and quantitative analyses are enabled by integrating nanoparticles (NPs) to LFAs [7, 16, 17]. In a simplified way, they detect the presence of the targeted contaminant and, if so, they send a signal to make the user aware of it. Taking pregnancy or SARS-CoV-2 tests as an example, the red lines indicating the positive or negative result represent in reality high concentrations of red nanoparticles sending an optical signal to

---

[1] CFU stands for colony-forming unit and is used to estimate the number of viable bacteria in a sample.

the user. Nanoparticles are the main signal transducer of LFAs and are therefore the key component to improve the detection performance of such tests, both qualitatively and quantitatively [16, 18]. At this day, their integration to PoC biosensors still requires a lot of research to obtain a quantitative test usable on the field, adaptable to different local legislations and with the same accuracy as laboratory detection techniques.
Although nanoparticles and LFAs offer promising advantages for water quality analyses, their environmental impact is not negligible. Indeed, nanoparticles are not always harmless and excessive use of these can lead to toxic effects on health and ecosystems. Moreover, since LFAs are for single use, they produce significant amounts of waste. Hence, eco-responsible strategies have to be integrated at the design level of the biosensors to anticipate adverse consequences on the environment.

This master thesis fits within the development of a low-impact paper-based biosensor for bacteria detection in remote area water samples, representing the PhD thesis of Grégoire Le Brun. In particular, the aim of this study is to better understand the role of nanoparticles in such biosensors. To this end, different nanoparticles are synthesized and characterized in order to open new detection opportunities for quantitative LFA-based analyses. Furthermore, their microfluidic flow in LFAs is analyzed to study their behavior in paper microstructures. Finally, on a larger scale, the environmental impacts of the papers, nanoparticles and plastics used in LFAs are assessed to identify which are the most affecting components for future industrial production.

The first chapter of this thesis gathers a state of the art about the use of nanoparticles in LFAs, as well as the most recent uses of LFAs for biosensing applications. Then, after outlining the objectives of this study in details, the materials and experimental procedures used to reach these goals are presented. The results followed by a discussion are then addressed in the fourth and fifth chapters, respectively. The sixth chapter reports an assessment of the environmental impacts of 1 million LFAs. Finally, a general conclusion and perspectives are presented to close this master thesis.

Chapter 1

State of the art

In this first chapter, the main concepts used in this study are established. First, the working principle and the different components of lateral flow assays (LFAs) are presented. Then, the use of nanoparticles in biosensors is introduced, covering the different detection methods they offer and how they can be integrated to the tests. Finally, gold and magnetic nanoparticles for LFA applications are discussed in more detail.

1 Lateral Flow Assays

Biosensors are analytical devices that couple bioreceptors and a signal transducer to provide information on the potential presence of a target analyte. The so-called target analyte groups many different substances potentially hazardous to health or to the environment, ranging from contagious viruses in a patient to the presence of heavy metals in water. Biosensors have a wide range of applications in these areas. One very interesting property is to integrate them into portable platforms for early and easy diagnostics. Such devices providing fast analysis and accurate diagnostics near the patient are known as Point of Care (PoC) tests. The main goal is to make them user-friendly and as simple as possible such that anyone could use it, with or without any medical or laboratory knowledge [11,19]. This is especially important in developing countries where laboratories, equipment and training people are too expensive [6, 7].

The World Health Organization (WHO) recommends that PoC biosensors adhere to the ASSURED criteria, standing for Affordable, Sensitive, Specific, User-friendly, Robust and Rapid, Equipment-free and Deliverable to end-users [12, 20]. As a matter of fact, paper-based biosensors are one of the best PoC devices corresponding to this criteria, from clinical to environmental applications [16]. Indeed, paper is abundant, cheap, light, easy to manufacture and biocompatible[2]. Moreover, paper is recyclable, which is very attractive for designing low-impact biosensors. The material is usually made of cellulose fibers leading to a porous microstructure and thus a high surface-to-volume ratio. This provides a capillary force to pump the sample through the strip, without the need of any external device [7, 11].

Among all the different types of paper-based biosensors, Lateral Flow Assays (LFAs) are best suited for bacteria detection in water. They respond to the ASSURED criteria as they provide specific and sensitive signals while being low-cost, easy-to-use, robust, relatively fast (5-20 minutes) and requiring low quantity of sample volume (typically from

---

[2] Biocompatibility is very important because it means that the specific bioreceptors detecting the target analyte can be easily immobilized. This will be clarified in the next sections.

femto- to milliliter). Moreover, because of the long shelf life and because they do not need to be stored in refrigerators, LFAs are very well adapted for use in developing countries, remote regions and even battlefields [7, 11].

One famous example of LFA is the pregnancy test, which is nowadays the most used PoC paper-based biosensor in the world [7, 16, 21]. More recently, LFAs are available in all pharmacies for SARS-CoV-2 detection. They are currently the only autotests available for this coronavirus. This shows how LFAs can revolutionize health care and disease prevention in both developing and developed countries. As shown in Figure 1.1, the interpretation of such tests is straightforward: a negative result is indicated by one red line and a positive one by two red lines.

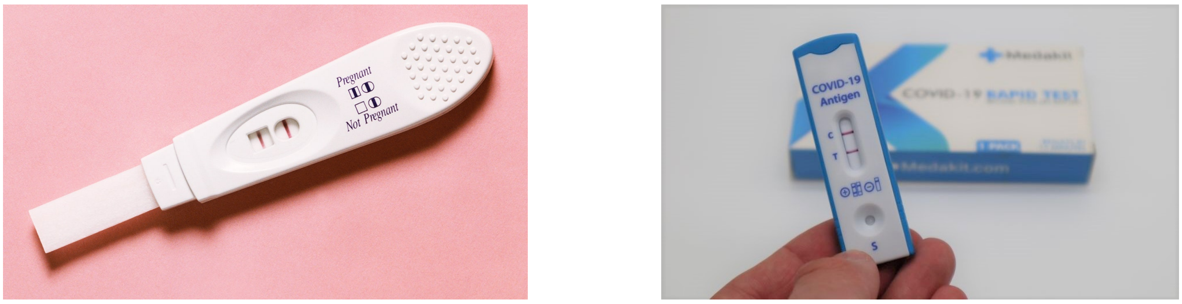

(a) (b)

Figure 1.1: Two examples of commercial LFAs: (a) a pregnancy test, (b) a SARS-CoV-2 test. Both tests are positive here.

The red lines are in reality made of very high concentrations of red nanoparticles that cannot be distinguished individually with the naked eye. These labels bind to the target analyte, which subsequently bind to the immobilized bioreceptors at these lines, thereby inducing a red color. This will be discussed in depth in the following section. Nanoparticles (NPs) are the main signal transducers of LFAs. They have unique properties making them very attractive for such tests. They can provide other colored signals but also electrical, magnetic or fluorescent signals. They are key components to improve the detection performance of biosensors.

1.1 General working principle

Lateral flow assays are usually composed of four overlapping paper-based pads called sample pad (SP), conjugate pad (CP), membrane (M) and absorbent pad (AP). Each pad has its own role and can be made of a different paper, given the application of the LFA. Generally, the sample and absorbent pad are made of cellulose, the membrane is made of nitrocellulose and the conjugate pad is made of glass fiber pre-stored with the label particles.

Standard LFAs The working principle of standard LFAs (also called sandwich assays) is shown on the left-hand side of Figure 1.2. The sample is initially loaded on the sample pad and flows through the different pads due to capillary forces. The conjugate pad is initially loaded with labelled bioreceptors which will recognise the target analyte if present in the sample.[1]

---

[1] As explained in the next sections, there are many different bioreceptors used in LFAs. In this study, we will focus almost exclusively on antibodies. Hence, the tests should be rigorously called lateral flow immunoassays (LFIA) but to make the explanations clearer, the general from “LFA” was kept.

Afterwards, the sample flows through the membrane (also called detection pad) and reaches the test line (TL). The test line is initially made of capture antibodies (Ab), used to immobilise the target analyte already attached to the label to form a so-called “sandwich” (Ab-analyte-Ab-NP). If the sample does not contain any target analyte, it will simply flow by the test line towards the control line (CL).
Similarly, the CL is initially composed of control antibodies, which are not specific to the target analyte but to the detection antibodies on the labels. Hence, whether the sample contains analyte or not, the control antibodies will anyway immobilise the labels at the CL, thereby validating that the test worked correctly. For pregnancy and SARS-CoV-2 tests, red label particles are used and gradually accumulate at the TL and CL as the sample flows through the test. Consequently, positive samples (*i.e.* containing the target analyte) will show two colored lines, while negative samples exhibit only one line at the CL.
Finally, the role of the absorbent pad is to have an extra wicking force, such that the more sample and thus more analyte flows through the test and control lines, thereby improving the sensitivity of the test [7, 16].

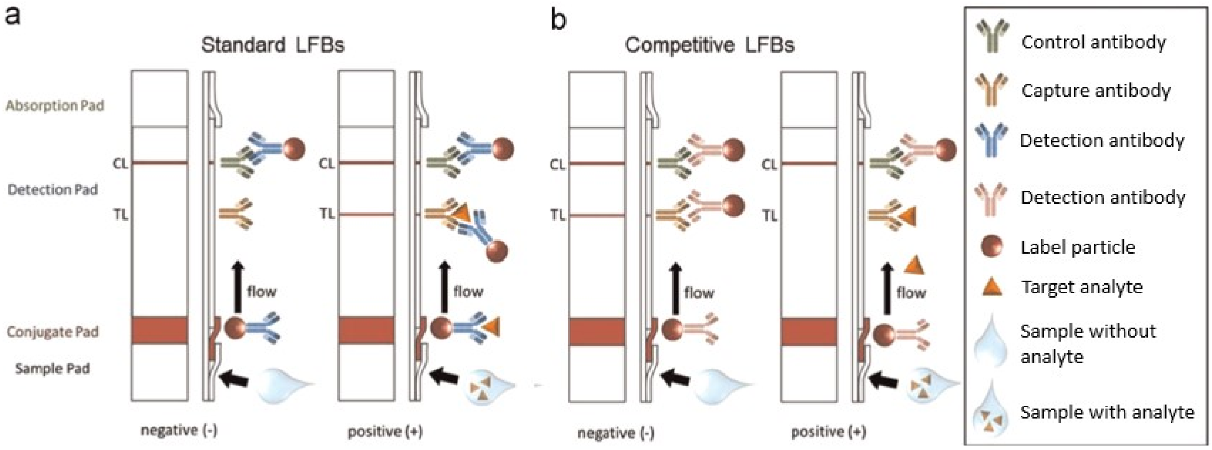

Figure 1.2: General working principle of LFAs: standard assay (left-hand side), competitive assay (right-hand side). The term LFBs used here means lateral flow biosensor and refers to the same principle as LFAs [7]

Competitive LFAs As it can be seen in the right-hand side of Figure 1.2, another type of LFA called competitive assay exists. The working principle is similar except that the TL does not contains capture antibodies but is already immobilized with the target analyte. Hence, if the latter is present in the sample, the conjugated labels will already be attached to the analyte from the sample. Thus, the labels will not attach the target analyte at the TL. A competition between both target analyte takes place. In this case, in contrast to standard assays, positive samples yield only one line.

The advantage of standard LFAs is that the signal produced is proportional to the amount of target analyte in the sample. Nevertheless, as it must be able to bind simultaneously to both the detection and the immobilized antibodies, small analyte molecules such as drugs or toxins might have some problems to bind to two antibodies. Additionally, steric hindrance may prevent this simultaneous binding. Hence, competitive assays are particularly useful for small analytes [16, 17, 22].
As this study covers detection of bacteria in water, the sample is not limited and the analyte is large (0.5-5 μm). Hence, standard assays are preferably chosen.

1.2 Use of LFAs

Lateral flow assays can be used for the detection of many analytes, including animal diseases, pathogens, chemicals, toxins and water pollutants. These targets have been efficiently detected in many different biological samples such as water, urine, saliva, sweat, serum, plasma, blood and many other fluids [13, 21–27]. At this day, LFAs are mainly used in veterinary medicine, hospitals, quality control, product safety in food production, and environmental health and safety.

As already mentioned, the latest application of LFAs is the detection of the SARS-CoV-2 virus. These tests are less accurate than polymerase chain reaction (PCR) tests (80 over 98%) but the fact that the patient can test him-/herself and get a result after maximum 30 minutes without the need of any laboratory makes them very interesting. In particular if someone feels typical symptoms but has to go somewhere, he/she can use this kind of test as a first check to reduce the risk of contamination [9, 10].

1.3 Components of LFAs

The different components of LFAs are described hereafter. Their main characteristics and the materials they are usually made of are discussed. All the pads are represented schematically in Figure 1.3.

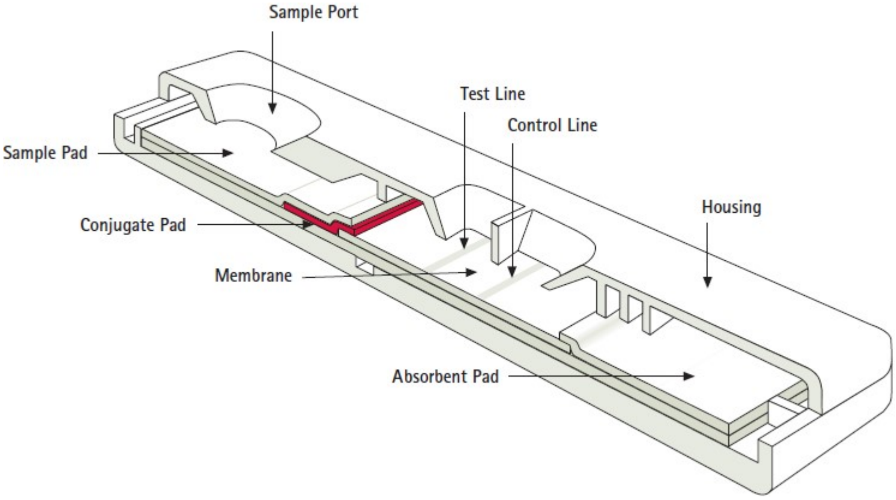

Figure 1.3: Schematic structure of a lateral flow assay with the different pads [28].

1.3.1 Sample pad

The assay starts when the sample is loaded onto the sample pad from the sample port in Figure 1.3. The main functions of the SP are to ensure a constant flow throughout the test, guarantee reproducible measurements and homogenize the buffer conditions of the sample [17].

Characteristics There are three key parameters to play with for the design of the sample pad. First, the *bed volume*, *i.e.* the volume v of air contained in the pad, can be linked to the amount of liquid required to wet the pad by multiplying the total volume of the pad V times the porosity of the fibrous material f, such that $v = Vf$. This property is important for determining the amount of sample that flows in the LFA.

Similarly, the *thickness* of the pad, sometimes called caliper, not only affects the bed volume but also the consistency of the pad. Indeed, a thicker pad provides a slower and more stable flow, as well as higher buffering capabilities.
Finally, the sample pad should also match the *desired particle retention rating*, referring to the particle size that the sample pad is able to retain and thus allowing a filtration of the sample [17].

Materials The materials used for sample pads are generally cellulose or woven meshes. Sample pads made of *cellulose* or *cotton fiber* tend to be thicker (> 250 μm) and cheaper, but are weaker for handling, especially when wet. They have bigger bed volumes (> 25 μL/cm^2) and have higher tolerance the chemicals present in the sample pad buffer.
Sample pads made of *woven meshes* such as glass fibers have a good tensile strength and provide an even distribution of the sample over the conjugate pad. They can also act as filters for removing chemicals from the sample. Their low bed volumes (≤ 2 μL/cm^2) make it possible to retain minimal amounts of sample but they are more expensive and their cutting is more difficult than cellulose.
For target analyte in the micron size range like bacteria, it is recommended to consider a high bed volume to allow them to flow through the strip [17].

1.3.2 Conjugate pad

After being loaded onto the sample pad, the sample reaches the conjugate pad (CP), shown in red in Figure 1.3. The three main functions of the CP are to preserve the dried conjugated nanoparticles, release them upon wetting by the sample and finally provide the first interaction between the labeled antibody and the target analyte. Its preparation is one of the most critical stage during the fabrication of the strips [17].

Characteristics The conjugate pad has three very important characteristics to be considered. First, it should provide *low non-specific binding* such that neither nanoparticles nor target analyte remains in it. Second, it should provide a *consistent flow and bed volume* to keep a homogeneous and reproducible flow towards the membrane. Finally, the CP should also have a *good mechanical strength* to resist the fabrication process and contain *no extractable material* that could potentially block the membrane or contaminate the sample [17, 28].

Materials The main material used for conjugate pads is glass fiber because it corresponds the best to the desired characteristics mentioned above. Other materials such as cellulose and polyester have also been reported in the literature [17].

1.3.3 Membrane

The membrane (M) is where the signal is emitted by the labels (e.g. nanoparticles), as shown in Figure 1.3. Its main function is to facilitate a homogeneous flow, support the immobilized antibodies for capturing the analyte target and show low non-specific binding [17].

Characteristics Membranes are generally characterized by their *capillary flow time*, representing the time required for the sample front to cover the membrane length and expressed in s/4cm (since 4 cm is the general length of the membrane). This parameter depends on many parameters such as the *pore size* (*i.e.* the diameter of the largest pore

in the flow direction), the *pore size distribution* (*i.e.* entire range of the pore sizes through the microstructure, generally between 0.5 and 5 μm) and the *porosity* (*i.e.* ratio of air to material). The pore size distribution affects the capillary flow time the most. Indeed, the lower the pore size distribution, the higher the capillary flow time and thus the slower the sample flow speed.
Consequently, low capillary flow times increase the probability of interaction between the immobilized antibodies and the labelled conjugates, and thus increase the sensitivity of the test. This characteristic is crucial as it affects the sensitivity and consistency of the assay. Once the analyte has passed the immobilized antibodies, it cannot bind to it anymore as the flow is forced to evolve in one direction only. Nevertheless, low capillary flow times also increases the chance for non-specific binding in the membrane.
Another important characteristic of the membrane is its *protein binding capacity*, related to the irreversible grafting of the capture and control antibodies on the membrane at the test and control lines. It is determined by the amount of surface area available for Ab immobilization [17, 28].

Materials Nitrocellulose (NC) is most often used for the membrane due to its relatively low price, strong electrostatic binding to antibodies (for the TL and CL) and different capillary flow times available [17]. Other materials have also been reported, such as polyvinyldiene fluoride (PVDF), nylon or polyethersulfone (PES) [28].
Nitrocellulose is very difficult to handle and is thus usually commercially available with a non-porous polyester backing of 50 or 100 μm thick, increasing the mechanical strength of the membrane without affecting its microfluidic properties. The polyester film also acts as a barrier to chemical contamination from the adhesive card used to assemble the different pads together [28].

Striping with antibodies The placement of the test and control lines is crucial for a good sensitivity of the test. The further the localization of the TL on the membrane, the slower the speed of the sample at the TL. The *capillary flow rate* (expressed in s/cm, different from the capillary flow time in s/4cm) decreases exponentially with the covered distance of the front from the origin because the difference of pressure between the liquid and the void in the pores decreases as the water front increases. As a slow flow rate means that the probability of binding between the target analyte and the immobilized antibodies is higher, it is advantageous to place the test and control lines far up the strip. This is usually done in LFAs when an absorbent pad is used [28].

1.3.4 Absorbent pad

The main function of the absorbent pad (AP) is to make sure all the labels have reached the end of the strip and passed through the test and control lines. By increasing the total volume of sample entering the test and control lines, it washes the unbound detector particles away from them, thereby lowering the background noise and enhancing the sensitivity [28]. In the absence of the AP, once the front of the flow reaches the end of the strip, it stops and the sample evaporates along the whole strip [17].

Characteristics The main characteristic of the absorbent pad is its *bed volume*. It should be based on the volume of liquid that must pass through the TL and CL [17].

Materials Like sample pads, absorbent pads are most often made of cellulose and cotton fibers [17, 28].

1.4 Assembly of LFAs

Suppose all the labels are already conjugated to the specific bioreceptors, the control and detection bioreceptors are ready-to-use and the different pads have already been cut with the desired length. In this case, a typical step-by-step fabrication method of an LFA is shown in Figure 1.4. Although not extremely complicated, the assembly needs to be performed very carefully to ensure a homogeneous and reproducible flow.

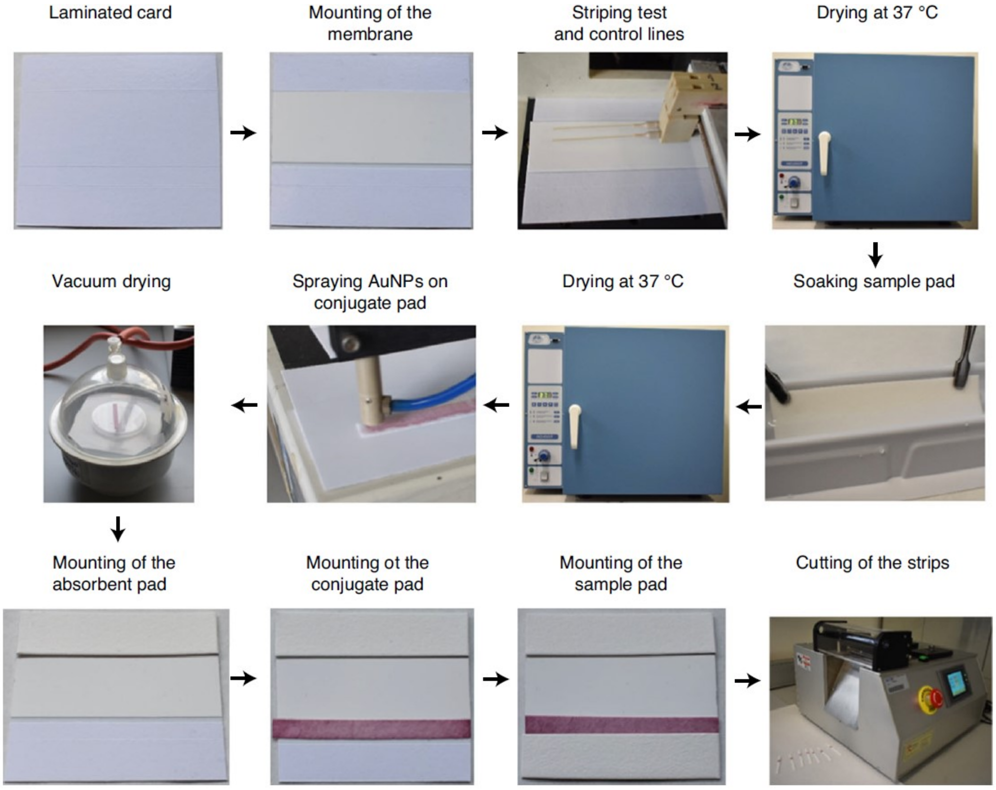

Figure 1.4: Step-by-step method for the assembly of LFA strips [17].

The first step is to place the polyester-backed membrane on the adhesive card (AC, also called laminated card). These are made out of polyester or cardboard paper and contain release liners (RLs) to help position the different pads at the right distance from each other.
Afterwards, capture and control antibodies are immobilised on the membrane to form the test and control lines, respectively, and the membrane is subsequently dried in an oven (the temperature might vary). The sample pad is then soaked in the sample buffer and also dried in an oven.
The next step is the spraying of the labels on the conjugate pad, which is dried in vacuum this time. This step is crucial for the good performance of the LFA. Once all the pads are ready-to-use, the absorbent pad is first placed on the membrane with a certain overlap (typically 2-4 mm), followed by the conjugate and sample pad. These overlaps have to be consistent in order to get a uniform flow.

The alignment of the different pads is very important to get reproducible tests. In large-scale processes, calm-shell laminators are used to obtain a rigorous alignment of the pads on the AC, without compressing the porous structures of the papers. This can also be done by hand at lab-scale but the alignment of the pads might be less accurate.
Once the pads stick together, the master cards are cut into individual strips. This can be done with a guillotine shear mechanism or rotary cutting mechanism. Scissors can also

be used but the consistence and reproducibility of the tests will be affected. Finally, it is common to place the strips in a housing cassette that fits their geometry in order to protect the test from any contaminant or mechanical damage and to avoid user mistakes [17].

1.5 Architectural enhancement methods

The working principle detailed in the last sections is quite straightforward. Although it already works very well and gives good qualitative results, it is possible to easily obtain much better sensitivities by playing with the architecture of the tests. There are many enhancement methods reported in the literature and playing with the architecture of the assays. The most interesting ones for bacteria detection in water samples are presented below.

Parolo *et al.* [6] made very simple changes in the size of the different pads to increase the sensitivity of the LFAs. They suggested that there are two opposite effects influencing the sensitivity of the assay when playing only with the sample pad. Although a bigger sample pad increases the volume of sample and thus the mount of analyte going through the test and control lines, it also increases capillary flow rate significantly, reducing the probability of binding between the conjugated labels and the immobilized antibodies.
While increasing the area of the sample pad 3 times led to lower sensitivities (more analyte but flow rate way too high), increasing it 2 times led to slightly better sensitivities. Moreover, when both the area of the sample and conjugate pad are increased, not only the amount of analyte to-be-detected is increased but also the number of labels (gold nanoparticles here) to-be-used. Hence, as shown in Figure 1.5a, increasing the width of the sample and conjugate pad 2 and 3 times led to limits of detection (LoD) of 1.83 ng/mL and 0.7 ng/mL, respectively, thereby reaching an 8-fold improvement of the LoD in the latter case.

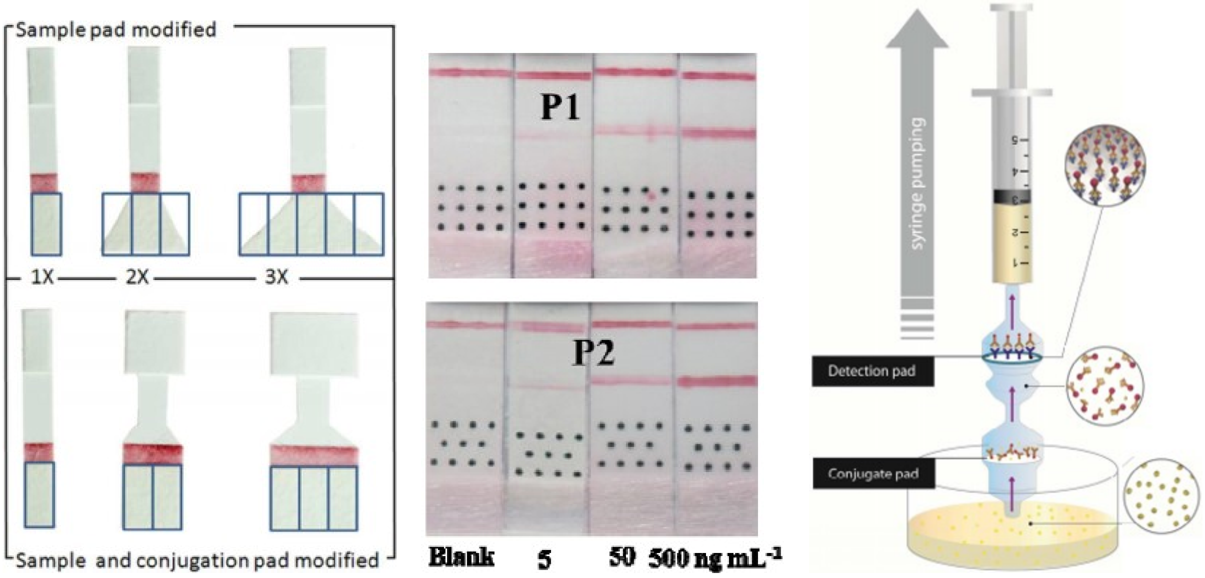

(a) (b) (c)

Figure 1.5: Different enhancement methods playing with the architecture of the LFA: (a) increase of the sample pad width and both the sample and conjugate pad width [6], (b) addition of wax pillars between the conjugate pad and the test line [29], (c) vertical flow assay [30].

Nunes Paulie *et al.* [30] revisited the LFA working principle by making a vertical flow assay (VFA), where the sample is pumped across the different pads with a syringe, as represented in Figure 1.5c. The sample is first pumped to the conjugate pad where the analyte interacts with the pre-stored labels during a few minutes. Then, it is pumped to a circular detection pad made of NC where the signaling takes place. Although this technique requires much more liquid sample than standard LFAs (around 6 mL compared to 200 μL, which is not a problem when dealing with samples like water), VFAs provide simple and sensitive tests which enable analysis of much greater sample volumes. The use of larger sample volumes translates to lower LoDs in shorter analysis times (around 13 minutes). Indeed, the higher the sample volume processed, the greater the amount of analyte interacting with the conjugated labels and consequently, the higher the analytical signal. Moreover, no sample and absorbent pads are needed.

2 Nanoparticles

Nanoparticles (NPs) determine the analytical performance of LFAs. They are used as labels which, when conjugated to bioreceptors (e.g. antibodies), can interact with the target analyte (bacteria, metals, DNA, viruses, ...). When further concentrated at the TL and CL, they generate a signal whether the tested sample contains the analyte or not. They are the main signal transducers in LFAs. Depending on the NP, this signal can be colorimetric (like pregnancy or SARS-CoV-2 tests) but also electrical, magnetic or fluorescent for example, as it will be discussed hereafter. NPs are the keys to obtain high sensitivities and low LoDs [16, 19].

Nanoparticles can adopt different shapes that can be classified by spatial dimension: 0D (spherical), 1D (e.g. nanotubes and nanowires), 2D (e.g. graphene) and 3D (e.g. nanoprisms and nanoflowers) [19, 31].
In this study only 0D spherical nanoparticles with diameters ranging from 5 to 200 nm are considered because they offer many advantages for LFA applications. Their small size reduces the risk of clogging the pores of the paper, provided that they do not form large aggregates. They are also easier to synthesise and bio-conjugate [31–35].

2.1 Nanoparticle-based detection methods

Many different detection methods have been successfully implemented on LFAs. They rely on the specific properties of different nanoparticles. The most widespread ones are discussed in the following sections.

2.1.1 Colorimetric detection

Colorimetric detection is the most popular method because the reading can be performed with the naked-eye, without any external reader, making the test more affordable and user-friendly. The most famous LFAs using colorimetric detection are pregnancy and SARS-CoV-2 tests. As explained earlier, the result is positive if the test and control lines are red. This red color is due to the high concentration of a certain type of nanoparticles at this place of the membrane.
There are many different NPs scattering a certain color for colorimetric detection. The most famous ones are gold nanoparticles (AuNPs) because they exhibit an intense red color which is the most distinguishable by naked-eye. Their properties will be largely discussed in section 2.3. Many other NPs exhibiting different colors have also been used in LFAs such as black carbon nanoparticles (CNPs) [36–40] or brown magnetic nanoparticles (MNPs) [41]. In addition, latex beads (LBs), usually made out of polystyrene, can also be used for colorimetric and fluorescence detection, depending on the dyes and fluorophores they are loaded with (see section 2.1.2). They can exhibit different colors such as blue or red [16, 42–44]. Figure 1.6 shows two types of colorimetric LFAs using different NPs and consequently exhibiting different colors at the test and control lines.

The result brought by colorimetric tests is for sure qualitative (Am I pregnant or not?) but can also be semi-quantitative. The color intensity can be indeed related to the analyte concentration, similarly to pH strips. This semi-quantitative response can further be improved with the help of colorimetric readers or even smartphones. You *et al.* [45] have developed user-friendly apps for smartphones to translate the signal from the TL and CL meanwhile all the steps that the user should perform are explained on the smartphone's screen.

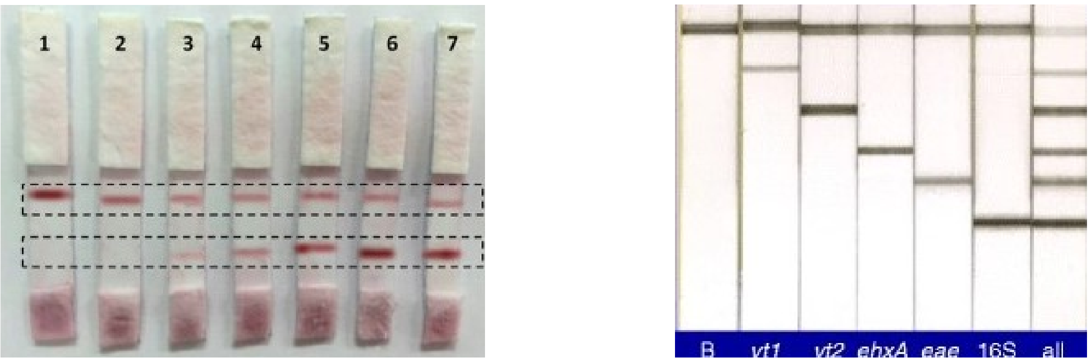

(a) (b)

Figure 1.6: Two types of colorimetric LFAs using different labels: (a) AuNPs [46] and (b) CNPs [36], both for the detection of different bacteria

2.1.2 Fluorescent detection

Another way to detect bacteria in LFAs is to use fluorescent nanoparticles. The most famous ones are quantum dots (QDs). QDs are semiconductor nanocrystals composed of III–V or II–VI elements with a size of approximately 1–10 nm [47]. Their inherent photoluminescent properties arise from a phenomenon called "quantum confinement". Semiconductors are materials characterised by a narrow band gap energy lower than 5 eV, which, for intrinsic semiconductors, separates the full valence band and the empty conduction band (filled with electron holes). When a semiconductor absorbs a photon of higher energy than its bandgap, an electron from the valence band is excited to the conduction band, creating subsequently a hole in the conduction band. These electron and hole are then attracted to each other and form a bound state called exciton [48, 49].

The preferred electron-hole separation distance is called exciton Bohr radius and depends on the material properties (equal to ∼5 nm for CdSe as an example). When the nanocrystal size becomes smaller than the exciton Bohr radius, the electron and hole are held closer to each other, increasing the exciton binding energy, which is correlated to the emission wavelength of the nanocrystal [50–52]. The wavelength of the emitted spectra, and thus the color observed, can be tuned by varying the size of the QD, as shown in Figure 1.7a for CdSe nanocrystals. Another way to tune the emission wavelength is to play with the composition of the QD [50].

Although QDs are mostly used for fluorescent detection in LFAs, there are other fluorescent materials such as upconverting nanoparticles (UCNPs). These larger nanoparticles contain rare earth elements to give them their fluorescent properties [54].

Fluorescent nanoparticles exhibit a much more sensitive response and a lower LoD than colorimetric NPs [16]. Bai *et al.* [53] have compared the performances of colorimetric detection using AuNPs and fluorescent detection using silver nanoparticles (AgNPs) of 38.5 nm of diameter on average loaded with CdTe QDs. As shown in Figure 1.7b, the LoD of the conventional AuNP-based LFA was 20 ng/mL of analyte (α-fetoprotein), while the LoD of the fluorescent assay was 2 ng/mL of analyte.

However, fluorescent detection methods require additional devices for the excitation of the NPs and for the reading of the signal. This makes their application to PoC devices more challenging [7, 55].

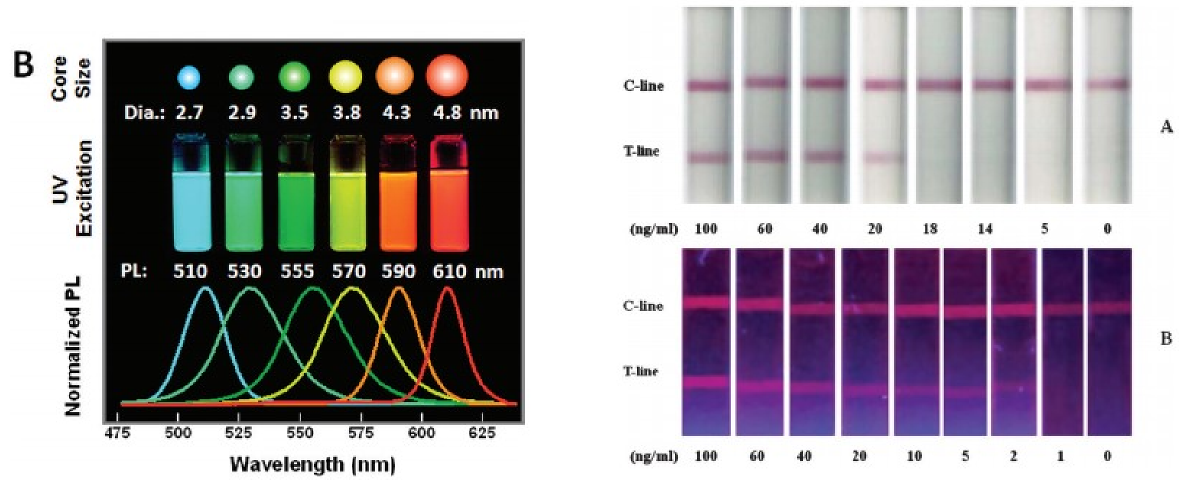

(a) (b)

Figure 1.7: (a) Progressive color changes of CdSe/ZnS core-shell structure with increasing nanocrystal size [50], (b) Comparison of LFAs made with AuNPs (up) and AgNPs loaded with QDs (down) [53].

2.1.3 Electrochemical detection

Coupling electrochemistry with LFAs provides fast, quantitative, sensitive and relatively inexpensive detection. Although robust measurement equipment and transducers are required, they are most often easy to miniaturize. There are already many point-of-care electrochemical devices well established on the market [56]. Electrochemical LFAs rely on the detection and quantification of an electrochemical transducer or the conductive bridge formation between electrodes. The electrodes can either take the form of gap electrodes or screen printed electrodes on the membrane [57].

Many conductive nano-compounds can be suited for electrochemical detection, among which metallic NPs such as silver or gold or organic conductive polymers are the most used. They are gathered in Table 1.1. The electrochemical methods can be classified according to the measured parameter: current (amperometry), potential (potentiometry), resistance (conductometry) or impedance (impedimetry).

In conductometric detection, the conductance (initially equal to 0) is measured after application of the sample. Muhammad-Tahir *et al.* [58] have developed a conductometric LFA using silver gap electrodes. By measuring the resistance R with a multimeter, the conductance C was calculated as $C = 1/R$. As shown schematically in Figure 1.8a, they used polyaniline-antibodies complexes to form a bridge between the electrodes and generate a signal. In 2 to 10 minutes, their biosensor could detect a specific bacteria at an average concentration of 79 CFU/mL.

Impedimetry is an electrochemical-based detection method relating changes in the impedance of the system to the number of bacteria present at the measured area. It uses Electrical Impedance Spectroscopy (EIS). To cut a long story short, a cyclic function of small amplitude and variable frequency is applied on the transducer and the resulting current is used to calculate the impedance for the whole frequency spectrum. The amplitude of the current and potential signals in addition to the resulting phase difference between voltage and current, which depends on the nature of the system under study, dictates the system impedance [59, 60]. Sinawang *et al.* [59] conjugated ferrocene as a redox label with

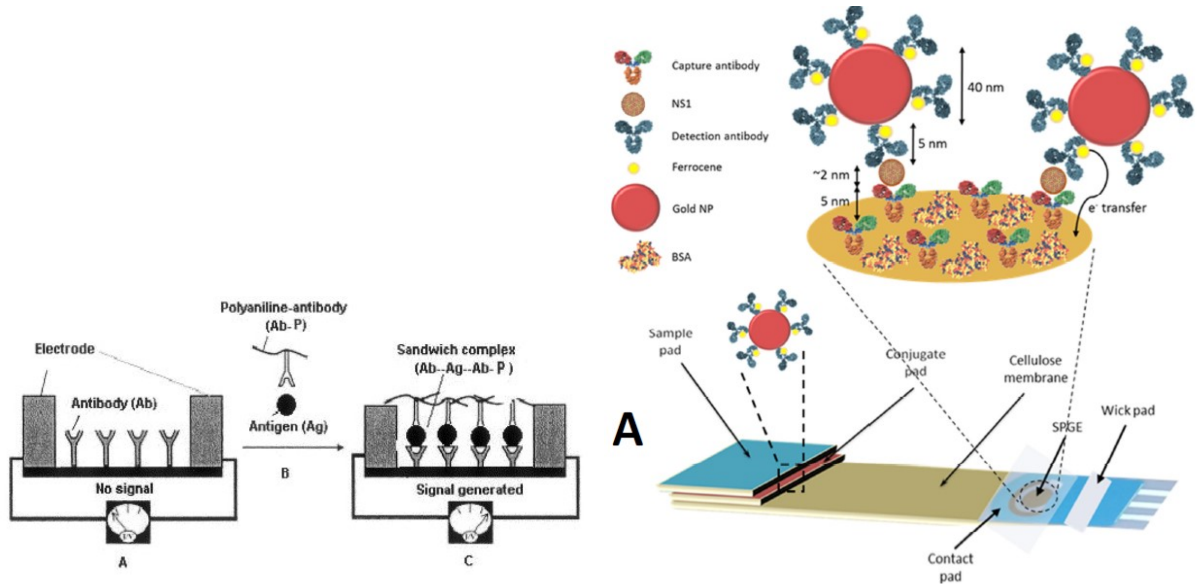

(a) (b)

Figure 1.8: (a) Sectional view of the membrane from a conductometric LFA using polyaniline to form a bridge between the two electrodes [58], (b) Schematic representation of the impedimetric LFA using ferrocene on AuNPs for labelling [59].

AuNPs of 40 nm for impedimetric quantitative detection of DENV-NS1 protein down to a detection limit of 0.5 ng/mL. The experiment is schematically shown in Figure 1.8b. The screen-printed gold electrodes (SPGE) were bio-functionalized beforehand with specific antibodies.

2.1.4 Magnetic detection

Similarly to electrochemical detection, lateral flow assays can benefit from the magnetic properties of some nanoparticles. Magnetic nanoparticles (MNPs) allow for remote positional control by means of an applied field. This make MNPs very interesting for LFAs, taking advantage of the magnetic properties to pre-concentrate the analyte from several liters to few mL or accumulate them on specific parts of the membrane [16, 61].
More interestingly, the magnetic response of MNPs under a magnetic field can also be measured by a magnetic reader and subsequently transformed into a useful analytical signal. This quantitative detection method has an important advantage over electrochemical detection because biological entities do not show any magnetic behavior or susceptibility. Only MNPs produce a signal, reducing the background noise to almost zero. Moreover, as shown by the red boxes in Figure 1.9, the signal from all the MNPs in the membrane thickness is read, while only NPs at the surface or in contact with the electrodes provide a signal for colorimetric and electrochemical detection, respectively. In addition, the magnetic signals are stable for a longer time than optical signals [7, 16, 18].
Many different magnetic nanoparticles have been reported in the literature. Some of them are gathered in Table 1.1. A more detailed discussion about their properties will be given in section 2.4.

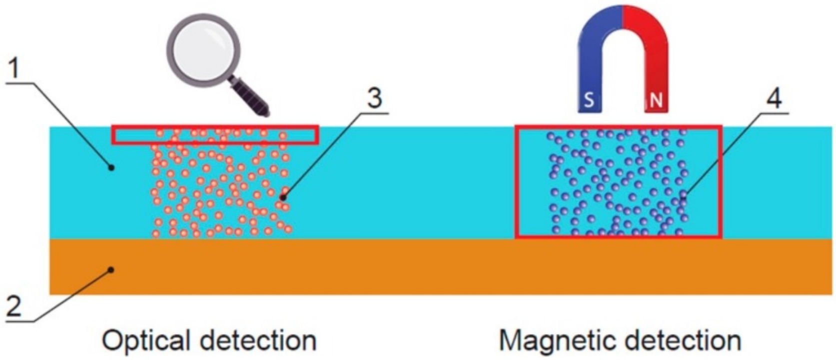

Figure 1.9: Comparison between colorimetric ad magnetic detection in LFAs. The magnetic one detects the NPs in the whole cross section. The blue background represents the NC membrane and the orange represents the backing. Taken from [62].

2.1.5 Thermal contrast detection

In addition to colorimetric and electrochemical detection, metallic nanoparticles can also be optically excited to generate heat. Figure 1.10 shows a schematic representation of thermal contrast detection in LFAs upon laser stimulation. When there are insufficient gold nanoparticles at the test line for a visual contrast, thermal contrast can still detect their presence, with a low-cost laser or light-emitting diode (in green) and an infrared temperature gun (shown as blue box). The mechanism of heat release is very simple: the laser electric field strongly drives mobile carriers inside the nanocrystals, and the energy gained by carriers turns into heat. The heat diffuses away from the nanocrystal and leads to an elevated temperature of the surrounding medium [63].
Qin *et al.* [64] reached a 32-fold improvement compared to visual detection. Although thermal detection increases the sensitivity significantly and shows a stable response over weeks making it a really robust and reproducible technique, the need of laser and infrared camera make it less applicable for PoC devices [7, 16].

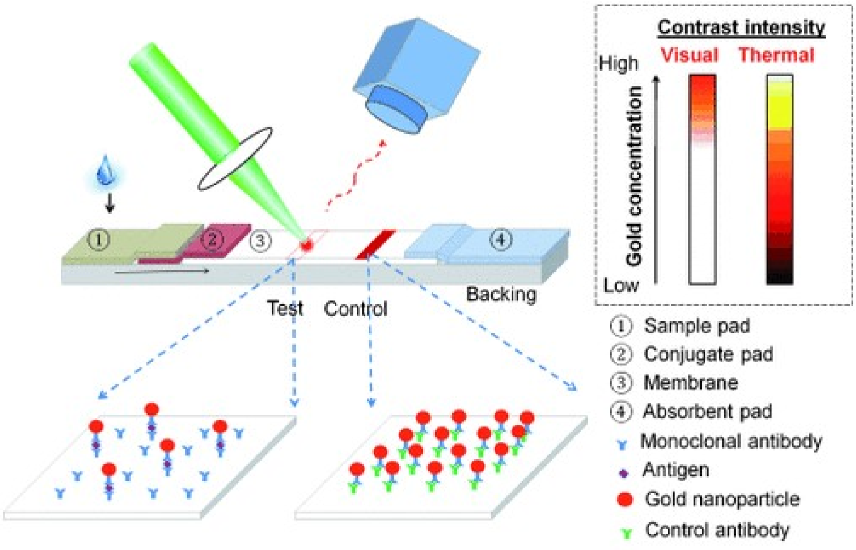

Figure 1.10: Thermal contrast sensor used with LFAs [64].

Table 1.1: The different detection methods of LFAs and their related nanoparticles, based on [7, 16, 17, 65]

Detection	**NP**	**Advantages**	**Drawbacks**	**Ab Conjugation**	**Core size**
Colorimetry	AuNP	Naked-eye detection Fast qualitative response Easy synthesis, Intense color Highly biocompatible, Well-known conjugation methods Relatively stable in time, Tunable size & shape	Only qualitative or semi-quantitative Poor sensitivity and LoD if no enhancement method Expensive if commercially bought	EDC/NHS Adsorption	10-40 nm
	CNP	High signal-to-noise ratio Cheaper, Stable-in-time	Unspecific adsorptions Weaker signal than AuNP	Adsorption	25-500 nm
	Dyed LB	Cheaper, Multiple colors Good sensitivity and LoD	Difficult synthesis, Weaker signal High amount of dye needed	EDC/NHS	200-500 nm
Fluorescence	QD	Good sensitivity and LoD Small size, Strong intensity Stable vs. photo-bleaching	External devices required Hard synthesis and conjugation Toxic, fluorescence quenching	EDC/NHS	1-10 nm
	UCNP	Require less excitation energy Low toxicity, Strong signal	Expensive (rare elements)	EDC/NHS	10-80 nm
Electrochemical	Metallic (Au, Ag, C, ...) Organic NP	Fast, quantitative, inexpensive Very good sensitivity and LoD Cheap & miniaturizable devices	External devices required Electrode reproducibility Toxic (oxidation)		
Magnetic	MNP (Fe_3O_4, Fe_2O_3, FeCo, $CoFe_2O_4$, $ZnFe_2O_4$, ...)	Inexpensive, Pre-concentration Colorimetry also possible, Low background noise, all MNPs provide signal	Magnetic device required Sensitivity $\propto$ particle size	EDC/NHS	5-800 nm
Thermal contrast	AuNP	High improvement of sensitivity and reproducibility High signal-to-noise ratio	Expensive equipment(laser and non-optical reader)		

2.2 Functionalisation of NPs

From the synthesis to the use of nanoparticles in LFAs, there are several steps to be rigorously followed. As shown in Figure 1.11, a primary coating must be applied to the synthesised NPs before attaching them to the bioreceptors, followed in the end by a surface passivation. The synthesis step will not be discussed in this section because it is specific to each type of nanoparticles [66, 67].

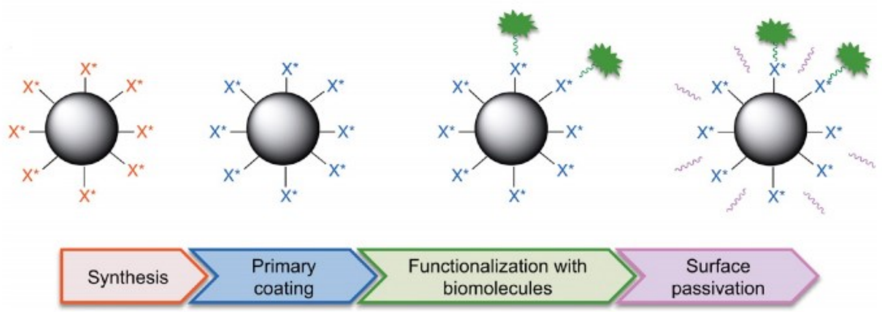

Figure 1.11: Synthetic steps towards usable nanoparticles for LFAs [66].

2.2.1 Primary coating

Water is a highly complex fluid that can destabilize nanoparticles and cause their aggregation through van der Waals interactions. In the case of LFAs, if nanoparticles agglomerate too much, they might not go through the pores of the papers, clog them end consequently falsify the test result. Therefore, an appropriate coating is crucial to obtain NPs with high colloidal stability, preserving their physicochemical properties and defining their interaction with the biological environment. Coating can also provide a flexible surface chemistry for further functionalization with biomolecules and allow for the outer layer of the NP to be engineered for specific biological interactions. The most common strategies for engineering the primary coating of NPs include ligand exchange, silica coating and polymer wrapping. They are schematically represented in Figure 1.12. The choice of a coating strategies is strongly influenced by the nature and initial coating of the inorganic nanomaterial [66].

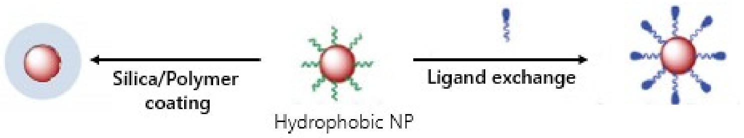

Figure 1.12: Primary coating strategies for nanoparticles, inspired from [66, 68].

The *ligand exchange* between the original surfactants and hydrophilic ligands makes it possible to get stable colloidal NPs in water. The chemical affinity of the ligand for the material and the presence of excess ligand are key parameters for achieving a densely packed ligand shell. The choice of the ligand depends on the composition of the inorganic core [66].

Silica (SiO_2) coating yields water-soluble NPs with good colloidal stability and biocompatibility. Other important advantages include an easy control of the coating process, optical and magnetic transparency, low cost, controlled porosity, and most importantly the presence of functional groups facilitating the further conjugation with bioreceptors [69].

Polymer coating typically uses polymers such as poly(ethylene glycol) (PEG), dextran, and chitosan derivatives, which are highly biocompatible and provide functional groups for further bio-conjugation. Upon cross-linking around each nanoparticle, the NPs become stable in water and can be further functionalized with the biomolecules of interest. Thanh *et al.* [67] have reviewed many different polymers used to coat NPs.

2.2.2 Functionalization with bioreceptors

As previously introduced, nanoparticles are widely used in LFAs because they offer many different detection methods. However, this is not sufficient alone. The specificity of a LFA is dictated by the biomolecules attached to the label that recognize the analyte specifically. Hence, after coating the inorganic core to give adequate colloidal stability and the desired chemical moieties to the NPs, the next step is to bio-conjugate the nanoparticles [70].

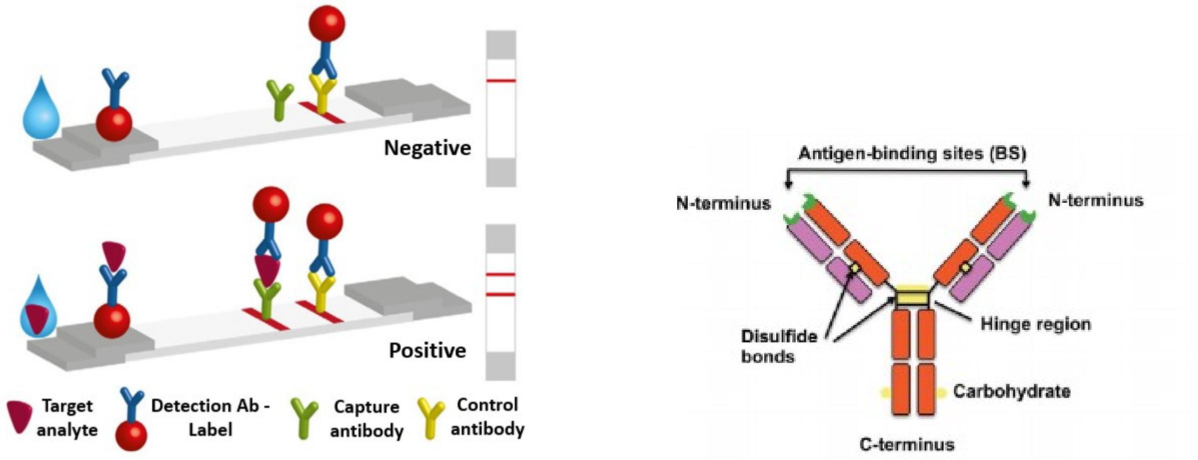

(a) (b)

Figure 1.13: (a) Standard LFA requiring three different antibodies [16], (b) Schematic representation of the general Y-shaped structure of an antibody [66].

Bioreceptors Bioreceptors are the recognition elements of LFAs and are crucial for the binding of the NPs to the target analyte. They have two roles in LFAs: they functionalize the support (either the NPs or the membrane at the test and control line) and they catch the target analyte to be detected [60, 71].

Although many different bioreceptors exist (proteins, peptides, enzymes, nucleic acids, cells, phospholipids), antibodies (Ab) remain the most adapted for LFAs towards bacteria detection [66, 67, 71]. As it can be seen on Figure 1.13a, standard LFAs require three different types of antibodies: detection Ab (blue) to be conjugated with the NP and bind to the target analyte, capture Ab (green) initially striped at the TL and specific to the target analyte and control Ab (yellow) specific to the detection Ab (blue) striped at the CL [16].

More specifically, antibodies are a family of Y-shaped glycoproteins known as immunoglobulins (Ig), as represented in Figure 1.13b. Antibodies are made of two identical light protein chains (violet) and two identical heavy protein chains (red), held together by non-covalent interactions and disulfide bonds (yellow). Two identical antigen-binding sites are localized at the end of the arms of the Y (green) and are called F_{ab} fragments. On the other end, the C-terminus, also called F_c fragment, should be attached to the specific surface (either the NP surface or the membrane of the LFA). The specificity and affinity of an antibody towards the binding site of its antigen is a function of its amino acid sequence [66, 71, 72].

Bio-conjugation Although there are many different coupling strategies of antibodies to nanoparticles, the two main ones are either *via* adsorption or *via* carbodiimide coupling [73]. The choice depend on the nanoparticle to-be-conjugated, as described in Table 1.1.

On the one hand, bio-conjugation *via* adsorption is especially used for AuNPs and CNPs. This strategy uses non-covalent modes of binding based on a combination of ionic and hydrophobic interactions of the antibody and the NP surface. Although easy to apply, this conjugation method requires high concentration of antibodies, it orients the Ab randomly at the NP surface and they can easily desorb [74, 75].

On the other hand, bio-conjugation *via* carbodiimide coupling covalently links carboxylic acids to amines via formation of a "zero length" amide bond [73]. After adding carboxylic groups in the form of a polymer coating in the primary coating step (see subsection 2.2.1), a peptide bond is formed between the nanoparticle and the label by means of EDC/NHS chemistry. The main disadvantage of using EDC/NHS chemistry is that the number of binding sites can be negatively affected, as the carboxylic groups available from the labels can also react with the N-terminus primary amine of the antibodies, shown in green in Figure 1.13b [16, 73].

Since the bio-conjugation of nanoparticles is not part of the goal of this study, it will not be further discussed. Nevertheless, more information regarding the bio-conjugation of nanoparticles can be found in Appendix A for the reader's interest.

2.2.3 Surface passivation

Finally, a surface passivation step can be required to maintain the colloidal stability of the nanoparticles in solution. Most often, bovine serum albumin (BSA) is used to block non-desired adsorption on the nanoparticles. BSA also facilitates the release of the conjugated NPs from the conjugate pad [76, 77]. Other proteins, surfactants, polymers, and organic cations have also been used as stabilization agents. As a consequence, the hydrodynamic radius of the bio-conjugated nanoparticle increases [78].

2.2.4 Toxicity of nanoparticles

When dealing with nanoparticles, it is important to be aware of the negative impacts they might induce. Toxicity is one of them. Assessing the toxicity of nanoparticles means studying the adverse poisoning effects of these particles to humans, animals and the environment [79]. Toxicity of nanoparticles are often evaluated both *in vitro* and *in vivo*. *In vitro* tests is important in research as it is simple, inexpensive, and easy to control [80]. Nevertheless, data obtained *in vitro* may not always correspond to *in vivo* results because the system is much more complicated in the latter case. Moreover, NPs in cell culture conditions remain in close contact with the cells, thereby often leading to more pronounced cytotoxicity [81]. These results are thus not reliable enough to assess the toxicity of nanoparticles on real systems. Hence, comparisons between *in vitro* and *in vivo* results are very important [82].

When assessing the toxicity *in vitro*, cytotoxicity[1] is mainly studied. Given their reduced

---

[1] Toxicity in cells.

size, usually 1 to 200 nm, nanoparticles can be easily taken up by cells *via* endocytosis. Once inside the cell, the NPs can bind to the negatively charged DNA, causing damage to it. They can also alter the cell adhesion, which may further affect the cell morphology, proliferation, differentiation and survival. Nanoparticle cytotoxicity varies with different parameters such as size, shape, surface chemistry and biological coating [81, 83].

2.3 Gold nanoparticles

Gold nanoparticles (AuNPs) have already been mentioned several times in the previous sections. As a matter of fact, AuNPs are the most studied nanoparticles for lateral flow assay applications [7]. As mentioned in Table 1.1, their small size, intense red color, stability in time, low toxicity, high biocompatibility and easy synthesis make them great candidates for such tests. They are mostly used for colorimetric detection but their use for electrochemical and thermal contrast detection have also been reported many times in the literature [7, 16–19].

2.3.1 Underlying physics

The reason why AuNPs exhibit an intense red color can be explained with quantum physics through surface plasmon resonance (SPR). When the AuNPs are irradiated with light, as their size is much smaller than the incident wavelength, the conduction electrons of the nanoparticle surface oscillate in a collective fashion, which is known as SPR. This results in a strong absorption and scattering of light. The absorption peak and color of AuNPs depend heavily on the nanoparticle size, shape and medium (20 nm AuNPs strongly absorb 520 nm wavelength light and scatter red light) [16, 18]. SPR is also the reason why AuNPs are used in thermal contrast detection [63, 64]. Although LBs, CNPs and MNPs can also be used for colorimetric detection, it should be noted that their color does not stems from SPR [16, 19].

2.3.2 Synthesis

One main advantage of AuNPs is that they are easy to synthesize [84]. They have been intensively used since the early 50's thanks to the method brought by Turkevich *et al.* [85]. As shown in Figure 1.14a, the main idea is to reduce a gold precursor (tetrachloroauric acid, $HAuCl_4$) with sodium citrate (NaCt) in water under stirring. NaCt is used as a reducing and stabilizing agent. This method provides AuNPs with diameters from 7 to 30 nm [16, 86, 87]. Above 30 nm, the particles become less spherical, the size distribution becomes broader, and the results are less reproducible. Even bimodal particle size distributions can be observed [84]. Today, the protocol has been modified and improved, focusing on control of their size, shape, solubility, stability, and functionality [84, 86, 88].

In 1994, Brust and Schriffin reported another easy way to synthesize shown in Figure 1.14b. The idea here is to transfer $HAuCl_4$ from aqueous phase to toluene using tetraoctylammonium bromide (TOAB) as a surfactant and to further reduce it with sodium borohydride ($NaBH_4$) with the presence of dodecanethiols. The AuNPs are protected with thiols and have diameters in the range of $1.5-5$ nm [86, 87, 89].

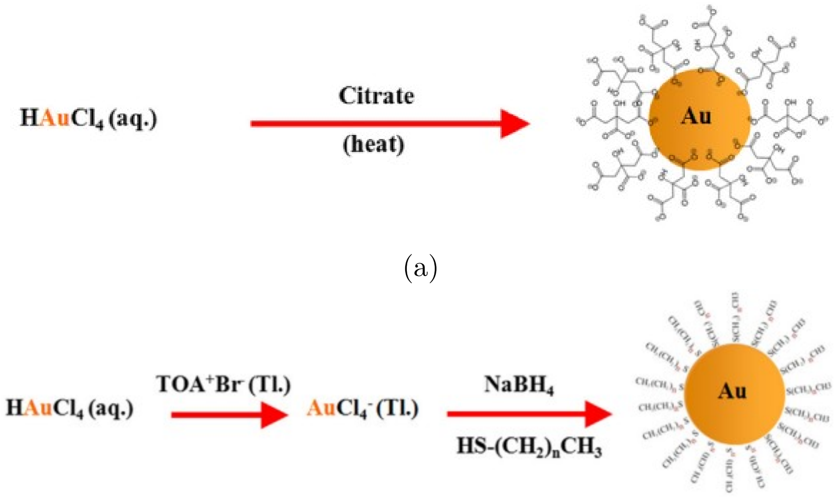

(a)

(b)

Figure 1.14: Illustration of the AuNP synthesis with (a) Turkevich method and (b) Brust-Schriffin method, taken from [87].

2.3.3 Size, morphology and size distribution control

By playing with particular parameters during the AuNP synthesis, it is possible to control the size, morphology and size distribution of AuNPs.

Dong *et al.* [84] have reviewed the effect of molar ratio of NaCt to $HAuCl_4$, batch size, initial $HAuCl_4$ and reaction temperature on the AuNPs. The most effective parameter to play with is the molar ratio (MR) of NaCt to $HAuCl_4$. By decreasing the molar ratio from 4 to 0.5, studies have shown that the size of the particles increased from 4 to 150 nm, as shown in Figure 1.15a [85, 90, 91].

Figure 1.15b shows that increasing the initial concentration of $HAuCl_4$ from 0.2 mM to 1 mM does not change the average particle size (peak at the wavelength) but increased the polydispersity as the peak breadth increased slightly.

Moreover, the influence of temperature depends on the chosen MR. As it can be seen in Figure 1.15c, it has a negligible effect for a MR of 7.6 but for 2.5, increasing the reaction temperature decreases the average particle size significantly from 43 to less than 20 nm.

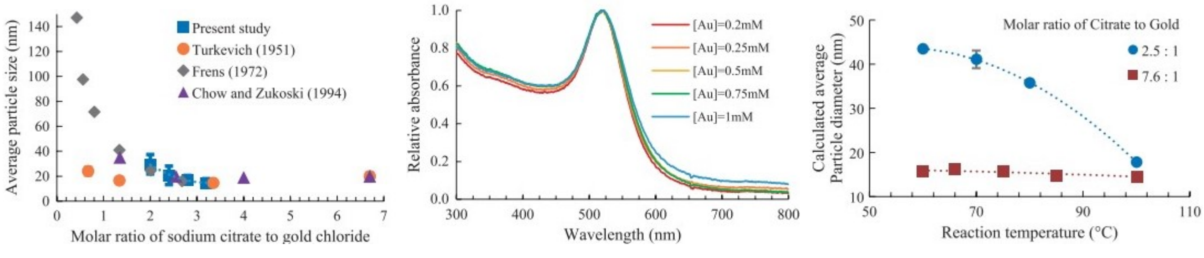

(a) (b) (c)

Figure 1.15: Tuning the properties of AuNPs by playing with parameters such as (a) molar ratio of NaCt to $HAuCl_4$, (b) initial concentration of $HAuCl_4$ and (c) reaction temperature [84].

2.3.4 Biofunctionalisation

As already discussed in section 2.2.2, AuNPs can be bio-conjugated with many different bioreceptors such as antibodies or nucleic acids. These can attach to the surface of the AuNPs either by adsorption or by carbodiimide coupling via EDC/NHS chemistry. Antibodies can adsorb via their C-terminus to AuNPs through hydrophobic and ionic interactions, or through chemisorption of thiol groups present in their chemical structure. However, this strategy contains several drawbacks due to the non-covalent bondings [74,75]. Thus, the carbodiimide coupling is the most frequently used strategy. It provides a more stable linkage between the AuNP and the antibody [92,93].

2.3.5 Toxicity

Gold nanoparticles can be thought to be non-toxic given that gold is a noble metal widely used in medical applications. However, given their reduced size, the properties of AuNPs change much compared to bulk gold. Once internalized in cells through endocytosis, AuNPs often induce reactive oxygen species (ROS) leading to DNA damage, DNA disrupting, cell death and cell cycle arrest [82]. As a matter of fact, Fratoddi *et al.* [83] and Jia *et al.* [82] reported that conflicting results are given in the literature regarding the cytotoxicity of gold nanoparticles, reporting both toxic and non-toxic effects.

In vitro *In vitro* studies have shown that particle size has an important effect on cytotoxicity, especially regarding the cellular uptake mechanism. Chitrani *et al.* [94] have shown that citrate-capped AuNPs with sizes ranging from 14 to 100 nm could all be internalized in cells, with uptake ranging between 500 and 6000 AuNPs per cell. In general, decreasing the size and increasing the concentration consequently induced more severe cytotoxicity as cellular uptake is favoured [82]. Moreover, the cytotoxicity of AuNPs is reduced when they are covered with antibodies as it alters the cellular uptake through endocytosis by changing the surface charge of the nanoparticles [83]. It is also possible that the surface groups on the AuNPs lead to toxicity. While amine-functionalized particles were only mildly toxic, particles functionalized with carboxylic acids were nontoxic under all the conditions examined [75]. AuNPs are often capped with sodium citrate, which does not influence the endocytosis mechanism compared to naked AuNPs [82].

In vivo *In vivo* toxicity of AuNPs is more complicated to assess. Less information is available in the literature. De Jong *et al.* have shown interesting results about the particle size dependency of *in vivo* toxicity. They injected gold nanoparticles with different sizes (10, 50, 100 and 250 nm) intravenously in rats. After 24h, it appeared that the 10 nm particles were present in every tissue (blood, liver, spleen, kidney, heart, lung and brain), while the larger particles were only detected in blood, liver and spleen. Hence, size distribution also influences organ distribution.
To illustrate the conflicting assessment of AuNP toxicity, Pompa *et al.* [95] have shown on the one hand that ingestion of 12 μg/g of 15 nm citrate-capped AuNPs induced a strong reduction of life-span and fertility and presence of DNA fragmentation on *Drosophila melanogaster*, a fly species.
On the other hand, Chen *et al.* [96] have studied the toxicity of citrate-coated AuNPs *in vivo* at doses of 8 mg/kg/week in mice. They showed that small (3–5 nm) and large AuNPs (30-100 nm) were not toxic, whereas medium-sized AuNPs (8-17 nm) provoked severe sickness, loss of weight, change in fur color, and shorter life spans. Moreover, it has also been shown that isotropic AuNPs larger than 5 nm are biologically inert [97].

2.3.6 Use in LFAs

Gold nanoparticles have been intensively used in LFAs for their numerous advantages reported in Table 1.1. They provide colorimetric, electrochemical and thermal contrast detection to LFAs. AuNPs have been used for detecting many different types of compounds in the literature, including bacteria, proteins and antibodies, nucleic acids, toxins, small molecules and heavy metals.
Protein detection is probably the most important use of LFA, specially in clinical diagnostics. Depending on the chosen antibody, different antigens from specific bacteria can be detected without cross-reactivity with other bacterial proteins [98, 99].
In addition, the detection of small molecules such as heavy metals have become very important in the last decades for environmental applications, especially for drinking water quality. Several studies reported AuNPs-base LFAs for detection of traces of heavy metals like Cd^{2+}, Pb^{2+}, Hg^{2+} or Cu^{2+} [100–103] and radioactive isotopes such as uranium [104]. Apart from water quality, AuNP-based LFAs have been used for many other medical applications such as detection of human infectious diseases like malaria, syphilis or tuberculosis [105, 106] or viruses like SARS-CoV-2 [26, 107].

2.3.7 Enhancement strategies

AuNPs also have some drawbacks for LFA applications, *i.e.* a poor sensitivity and limit of detection (cfr. Table 1.1). To remedy this, intensive research has been conducted to improve the signal from AuNPs. In addition to the enhancement strategies intrinsically related to the LFA assembling discussed in section 1.5, the discussion here is more focused on the AuNPs themselves.

Choi *et al.* [108] have taken profit from the arrangement of LFAs to enhance the colorimetric signal of the AuNPs with a very straightforward strategy. As shown in Figure 1.16, they used two conjugate pads loaded with AuNPs of 10 and 40 nm. The smaller NPs, conjugated with the detection antibody and BSA (cfr. section 2.2.2), flow faster through the membrane towards the TL and CL. Afterwards, the bigger AuNPs, conjugated with anti-BSA antibodies, bind to the smaller AuNPs, leading to an enhanced colorimetric signal. The detection sensitivity increased about a 100-fold compared to the conventional LFA and they could detect as low as 0.01 ng/mL of analyte in 10 min.

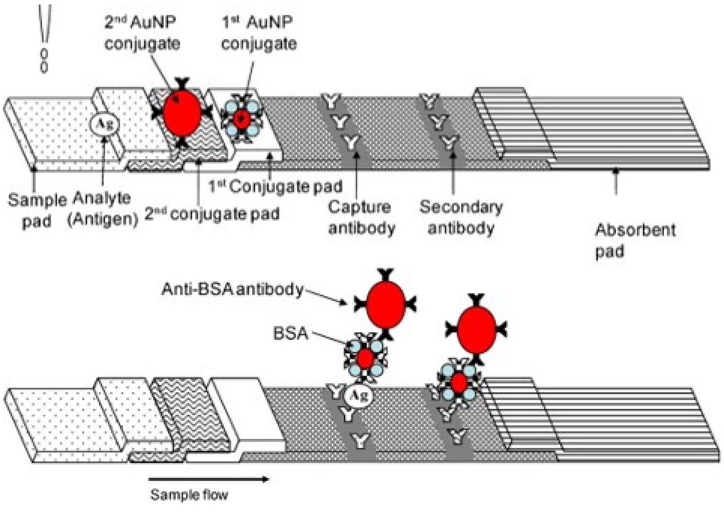

Figure 1.16: Signal enhancement of LFA by using two sizes of AuNPs [108].

Another efficient way to enhance the optical signal provided by AuNPs in LFAs is to conjugate them to enzyme-modified antibodies to produce enzymatic reactions at the test line. The colored products of these reactions enhanced the total color at the test line. In this way, Parolo *et al.* [109] increased the sensitivity by one order of magnitude compared to classical AuNP-based LFAs. The limit of detection was lowered to 5 ng/mL of human IgG by naked eye, which was not possible with non-modified AuNPs. Nevertheless, this strategy increases the development and testing times and the enzymatic reagents have low stability over time.

2.4 Magnetic nanoparticles

The use of magnetic nanoparticles (MNPs) and their advantages for LFA applications have been introduced in section 2.1.4 and summarized in Table 1.1. MNPs group a wide range of metallic oxide nanoparticles exhibiting different magnetic behaviors under an applied magnetic field. This is very promising to increase the sensitivity of LFAs. First, it enables the pre-concentration of the analyte in the water sample before dropping it onto the sample pad (cfr. section 2.4.8). Second, as biological entities and papers do not exhibit any magnetic behavior, it is possible to obtain extremely low LoDs. Third, all the MNPs at the TL and CL participate to the signal. In comparison, only the surface AuNPs provide the red colored signal. In addition, MNPs can also be used for colorimetric assays as they exhibit a orange-brown color [7, 16, 18, 19].

2.4.1 Underlying physics

The magnetic behavior of MNPs depend on the arrangement of the magnetic dipoles in the material. Magnetic dipoles group electrons circulating around atomic nuclei, electrons spinning on their axes and rotating charged atomic nuclei. If the sum of these three effects do not fully cancel, the atom is a permanent magnetic dipole. The magnetic dipole moment of an atom represents the dipole's ability to align with a given applied magnetic field [110–113].

Materials can exhibit five main magnetic behaviors, depending on the arrangement of the magnetic dipoles with and without applied magnetic fields H, as represented in Figure 1.17a. They are briefly described hereafter [114, 115].

- Diamagnetic materials, like gold or copper, do not contain magnetic dipoles in the absence of an applied field and have weak induced dipoles in the presence of a field, directed oppositely to the applied field.
- Paramagnetic materials like aluminum have non-zero randomly oriented dipoles that can be aligned with the applied field.
- Ferromagnetic materials always contain magnetic dipoles in the absence and presence of an applied field and exhibit long-range order. At the macroscale, such materials display a permanent magnetic moment.
- Ferrimagnetic materials always have opposed magnetic moments unequal in magnitude. They thus also exhibit a permanent magnetic moment.
- Antiferromagnetic materials also have opposed magnetic moments but they cancel each other in the absence of an applied magnetic field.

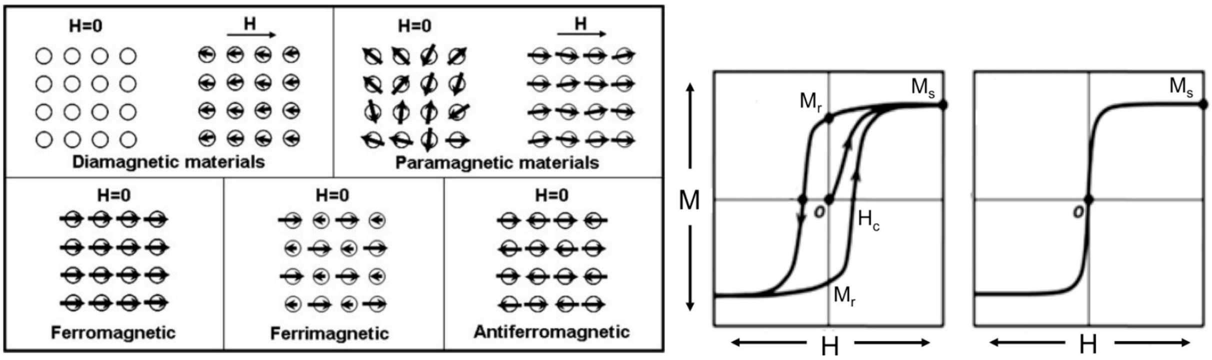

(a) (b)

Figure 1.17: (a) The five magnetic behaviors with and without an applied magnetic field H and (b) Two typical magnetization curves generated by an applied magnetic field H for ferromagnetic (left-hand side) and superparamagnetic (right-hand side) materials [116].

On a microscopic scale, the magnetization of ferromagnetic materials spontaneously divides into many small regions called magnetic domains when cooled below a temperature called the Curie temperature (e.g. 770°C for Fe). The magnetization in each domain is uniform but different domains point in different directions [111].

These phenomena lead to the magnetization curves shown on the left-hand side of Figure 1.17b. When a ferromagnetic material is subjected to a magnetic field H for the first time, by increasing H, more and more domains tend to align to the magnetic field, increasing the magnetisation inside the material by following the first-magnetisation curve up to saturation M_s.

When the applied magnetic field goes back to zero, some domains will go back to their initial direction and some will stay oriented with H. Hence, a remanent magnetisation M_r remains inside the material. The coercive field H_c is the field strength required to demagnetize the ferromagnetic material.

In the case of MNPs of 10-50 nm, their size is so small that they are made of only one single magnetic domain, which leads to a particular magnetisation curve shown on the right-hand side of Figure 1.17b. This phenomenon is called super-paramagnetism. As a matter of fact, they behave like a giant paramagnetic atom, with negligible remanent magnetization but a strong response to applied magnetic fields [117]. This extraordinary property prevents any attractive or repulsive forces between the MNPs (if $H = 0$) and have made them therefore very interesting for many applications like LFAs [18, 116, 117].

2.4.2 Different types of MNPs

In reality, there exist many different types magnetic nanoparticles of different compositions, phases and elements. The most notable ones are of course the iron oxides such as Fe_3O_4 or γ-Fe_2O_3 but also metallic oxides MFe_2O_4 (M = Co, Ni, Zn), pure metals such as Fe, Ni and Co, spinel-type ferromagnets such as $MgFe_2O_4$ and even alloys such as $CoPt_3$ and FePt [116, 117].

In this study, only iron oxide nanoparticles made of magnetite (Fe_3O_4) and maghemite (γ-Fe_2O_3) are considered. They have been widely used for magnetic LFAs because of their easily tunable size, shape and composition, good biocompatibility, low-cost production, good magnetic properties and because they possess numerous synthesis methods.

Nevertheless, these MNPs possess large surface-to-volume ratio and thus high surface energies, making them susceptible to aggregate significantly in order to minimize it. Moreover, they also tend to oxidize at the expense of colloidal stability and good magnetic properties. As it will be discussed later, this is why iron oxide MNPs need a primary coating (as introduced in section 2.2.1 [117,118]. In particular, magnetite NPs are not very stable under ambient conditions and are easily oxidized to maghemite. However, since maghemite is a ferrimagnet, this oxidation is not a major problem at this stage of the development of the biosensor [117].

2.4.3 Synthesis

There are many ways to synthesize iron-oxide MNPs. The most famous ones, namely direct co-precipitation, thermal decomposition and hydrothermal synthesis are reported in Table 1.2 with their size range, reaction temperature, advantages and drawbacks. This table also mentions how to control and tune several MNPs properties. Figure 1.2 shows a schematic representation of the three syntheses. Reddy *et al.* [81] have reported many other methods for MNP synthesis, such as micelle synthesis or pyrolysis techniques.

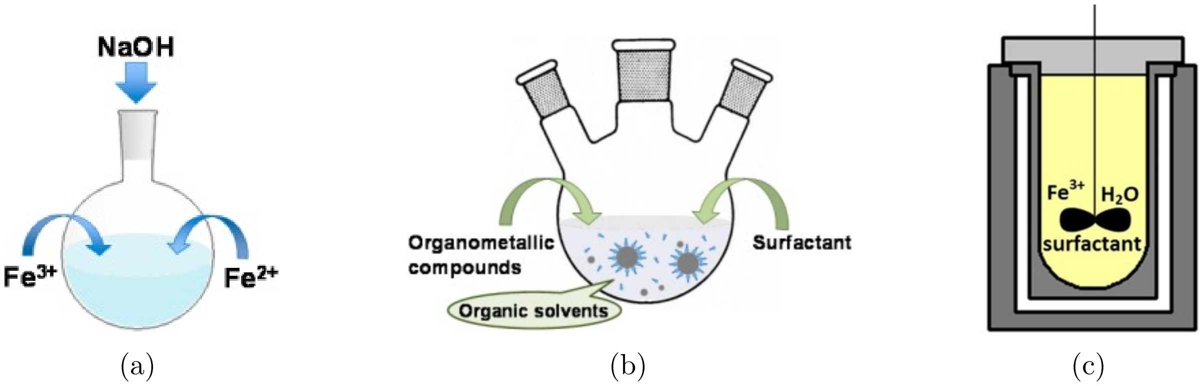

(a) (b) (c)

Figure 1.18: Schematic representation of the three main synthesis methods of MNPs: (a) Direct co-precipitation [116], (b) Thermal decomposition [116], (c) Hydrothermal synthesis [119].

Synthesis of iron oxide nanoparticles *via* direct co-precipitation is the simplest and most efficient method. It is based on chemical reactions carried out in an aqueous monophasic medium, allowing both the nucleation and growth of the MNPs. As shown in Figure 1.18a, the typical synthesis procedure consists of the addition of a base (e.g. NH_4OH or NaOH) to a solution of Fe(III) and Fe(II) salts. The chemical reaction is shown in Eq. 1.1 [81,118,120].

$$\mathrm{Fe^{2+}} + 2\,\mathrm{Fe^{3+}} + 8\,\mathrm{OH^-} \longrightarrow \mathrm{Fe_3O_4} + 4\,\mathrm{H_2O} \tag{1.1}$$

In the thermal decomposition method shown in Figure 1.18b, organometallic complexes and metal precursors such as iron cupferronate, iron acetylacetonate, and iron oleate are decomposed at elevated temperatures. This method provides the narrowest size distribution and the best colloidal stability to the MNPs [116, 117].

Finally, the hydrothermal synthesis method is used to synthesize MNPs in aqueous media and in reactors or autoclaves at high temperature and pressure. This environment results in rapid nucleation and fast growth of the newly formed particles, leading to the formation of small-sized NPs [116, 121]. For the three methods presented, the control of MNP properties such as size and shape are reported in Table 1.2 with the related parameters to vary.

Table 1.2: Three methods for synthesising MNPs, their size-range, reaction temperature, advantages, drawbacks, the properties that can be controlled and by varying which parameter, inspired from [81, 116, 117] (*) M = Fe, Co, Ni, Zn, (**) T° = Temperature.

Method	**Material**	**Size [nm]**	**Temp. [°C]**	**Advantages**	**Drawbacks**	**Control and tuning**	
						Property	**Variable**
Co-precipitation	Fe_3O_4 γ-Fe_2O_3	4-43	20-90	Easy synthesis Low reaction T° (**) Reproducible	Bad shape control Large size distribution	Size, Shape Magn. properties Composition	Fe^{2+}/Fe^{3+} ratio, pH, T° (**), Salts Media ionic strength
Thermal Decomposition	Fe, Co, Ni $MFe_2O_4^{(*)}$ FePt, FeCo	2-150	20-90	Good shape control Narrow distribution Hydrophobic coating	Complicated synthesis High temperatures Size& shape control	Size Shape	Reaction time and T° (**), Reagent ratio, Solvent, Surfactant
Hydrothermal	Fe_3O_4 $CoFe_2O_4$	9-12	100-220	Good shape control Narrow distribution, Easy synthesis	Autoclave needed Little explored for iron oxides	Size Surface funct.	Reaction T° (**), Solvent, Surfactant Ratio EG/DEG

2.4.4 Functionalisation

Iron oxide nanoparticles are extremely reactive in the presence of water or humid air. Their protection is thus crucial to ensure a good physical and chemical colloidal stability. This can be done with a primary coating, introduced in section 2.2.1. Surface coatings also increase the water-dispersibility of the MNPs, reduce their toxic effects and provide a suited functionalization surface for further bio-conjugation with antibodies or other entities. Different coating procedures have been introduced in section 2.2.1. The most used ones for MNPs include polymer coatings (*i.e.* with PVA or PEG), inorganic shells (*i.e.* silica, gold or graphite) and organic ligands. [81, 116, 117]
Among all these different coatings, silica (SiO_2) appears to be the best choice for LFA application. Indeed, silica coating does not affect the magnetic properties of the iron core (if not excessively thick), has a convenient and inexpensive procedure and provides functional groups for further conjugation with bioreceptors.

The Stöber method is a sol-gel process that has been used for many years for silica coating on iron oxide NPs. Briefly, a sol–gel process is a method for producing solid materials from small molecules. The process involves two main reactions: first the hydrolysis of the precursor in the acidic or basic mediums and then a polycondensation of the hydrolyzed products. In the end, a polymeric network is formed in which MNPs can be retained [122, 123].
Here, the Stöber method uses hydrolysis of tetraethoxysilane (TEOS) as a precursor under basic conditions (e.g., ammonium hydroxide solution) to condense and polymerize TEOS into a silica shell on the surface of the magnetic core. The chemical reaction can be ideally expressed as in Eq. 1.2 and 1.3 [124].

$$\mathrm{Si(OC_2H_5)_4 + 4\,H_2O \longrightarrow Si(OH)_4 + 4\,C_2H_5OH} \tag{1.2}$$

$$\mathrm{Si(OH)_4 \longrightarrow SiO_2 + H_2O} \tag{1.3}$$

The coating thickness can be tuned from 5 to 200 nm by increasing the reaction time and the concentrations of TEOS. This ability to control the thickness of the silica coating easily is very important as a too thick coating reduces the magnetic properties of the core significantly [117].

2.4.5 Bio-conjugation

After the synthesis and coating steps, the last one is the bio-conjugation of the silica-coated iron-oxide nanoparticles. As introduced in section 2.2.2 and Table 1.1, carbodiimide coupling via EDC/NHS chemistry is the most used strategy to graft antibodies on MNPs. Carboxilate-terminated ligands must first be attached to the silica layer in order to for an amide bond with the antibody by EDC/NHS chemistry.

2.4.6 MNP @AuNP

In addition to silica, polymers or other coatings mentioned previously, magnetic nanoparticles can also be coated with gold nanoparticles. Eyvazzadeh *et al.* [125] have not used such MNP @AuNP core-shell structures for LFA applications but as dual-function Magnetic Resonance Imaging (MRI) contrast agents and photosensitizer for cancer photothermal therapy. Hwang *et al.* [126] have used such nanostructures to detect Salmonella in milk by means of LFAs. Briefly, they first synthesized ∼160 nm iron-oxide NPs using a hydrothermal method and 14 nm AuNPs using a modified version of the Turkevich method. Afterwards, they added the MNPs and AuNPs to a solution containing (3-Aminopropyl)triethoxysilane

(APTES) to form amine groups at the surface of the MNPs and left the mixture under stirring for several hours. The final red spherical clusters had a diameter of ~180 nm and were successfully conjugated with polyclonal Salmonella antibodies. Their results are shown in Figure 1.19, including the absorption curve confirming that the AuNPs were successfully attached to the MNPs.

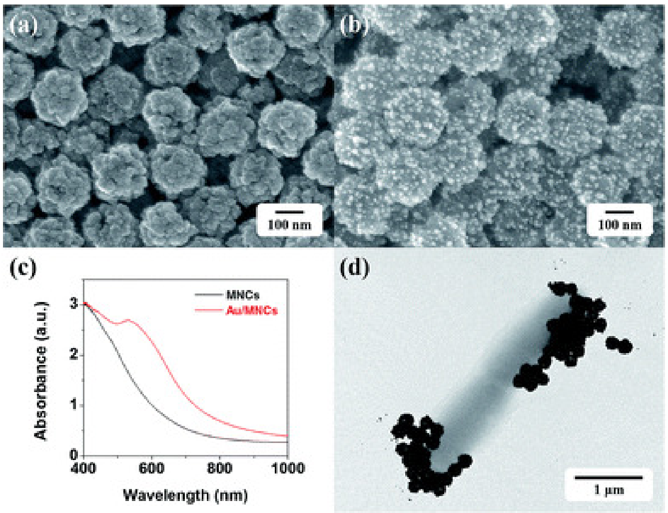

Figure 1.19: Results from Hwang *et al.* [126], where a-b show the MNPs before and after coating of AuNPs by Transmission Electron Microscopy (TEM), c shows the absorption curve of the NPs obtain by UV/Vis spectroscopy and d shows a TEM image of the MNP @AuNP grafted on a Salmonella bacteria

2.4.7 Toxicity

The toxicity of iron nanoparticles results from its ability to generate reactive oxygen species (ROS), like AuNPs (cfr. section 2.3.5). These ROS include hydroxyl radicals which are highly chemically reactive [80,127]. Iron-oxide NPs can however be rendered biocompatible when coated with materials such as silica, gold and PEG. In this way, the generation of ROS is hindered. The toxicity of the iron core depends on the size, chemical composition, surface charge, and particle-induced reactions [116].

In vitro researches have shown that MNP cytotoxicity was influenced by the particle size. For instance, at 80 μg/mL, 30 nm Fe_3O_4 particles caused higher oxidative DNA damage than 500 nm particles at the same concentration. As for AuNPs, cytotoxicity also depends on the NP concentration. During the same experiments, both 30 and 500 nm particles were not toxic anymore for concentrations of 40 μg/mL [81]. *In vitro* tests have also shown that the particle size may have different effects on cells. Karlsson *et al.* [128] showed that iron-oxide NPs of 30 nm size were much more toxic than 0.5 μm-sized nanoparticles. The smaller particles caused higher oxidative DNA damage and cell death.

Baber *et al.* [129] compared the toxicity of coated and uncoated iron-oxide nanoparticles with silica on cells *in vitro*. They observed that the silica coating provides prevents the mobilization of soluble iron from the particle to the cell, thereby reducing cytotoxicity or induction of inflammatory response to almost nothing.

2.4.8 Use of MNPs for immunomagnetic separation

As already mentioned, magnetic nanoparticles can be used in LFAs to pre-concentrate the analyte before applying it on the sample pad of the assay, as shown schematically in Figure 1.20. Instead of being pre-stored in the conjugation pad like traditional AuNP-based LFAs, the conjugated MNPs are mixed with the analyte and interact with the specific target to be detected. Under an applied magnetic field, the nanoparticles conjugated to the analyte are attracted towards the bottom of the recipient. Then, the excess sample without any target analyte is removed. This makes it possible to increase the concentration of the analyte in the sample by reducing the volume from several liters to few milliliters. Using this immunomagnetic separation strategy, Liu *et al.* [130] improved the sensitivity of their LFA 50-fold compared to traditional AuNP-based colorimetric tests.

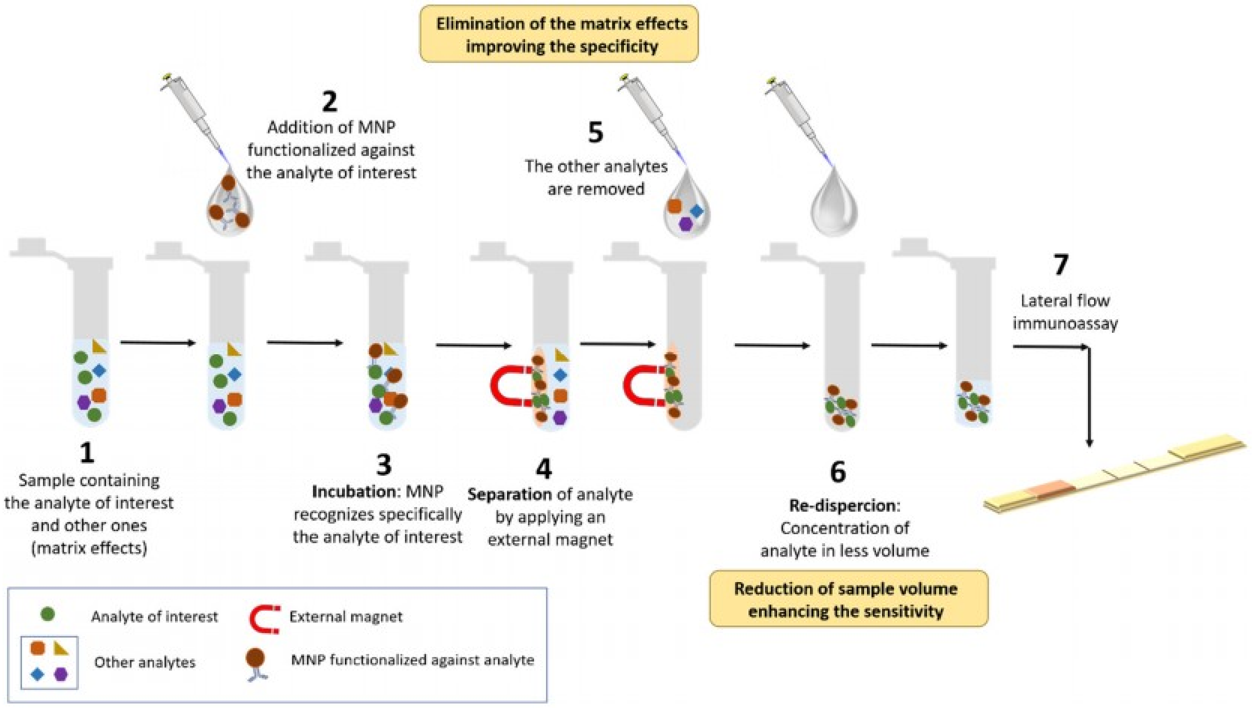

Figure 1.20: Step-by-step representation of immunomagnetic separation before application onto the sample pad of the LFA [61].

2.4.9 Use of MNPs for quantification

In addition to immunomagnetic separation and colorimetric detection, MNPs have also been used in LFAs for quantitative magnetic detection. The possibility to quantify the amount of analyte in the sample is very powerful, especially for water quality assessments. Indeed, as it was already mentioned, the level of contamination admitted varies according to the local legislations, the intended use of the water (drinking, swimming, ...) or the harmful character of the bacteria or toxic substance [14, 15].

Several methods to quantify magnetic nanoparticles at the detection zones in LFAs have been reported in the literature. They are based on different physicochemical transducing principles which can be divided into two groups: magnetoresistive and inductive readers. The most famous magnetic transducers are Giant Magnetoresistance (GMR), Tunnel Magnetoresistance (TMR) and Magnetic Particle Quantification (MPQ). They are schematically represented in Figure 1.21. Some of them are commercially available and others have been developed by academic research groups with the aim of improving the analytical characteristics or portability requirements [61, 117].

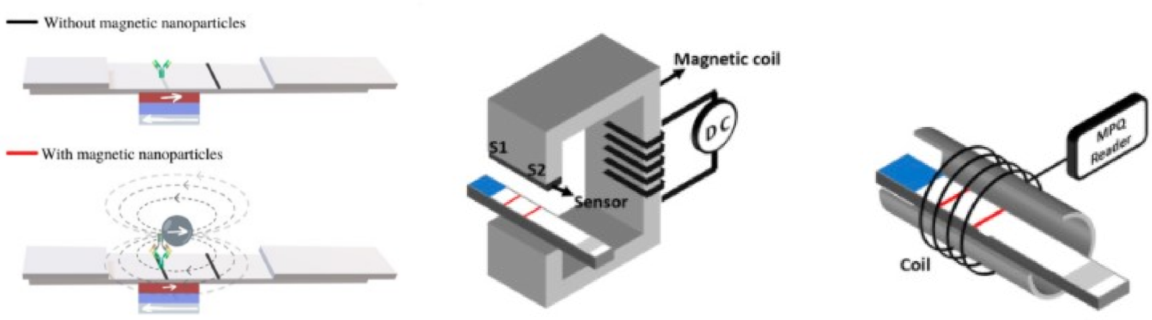

(a) (b) (c)

Figure 1.21: Magnetic detection with LFAs via (a) GMR, (b) TMR and (c) MPQ [61, 73].

Taton *et al.* [131] used a GMR to quantify the amount of proteins (rabbit IgG and interferon-γ) present in the sample with a GMR as external reader, similar to the one shown in Figure 1.22a. They achieved a low LoD of 12 pg/mL protein. The main challenge is now to miniaturize the GMR in order to use it as a PoC device.

Orlov *et al.* [132] used an MPQ reader to detect prostate-specific antigen (PSA) with 200 nm MNPs. They reached an impressive LoD of 60 zmol (zeptomole, 10^{-21}). As shown schematically in Figure 1.22b, the LFA strips pass through the measuring coil of the portable MPQ reader to quantify the number of MNPs bound at the test and control lines. The measured signals are interpolated in order to correlate the signal intensity with the number of MNPs.

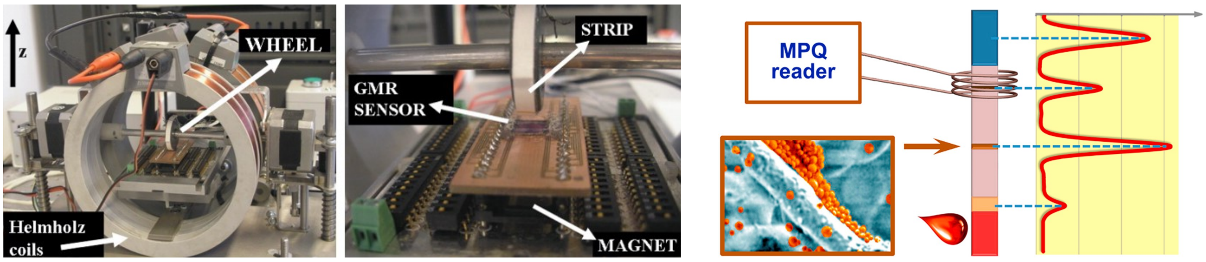

(a) (b)

Figure 1.22: (a) Picture of a GMR used for magnetic quantification on a LFA strip [133] (b) Representation of a quantification strategy using an MPQ to quantify the number of MNPs bound at the test and control lines [132].

2.5 Multiplexing

The different detection methods discussed previously always led to the detection of one single analyte in the sample. However, the easy working principle of LFAs makes it possible to detect several analyte at the same time. Many research groups developed multiplexed LFAs in recent years. Some interesting cases are shown below.

The easiest way is to add several test lines on the membrane with different capture antibodies specific to different analytes. Yonetika *et al.* [134] have used this strategy to detect three serogroups of Shiga toxin-producing Escherichia coli (STEC) simultaneously, with polyclonal antibodies anti-O157, anti-O26, and anti-O111. The result is shown in Figure 1.23a. They used different conjugated AuNPs and succeeded in conducting single detection (strips 1–3 from top to bottom), double detection (strips 4–6), and triple detection (strip 7).

Another way to simultaneously detect different analyte is to extent the shape of the LFA to 2 dimensions, as shown in Figures 1.23b. Here, instead of assigning one test line to one analyte, each branch is used to detect one specific analyte. Although the number of conjugate pads, membranes and absorbent pads increase with the number of branches, only one large sample pad is necessary. Nevertheless, the manufacturing becomes more complicated and the test less user-friendly [135–138].

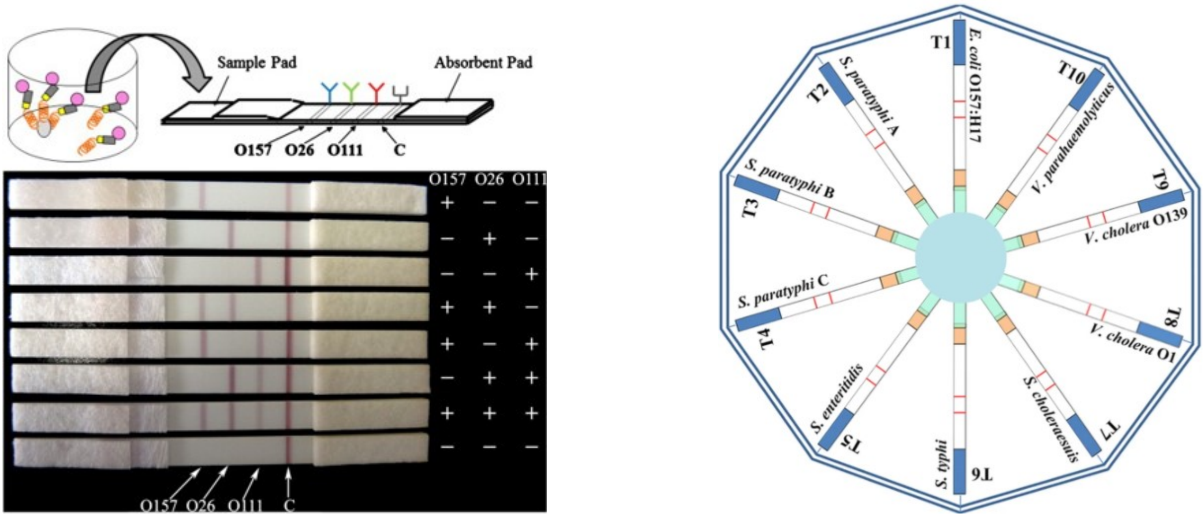

(a) (b)

Figure 1.23: Different multiplexing strategies: (a) using several test lines with different immobilized Ab [134], (b) using a 2D geometry with a single sample pad and different branches for different analytes [137].

Chapter 2

Objectives and Strategy

This master thesis fits within the development of low-impact paper-based biosensors based on LFAs for bacteria detection in remote area water samples.
The goal of this master thesis is to give a preliminary study regarding the use of nanoparticles in lateral flow assays, the different ways they can be obtained and the main parameters influencing their properties in order to open new electrical and magnetic detection opportunities.

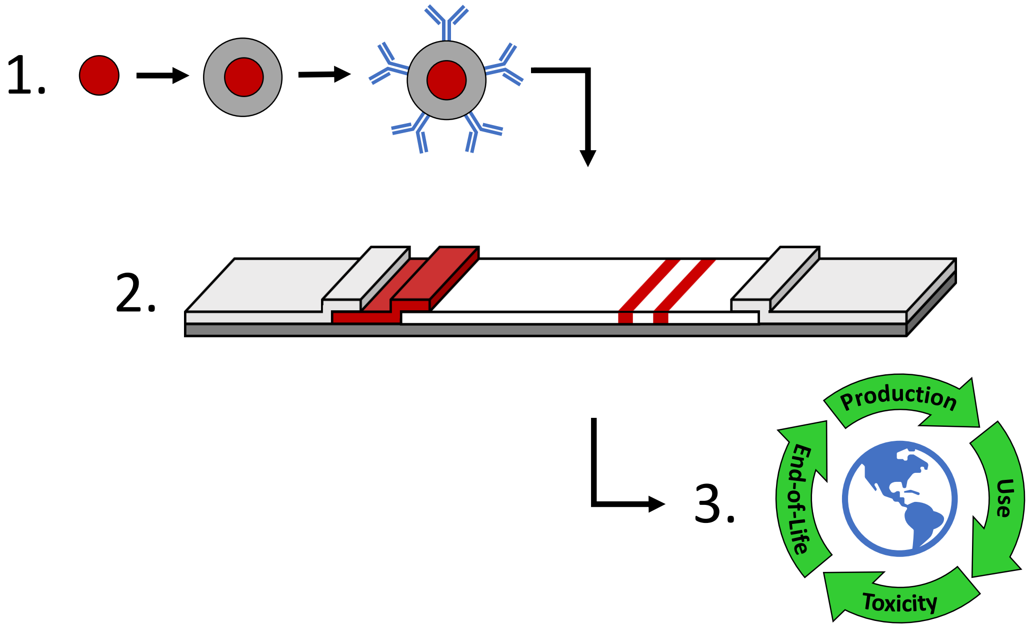

Figure 2.1: General overview of the structure of this master thesis.

The framework of this thesis is divided in three main parts schematically represented in Figure 2.1. More specifically, the objectives of each step of the thesis are:

1. To synthesize, coat and characterize gold and iron-oxide magnetic nanoparticles and compare them with commercial units. The scope of this thesis stops when the nanoparticles are ready for conjugation with the bioreceptors for subsequent specific binding to the analyte. Special attention is paid to their:
    - Size, such that, when bound to the target analyte, they do not increase their size too much and thereby clog the pores of the paper.

   - Dispersion, such that they are individually conjugated to bioreceptors and thus individually bind to the target analyte.
   - Shape, to ensure a consistent and reproducible flow through the LFA to improve the test sensitivity.
   - Intrinsic colorimetric, electrical or magnetic properties to explore their potential for signal transduction purposes.

2. To analyze the behavior of nanoparticles in paper microstructures to anticipate any clogging of the pores and non-specific binding with the fibers. This is done by:
   - Characterizing the microstructure of the papers.
   - Analyzing the water front evolution in LFAs, with and without NPs.

3. To assess the environmental impacts of the papers, nanoparticles and plastics used for 1 million tests in order to anticipate potential adverse consequences of LFAs on the environment. This is made of three main steps:
   - An assessment the most impacting components based on their energy demand, carbon footprint and water usage.
   - A study of the toxic effects of nanoparticles on human health and on ecosystems.
   - A proposition of adequate end-of-life strategies for each component.

Chapter 3

Materials and methods

This chapter summarizes the different materials and methods used in this study. First, the protocols followed for the synthesis and functionalization of the gold and magnetic nanoparticles are described. Second, the materials and assembling steps applied for the LFA manufacture are outlined. Finally, the working principle behind the characterization techniques utilized in this study are introduced. All the chemicals used for the NP synthesis are gathered in Table 3.1.

1 Nanoparticle synthesis

1.1 AuNP synthesis

Gold nanoparticles were synthesized by adapting a procedure from Hwang *et al.* [126] based on the Turkevich method explained in section 2.3. In an erlenmeyer, 10 mg of gold(III) chloride hydrate ($HAuCl_4$) was first suspended in 80 mL of deionized (DI) water under magnetic stirring at room temperature. The liquid had a light yellow color at first and became transparent after a few tens of seconds. Then, sodium citrate (NaCt, $HOC(COONa)(CH_2COONa)_2 \cdot 2H_2O$) was added to the solution, with a quantity defined by the investigated molar ratio (MR). The latter is defined in Equation 3.1. NaCt acts as a stabiliser for the future AuNPs and provides functional groups for conjugation with proteins.

$$MR = \frac{mol.\ wt.\ NaCt}{mol.\ wt.\ HAuCl_4} \tag{3.1}$$

Considering always 10 mg of $HAuCl_4$, molar ratios of 1.7, 2.3, 3.0 and 3.7 were investigated, inspired from Dong *et al.* [84]. The color of the solution does not change after adding the NaCt. The latter can also be dissolved in DI water before the $HAuCl_4$, the order does not affect the AuNP formation. Finally, 7.5 mg of sodium borohydride ($NaBH_4$) was added to the solution, which became instantaneously red. Depending on the molar ratio, the solution can exhibit a more or less intense red color. The higher the molar ratio, the lighter the red color of the solution was. $NaBH_4$ acts as a reducer for the gold precursor.

Commercial AuNPs provided by Unisensor® were used also in this study. They were delivered with an optical density (OD) of 8, stabilized with NaCt and dispersed in DI water.

Table 3.1: Reactants and solvents used in this study for the synthesis of the different NPs, their purity/grade, abbreviation and supplier, in alphabetical order.

Name, Purity/Grade	Abbrev.	Supplier
(3-Aminopropyl)triethoxysilane, 99%	APTES	Sigma-Aldrich
Ammonium hydroxide, Extrapure, 25% solution in water	AH	Acros Organics
Diethylene glycol, ReagentPlus®, 99%	DEG	Sigma-Aldrich
Dioctyl ether, 99%		Sigma-Aldrich
Ethanol, 99% EURO DENATURED TechniSolv®	EtOH	VWR Chemicals
Ethylene glycol, Spectrophotometric grade, 99+%	EG	Alfa Aesar
Gold(III) chloride hydrate, 99.995%, trace metals basis	$HAuCl_4$	Sigma-Aldrich
Gold nanoparticles citrate capped in water		Unisensor
Hexadecyltrimethylammonium bromide, $\geq$98%	CTAB	Sigma-Aldrich
Iron(III) acetylacetonate, 97%	$Fe(acac)_3$	Sigma-Aldrich
Iron(III) chloride·$6H_2O$, 97%	$FeCl_3 \cdot 6H_2O$	Sigma-Aldrich
Iron(II,III) oxide nanopowder, 50-100 nm particle size (SEM), 97% trace metals basis		Sigma-Aldrich
Iron(II) sulfate·$7H_2O$, 99% for analysis	$FeSO_4 \cdot 7H_2O$	Acros organics
n-Hexane, 97% HiPer Solv CHROMANORM for HPLC		VWR Chemicals
Nitric acid, 68%	HNO_3	VWR Chemicals
Oleylamine, Approximate C18-content 80-90%		Acros organics
Polyvinylpyrrolidone, Average mol. wt. 40000	PVP	Sigma-Aldrich
Sodium acetate, Anhydrous, ReagentPlus®, $\geq$99.0%	NaOAc	Sigma-Aldrich
Sodium acrylate, 97%	SA	Sigma-Aldrich
Sodium borohydride powder, $\geq$98%	$NaBH_4$	Sigma-Aldrich
Sodium citrate dihydrate, $\geq$99%	NaCt	Sigma-Aldrich
Sodium hydroxide, 99% AnalaR NORMAPUR® pellets ACS/Reag Ph. Eur.	NaOH	VWR Chemicals
Tetraethyl orthosilicate, for synthesis	TEOS	Sigma-Aldrich

1.2 MNP synthesis

Iron-oxide magnetic nanoparticles were synthesized by means of three different methods shown in Figure 1.18, namely by co-precipitation (MNP-CP), thermal decomposition (MNP-TD) and hydrothermal (MNP-H) synthesis.

1.2.1 Direct co-precipitation method

Iron-oxide magnetic nanoparticles were synthesized by adapting a procedure from Mederos-Henry *et al.* [139]. In a 500 mL round-bottom and long-necked flask, 15 mmol of iron(II) sulfate heptahydrate ($FeSO_4{\cdot}7H_2O$) and 7.5 mmol of iron(III) chloride hexahydrate ($FeCl_3{\cdot}6H_2O$) were dissolved in 250 mL of ultrapure water. The orange solution was heated to 60 °C using a liquid oil bath and stirred using a mechanical rotating helix (RZR 2051 electronic, Heidoplh). Then, 15 mL of ammonium hydroxide (AH, NH_4OH) was added. A black precipitate was formed and the solution was stirred for 30 minutes. Then, after stopping the stirring, the solution was cooled to room temperature. The product was recovered by magnetic decantation and washed three times with a 50/50 ethanol (EtOH, C_2H_6O)/DI water solvent in the centrifuge, each time 10 minutes at 6000 rpm. The magnetic product was dried overnight at 120 °C and stored in a desiccator.

1.2.2 Thermal decomposition method

Iron-oxide magnetic nanoparticles were synthesized by adapting a procedure from Xu *et al.* [140]. Dioctyl ether ($[CH_3(CH_2)_7]_2O$) was used here instead of benzylether as it is cheaper while keeping the same properties for this case. In a 100 mL round-bottom flask, 3 mmol of iron(III) acetylacetonate ($Fe(acac)_3$) was dissolved in 15 mL of oleylamine ($C_{18}H_{35}NH_2$) and 15 mL of dioctyl ether. A condenser was connected to the flask and the solution was heated to 295 °C (0.1 °C/s) using a liquid oil bath. Once the temperature reached, the reaction mixture was refluxed for 1 hour under vigorous agitation. As ebullition of the mixture appeared, the temperature was lowered to 270 °C after 30 minutes to avoid any risk of explosion. Afterwards, a black precipitate was formed and the solution was cooled to room temperature. The magnetic response of the product was verified by approaching a magnet close to the solution. Then, the solution was washed twice at 6000 rpm during 10 min each time with 50 mL of EtOH. Finally, the magnetic product was dispersed in n-hexane (C_6H_{14}) and stored under ambient conditions.

1.2.3 Hydrothermal method

Iron-oxide magnetic nanoparticles were synthesized by adapting a procedure from Xuan *et al.* [141]. A bisolvent made of ethylene glycol (EG, $(CH_2OH)_2$) and diethylene glycol (DEG, $(HOCH_2CH_2)_2O$) was used here to tune the particle size. Increasing the volume ratio of DEG from 0% to 100% reduces the particle size from 170 to 6 nm [141]. In 20 mL of a 50/50 EG/DEG mixture, 0.54 g of iron(III) chloride hexahydrate ($FeCl_3{\cdot}6H_2O$), 1.5 g of sodium acrylate and 1.5 g of sodium acetate (SA, CH_3COONa) were dissolved and left under magnetic stirring for 3 min. The obtained yellow solution was transferred afterwards to a Teflon-lined stainless-steel autoclave and sealed to heat at 200 °C for 14 hours. Then, after 1h30 of cooling to room temperature, the magnetic response of the product was verified with a magnet. Afterwards, the product was washed twice with EtOH and subsequently twice with DI water (10 min at 6000 rpm each time). The final product was dried overnight at room temperature and stored in a desiccator.

1.3 Silica coating of MNPs

Iron-oxide magnetic nanoparticles are coated with a silica (SiO_2) layer by using the Stöber method. As it was explained in section 2.2, tetraethoxysilane (TEOS, $Si(OC_2H_5)_4$) is hydrolyzed with ammonium hydroxide (AH, NH_4OH) to condense and polymerize it into a silica shell on the surface of the nanoparticle. Different variations of the Stöber method are used depending on the magnetic nanoparticle to be coated.

1.3.1 Silica coating of MNP-CPs

The iron-oxide magnetic nanoparticles obtained by direct co-precipitation (MNP-CP) were coated with silica by adapting a procedure from Gao *et al.* [142]. The MNP powder stored in the desiccator were first ground in a mortar in order to obtain a very fine powder. Then, 80 mg of the powder was suspended in 45 mL of EtOH. The brown liquid was sonicated for 30 min (VWR Ultrasound cleaner, power level 9) and placed afterwards under magnetic stirring at room temperature. Then, AH and subsequently TEOS were added to the solution, both with different volumes given in Table 3.2. The color remained homogeneously brown after addition of the silica precursor. The mixture was stirred for 5 hours[1]. Finally, the solution was washed twice with EtOH at 6000 rpm for 10 minutes, dried at 120 °C for 6 hours and stored in a desiccator.

Table 3.2: The different quantities of ammonium hydroxide and TEOS used for the silica coating of the MNP-CPs.

Absolute Ratio	**1/4**	**1/4**	**1/4**	**1/3**	**1/3**	**1/2**	**1/2**	**2/3**	**2/3**
AH [mL]	1	0.5	0.25	0.66	0.5	1	0.5	1.33	1
TEOS [mL]	4	2	1	2	1.5	2	1	2	1.5

1.3.2 Silica coating of MNP-TDs

The iron-oxide magnetic nanoparticles obtained by thermal decomposition (MNP-TD) were coated with silica by adapting a procedure from Gao *et al.* [142]. The MNP-TDs were very stable in hexane and thus very difficult to separate from the solvent by centrifugation. Moreover, the Stöber method does not work in hexane and requires EtOH as solvent. Hence, 20 mL of EtOH were added to 6 mL of the MNP-TDs dispersed in n-hexane in order to de-stabilize them. After centrifugation for 10 minutes at 6000 rpm, the precipitate was separated from the n-hexane and re-dispersed in 40 mL of EtOH. After sonication for 5 minutes (VWR Ultrasound cleaner, power level 9), the mixture was placed under magnetic stirring. Then, 1 mL of AH and subsequently 3 mL of TEOS were added to the solution. After 5 hours of magnetic stirring, the product was washed three times with EtOH (10 min at 6000 rpm each time) and dried overnight at 120 °C.

1.3.3 Silica coating of commercial MNPs

The iron(II,III) oxide nanoparticles from Sigma-Aldrich (called commercial MNPs in the following) were coated with silica by adapting a procedure from Gao *et al.* [142]. In 40 mL of EtOH, 80 mg of the powder were mixed and sonicated for 60 min (VWR Ultrasound cleaner, power level 9). Then, under magnetic stirring, 0.5 mL of AH and subsequently 1 mL of TEOS was added to the solution. The black mixture was stirred for 5h50 and

---

[1] Except for the AH/TEOS ratio of 1/4 mL where the mixture was stirred overnight.

then washed three times with EtOH (10 min at 6000 rpm each time). After stopping the magnetic stirring, the product was black and homogeneous and precipitated in several minutes.

1.4 Mesoporous silica coating of MNPs

The MNP-CPs, MNP-TDs and commercial MNPs were coated with mesoporous silica by adapting a procedure from Haynes *et al.* [69]. The procedure was identical for the three different types of MNP mentioned earlier.[1] First, 250 mg of the respective MNP powder was mixed with a 35 mL solution made of 10 mL of sodium hydroxide (NaOH) 0.1 M and 25 mL of DI water. The solution was heated to 60 °C using a liquid oil bath. Then, 571 mg of hexadecyltrimethylammonium bromide (CTAB) was added and the mixture was stirred for 10 minutes. This is what induces the mesoporous structure of the silica. Afterwards, 0.7 mL of TEOS was added dropwise in 30 minutes with a single syringe infusion pump (KDS-100-CE, kd Scientific®). The syringe pump was configured with a rate of 1.4 mL/h and a syringe diameter of 5 mm. After 3h30 of magnetic stirring, the mixture was then transferred to a sealed teflon flask and heated in static mode at 100 °C for 72h. Finally, the product was centrifuged (10 min at 6000 rpm), washed once with EtOH, dried overnight and stored in a desiccator.

1.5 AuNP coating of commercial MNPs

The commercial MNPs from Sigma-Aldrich were coated with gold nanoparticles by adapting a procedure from Hwang *et al.* [126]. The first step was to coat the MNPs with APTES ((3-Aminopropyl)triethoxysilane), which will graft the AuNPs to the magnetic cores. To this end, 100 mg of the commercial MNPs were dispersed in 40 mL of EtOH and sonicated for 30 min (VWR Ultrasound cleaner, power level 9). Then, after adding 1 mL of APTES, the solution was stirred for 24h.

Two different solutions of AuNPs were grafted on the commercial MNPs. In each case, 10 mL of the APTES coated MNPs were sonicated for 5 minutes (VWR Ultrasound cleaner, power level 9) and placed under magnetic stirring. On the one hand, 1.5 mL of commercial AuNPs from Unisensor® were added to the solution. On the other hand, 30 mL of the AuNPs obtained with a molar ratio (MR) of 2.0 were added to the solution. In both cases, the mixture was stirred for 6 hours at room temperature.

In order to increase the concentration of AuNPs at the surface of the MNPs, the previous procedure was repeated over three cycles. After the APTES coating, the mixture was washed three times with EtOH (10 min at 6000 rpm each time). Then, 40 mL of the AuNP solution obtained with an MR of 3.2 was added to the centrifuged MNP@AuNP. The mixture was softly sonicated for 20 seconds (VWR Ultrasound cleaner, power level 3) in order to detach what sticks to the sides of the recipient. Then, the mixture was again left under magnetic stirring for 24h. This procedure was repeated three times. In the end, the final product was dried at 100 °C for the weekend.

---

[1] Except for the MNP-TDs, where 145 mg were used instead of 250. The proportions of the different chemicals were consequently adapted, *i.e.* 145 mg of MNP-TD, 331.18 mg of CTAB, 5.8 mL of NaOH 0.1 M, 14.5 mL of DI water and 0.406 mL of TEOS.

1.6 MNP stabilisation

Different procedures have been implemented in order to increase the dispersion of the magnetic nanoparticles.

1.6.1 Change of solvent

The MNP-TD coated with SiO_2 were dispersed in two different solvents, namely DI water and EtOH. The two mixtures were sonicated for 30 min (VWR Ultrasound cleaner, power level 9) and subsequently stored under ambient conditions.

1.6.2 Change of pH

The commercial MNPs were dispersed in three aqueous solutions with different pH. In each case, 3 mg of the commercial powders were first dispersed in 3 mL of DI water. In the first case, 0.1 mL of sodium hydroxide (NaOH) 1M was added. In the second case, 0.1 mL of nitric acid (HNO_3) 1M was added. In the third case, the sample was kept as such. The three mixtures were then sonicated for 5 minutes (VWR Ultrasound cleaner, power level 9).

1.6.3 PVP stabilisation

The MNP-CPs were mixed with polyvinylpyrrolidone (PVP) by adapting a procedure from Cha *et al.* [143]. In 3 mL of EtOH, 3.7 mg of the MNP-CP powder were suspended with 30 mg of PVP. The mixture was then sonicated for 10 minutes (VWR Ultrasound cleaner, power level 9).

1.6.4 CTAB stabilisation

The MNP-CPs were mixed with Hexadecyltrimethylammonium bromide (CTAB) by adapting a procedure from Cha *et al.* [143]. In 3 mL of EtOH, 3.9 mg of the MNP-CP powder were mixed with 30 mg of CTAB. The mixture was then sonicated for 10 minutes (VWR Ultrasound cleaner, power level 9).

2 Microfluidic tests with LFAs

Lateral flow assays were assembled manually by adapting the procedure from Parolo *et al.* [17]. The materials used are gathered in Table 3.3 with their main properties. All the papers were provided as sheets by the suppliers. The nitrocellulose (NC) sheets from Sartorius were delivered onto a 100 μm polyester backing. The polyester KN-2211™ adhesive cards from Kenosha® were used to assemble the different pads together.

Table 3.3: Materials used for assembling the LFAs, their suppliers and main properties.

Name, Supplier	Material	Pad	Caliper [mm]	Capillary flow time [sec/4cm]	Basis weight [g/m^2]
Surewick® C083, Merck-Millipore	Cellulose	SP, AP	0.83	?	291
ReliaFlow™ 237, Ahlstrom-Munksjö	High purity cotton fibers	SP, AP	0.42	86	183
ReliaFlow™ 601, Ahlstrom-Munksjö	High purity cotton fibers	SP	0.19	240	88
ReliaFlow™ 8950, Ahlstrom-Munksjö	Chopped glass (polyester)	CP	0.25	24	50
Unisart® CN95, Sartorius	Backed NC	M	0.25	95	52.5
Unisart® CN180, Sartorius	Backed NC	M	0.24	155	?
ReliaFlow™ 270, Ahlstrom-Munksjö	High purity cotton fibers	AP	1.82	50	39

2.1 Assembly of LFAs

The different steps for the assembling of the LFA are inspired from Figure 1.4, taken from Parolo *et al.* [17]. Figure 3.1 shows the geometry of the LFA strips manufactured in this study. The adhesive cards (AC) came with release liners (RL) that helped positioning the different pads always at the same distance with the same overlap. The geometry of the test was thus partially imposed by these release liners.

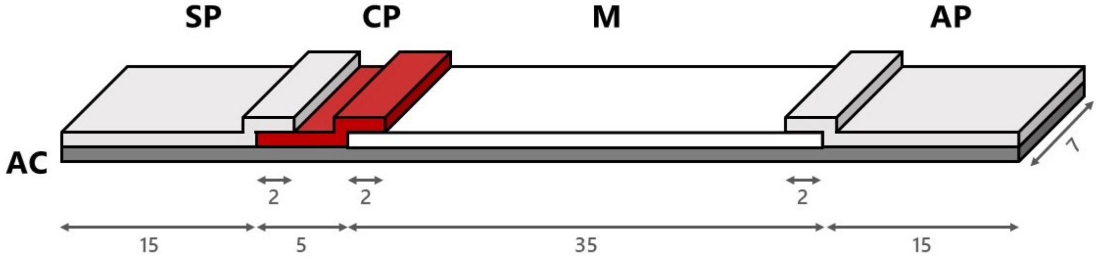

Figure 3.1: Schematic representation of the LFA strips manufactured manually (lengths in mm).

As shown in Figure 3.1, tests of 7 mm wide and 70 mm long were manufactured per 6, for reproducibility issues. The sample pad (SP), conjugate pad (CP), membrane (M) and absorbent pad (AP) were respectively 15, 5, 35 and 15 mm long. Overlaps of 2 mm between the different pads were chosen. The different steps for the assembling of 6 LFA strips are enumerated below. Standard scissors and a metal ruler were used for the cutting and measuring of the pads, respectively. These steps are to be followed for each investigated assembly.

1. Carefully cut out the four pads from the sheets with their respective length and a width of 42 mm.
2. Remove the central release liner and mount the backed side of the NC piece on the adhesive card. Be careful not to damage the NC surface.
3. Remove the release liner associated to the CP and mount the glass fiber piece on the adhesive card with an overlap of 2 mm on the membrane.
4. Remove the release liner associated to the SP and mount the cellulose piece on the adhesive card with an overlap of 2 mm on the conjugate pad.
5. Remove the release liner associated to the AP and mount the related cellulose piece on the adhesive card with an overlap of 2 mm on the membrane.
6. Carefully cut out the 6 strips of 7 mm width. Caution must be taken to not crush the different papers in order to keep their initial porosity.
7. Store the strips in a plastic pocket under ambient conditions.

2.2 Water front evolution in different assemblies

Different parameters were varied in order to compare the microfluidic performance of different LFAs. Here, the change of porosity and pore size was studied by changing the papers of the different pads.
To analyze the evolution of the water front in the LFA over time, blue food colouring was diluted 10 times in tap water was. Other colours are possible, as long as the contrast with the paper is sufficiently strong.

In particular, four different assemblies were manufactured following the steps presented before. The papers they were made of are gathered in Table 3.4. The test number 1 is taken as the reference test. From tests number 2 to 4, only one pad was changed compared to the reference test: the sample pad, the membrane and finally the absorbent pad, respectively. The capillary flow time of the changed pad was decreased in tests 2 and 3 while increased in test 4. Given its reduced length, the conjugate pad was always made of the same material, *i.e.* ReliaFlow$^{\text{TM}}$ 8950.
The procedure followed to measure the evolution of the front through the strips is described step-by-step in the following and was inspired from [144].

1. Prepare the 1/10 dilution of blue food color/tap water.
2. Stick the 6 strips on a sheet of paper with double-sided adhesive paper, with several centimeters between each test. This facilitates the handling and storage of the tests afterwards.

Table 3.4: The four investigated LFA assemblies and the different papers they are made of.

Test number	1	2	3	4
Sample Pad (ReliaFlow^{TM})	237 *86 sec/4cm*	**601** *240 sec/4cm*	237 *86 sec/4cm*	237 *86 sec/4cm*
Membrane (Unisart®)	CN95 *95 sec/4cm*	CN95 *95 sec/4cm*	**CN180** *155 sec/4cm*	CN95 *95 sec/4cm*
Absorbent Pad (ReliaFlow^{TM})	237 *86 sec/4cm*	237 *86 sec/4cm*	237 *86 sec/4cm*	**270** *50 sec/4cm*

3. Drop-cast 100 μL of water with a pipette onto the sample pad[1].
4. Start the timer when the water front reaches the membrane at 20 mm[2].
5. On the sheet of paper, mark the water front advancement every 10 seconds for 1min30 and then every 30 seconds until the front reaches the end of the absorbent pad (or until the front is no more moving forward).
6. After the 6 tests, measure the spacing between the marks and encode them in a plotting software to obtain the capillary flow curves.

2.3 Evolution of NP solutions in LFA assemblies

Five nanoparticle solutions were deposited onto the LFAs, namely commercial AuNPs in water, homemade AuNPs (MR 2.3) in water, commercial MNPs in EtOH, MNP-CPs in EtOH and MNP-TDs in n-hexane.

For each solution, one strip of 7 mm width was manufactured following the procedure described in section 2.1. However, the dimensions of the pads were different than in Figure 3.1, imposed by the release liners of the adhesive card. Information regarding the lengths and the papers of the pads is gathered in Table 3.5.[3] An overlap of 2 mm was kept. Apart from the type of solution dropped onto the sample pad, the procedure was similar to the one described in section 2.2.

Table 3.5: Pad lengths and materials for the microfluidic tests with NPs.

Pad	Material	Pad length [mm]
SP	ReliaFlow^{TM} 601	13.5
CP	ReliaFlow^{TM} 8950	6.5
M	Unisart® CN95	26.5
AP	ReliaFlow^{TM} 237	13.5

---

[1] The sample should be added dropwise to avoid overflow of the sample on top of the conjugate pad and the membrane. This ensures that the front moves across the different pads exclusively by capillarity.

[2] It was nearly impossible to measure the evolution of the front precisely in the CP or SP since the capillary flow was too fast.

[3] Cellulose purchased from Merck-Millipore was used instead of the cotton fiber from Ahlstrom-Munksjö considered before because, as it will be shown in the next sections, the microstructure of the former is analyzed by SEM. Hence, correlations between the evolution of NPs in the strips and the microstructure of the cellulose can be done.

3 Characterization techniques

Characterization of nanoparticles is not straightforward and requires different techniques to be compared in order to draw thorough conclusions. To this end, the main advantages and drawbacks of the techniques used in this study are introduced hereafter. This gives a first overview of the reason which these techniques were used. Afterwards, their working principles and the sample preparations they require are presented in details.

- Transmission Electron Microscopy (TEM) provides an overview of the size, shape, dispersion and polydispersity of nanoparticles. However, the number of nanoparticles observed at the same time might not always be representative of the whole batch. Furthermore, their surface properties are not always very clear.
- Dynamic Light Scattering (DLS) considers much more NPs in solution to assess an average particle size. Polydispersity and aggregate size can also be determined. However, distinction between individual and aggregated NPs is not always clear.
- Ultraviolet-Visible (UV-Vis) spectroscopy qualitatively describes the size, dispersion and polydispersity of NPs. The shape of the curve can also be qualitatively associated to the composition, size and color of the NPs. When calibrated, it can also semi-quantify the concentration of particles in solution[1].
- Scanning Electron Microscopy (SEM) provides precise information regarding the surface topography of NPs with > 100 nm sizes. Below, they cannot be clearly characterized due to the limited resolution. SEM is often coupled with EDX to assess the surface composition of the particle.
- X-ray Diffraction (XRD) gives precise information regarding the phase composition and crystallite sizes of nanoparticles. The latter can be correlated to the size of the NPs, provided that they are made of single crystals, which cannot be ensured by this technique. In addition, it will be shown that the distinction between different phases is not always clear.

In addition, some characterization techniques involve an incident electron beam hitting the sample. The effects of this electron bombardment are summarized in Figure 3.2 and will be used throughout the different sections. Particular attention will be paid to X-rays, secondary electrons, backscattered electrons and transmitted electrons.

3.1 Transmission Electron Microscopy (TEM)

Transmission electron microscopy (TEM) provides an image of the sample on a nanoscale. A typical set-up is shown in Figure 3.3a. As in SEM, an electron beam is emitted from a cathode filament (electron source) towards an anode. The beam is then focused in a very fine spot size with a condenser lens. Upon hitting the sample, parts of the electrons are transmitted, depending on its thickness and electron transparency. This transmitted portion is focused by the objective lens into a real intermediate image. The image then passes through the intermediate and projector lenses, where it is enlarged, and finally strikes a fluorescent screen, where the user can see the image.

---

[1] To this end, a calibration curve must be set up beforehand, based on a sample with a known concentration of AuNPs. Afterwards, the height of the characteristic peak at 520 nm can be correlated with the concentration of AuNPs in the analyzed sample [145]. However, this was not done in this study, since neither the concentration of AuNPs in the commercial solution nor in the homemade ones was known.

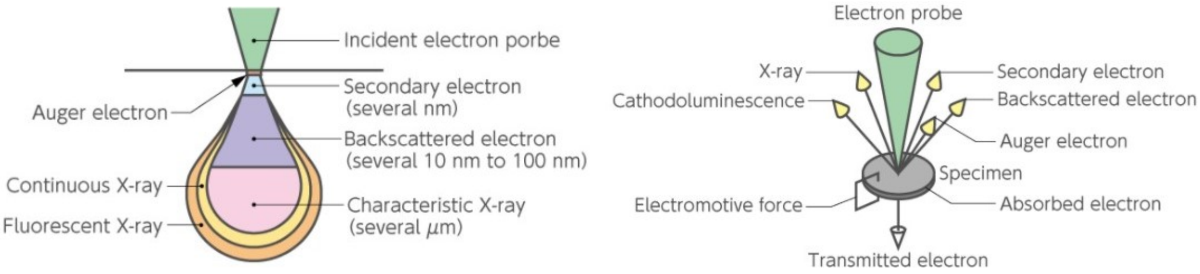

(a) (b)

Figure 3.2: Summary of signals generated by the incident electron beam hitting the sample (a) Depth of quantum emission and spatial resolution, (b) Information obtained from specimen [146].

The quality of the final image depends on the accuracy of the mechanical and electrical adjustments with which the various lenses are aligned to one another. Moreover, lighter (resp. darker) areas on the image represent areas of the sample where more (resp. fewer) electrons were transmitted through it [147, 148].

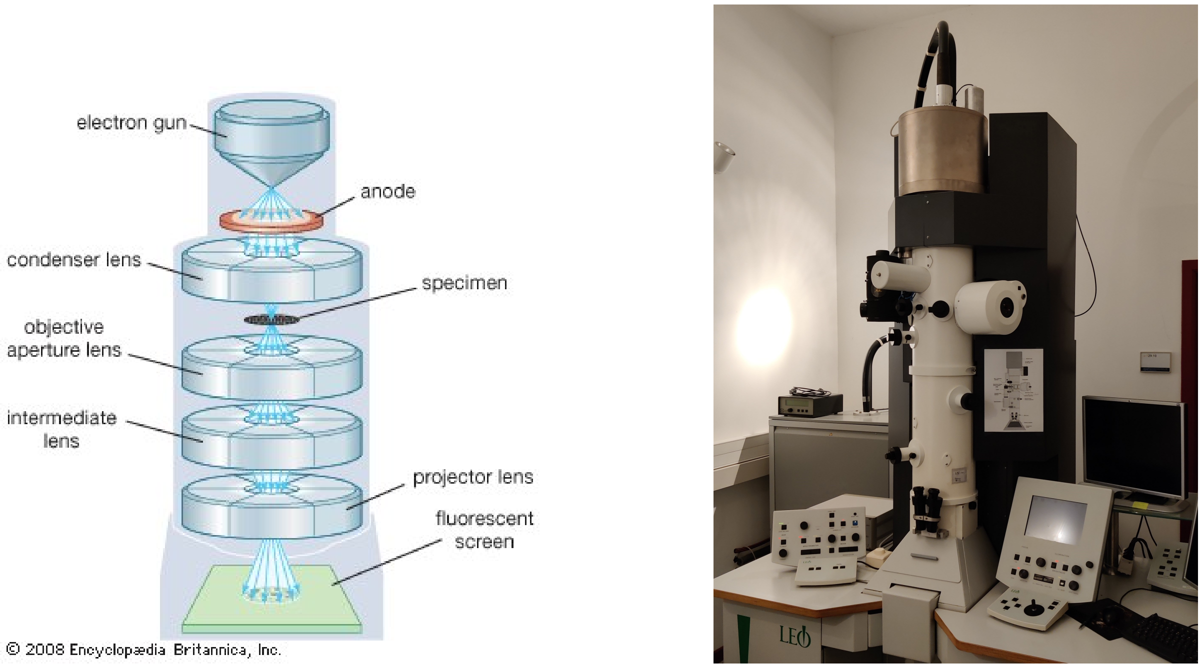

(a) (b)

Figure 3.3: (a) Schematic set-up of a TEM, taken from [148], (b) LEO 922 OMEGA Energy Filter Transmission Electron Microscope

Transmission electron microscopy (TEM) was performed by Dr. Tommy Haynes on a LEO 922 OMEGA Energy Filter Transmission Electron Microscope operating at 120 kV. Sample preparation consisted of dispersing a few milligrams of each sample in an appropriate solvent (e.g. DI water or EtOH) and sonicating the sample for 30 minutes sonication (VWR Ultrasound cleaner, power level 9). Then, one drop of the supernatant were placed on a holed carbon film deposited on a copper grid (CF-1.2/1.3-2 Cu-50, Electron Microscopy Sciences, C-flat$^{\mathrm{TM}}$, Protochips, USA). The grid was carefully deposited on a filter paper to absorb the excess sample and dried overnight in a petri dish at room temperature.

3.2 Dynamic Light Scattering (DLS)

Dynamic light scattering (DLS) measures the size and size distribution of particles dispersed in a liquid down to 1 nm. A schematic representation of the setup is shown in Figure 3.4. By illuminating the sample with a laser, the photon detector measures the Brownian motion of the particles and analyses the intensity of the fluctuations in the scattered light. The Brownian motion of the particles is due to random collisions of the particles with the surrounding liquid molecules or with neighbouring particles. The analysis of the intensity of fluctuations yields the speed of the Brownian motion through the diffusion coefficient D (m^2 s^{-1}). Hence, with the Stokes-Einstein equation (Eq. 3.2), the particle size d (nm) is obtained, where k_B is the Boltzmann constant, T is the temperature and η is the viscosity of the liquid (Pa·s). The motion of small particles is thus faster than that of large particles.

$$d = \frac{k_B T}{3\pi\eta D} \tag{3.2}$$

In the end, the DLS measurement provides the normalized scattered light intensity (a.u.) as a function of the particle diameter (nm). Thus, the higher the peak at a certain size, the higher the number of particles of that size in the sample. Furthermore, the narrower the peak, the more particles have the same size and thus the more monodisperse the nanoparticles are [149, 150].

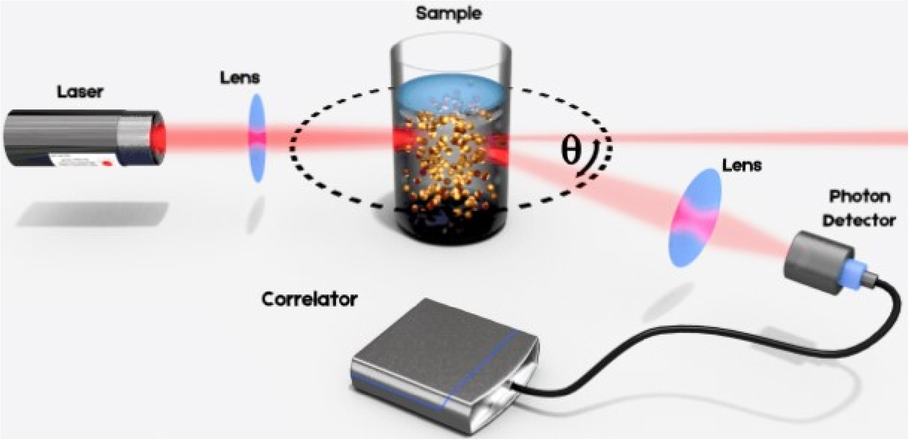

Figure 3.4: Schematic representation of the dynamic light scattering (DLS) setup [149].

In this study, DLS analyses were performed on a CGS-3 Compact Goniometer System (ALV, Germany) equipped with a LSE-5003 light scattering electronics and multiple tau digital correlator. Data were analyzed using the ALV-5000 & 60X0 Software (ALV, Germany).

Sample preparation consisted of dispersing a few milligrams of each sample in an appropriate solvent (e.g. DI water or EtOH) and sonicating it for 30 minutes (VWR Ultrasound cleaner, power level 9). The supernatant was introduced in the machine with an appropriate glass test tube. After choosing the appropriate solvent in the software, the measurements were carried out three consecutive times and once after waiting 5 minutes.

3.3 Ultraviolet-visible spectroscopy (UV-Vis)

Ultraviolet-visible (UV-Vis) spectroscopy provides information about the light absorption of a sample as a function of the incoming wavelength λ (nm). The light absorption A^λ (-) for a given λ is given by the Beer-Lambert law (Eq. 3.3), where I is the intensity of light measured after interaction with the sample, I_0 is the incident intensity, ε^λ ($M^{-1}cm^{-1}$) is the molar absorptivity coefficient of the sample, c (M) is the concentration of absorbing substance and l (cm) is the path length of light through the sample [151, 152].

$$A^\lambda = -\log_{10}\left(\frac{I}{I_0}\right) = \varepsilon^\lambda c l \leq 1 = 100\% \tag{3.3}$$

A typical set-up of spectrophotometers is represented in Figure 3.5. The light emitted by the light source (typically tungsten filament lamp or deuterium lamp) first enters the monochromator. The entrance slit narrows the beam to a usable size, the prism separates the white light into bands of monochromatic light of a single wavelength and the exit slit is configured to select the desired monochromatic wavelength. After passing through the sample, the transmitted light hits the detector, which will quantify the light intensity I (*i.e.* the number of photons) and convert it into an electrical signal. The detectors are typically photo tubes, photomultipliers or photodiodes. By playing with the exit slit, different light wavelengths can be chosen and the whole spectra can be analyzed [152, 153].

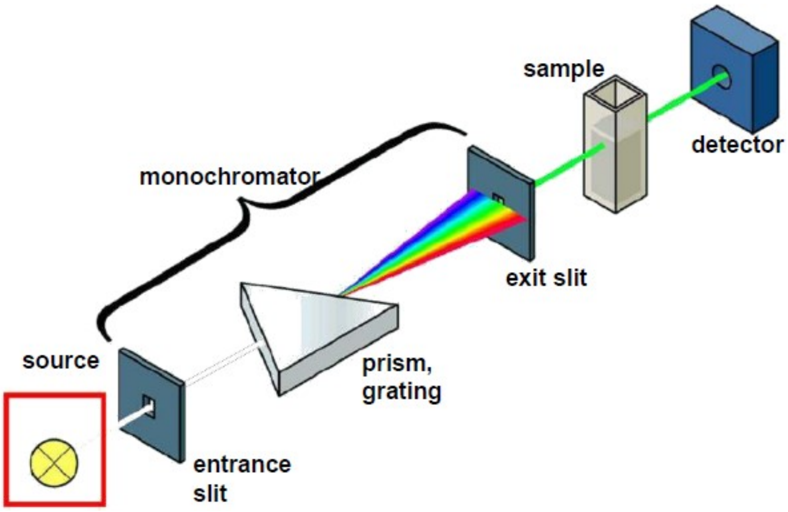

Figure 3.5: Schematic representation of a UV-Vis spectrophotometer, taken from [154].

UV-visible spectroscopy analyses were performed on a 1700 UV/visible spectrophotometer from Shimadzu®. Sample preparation consisted of dispersing a few milligrams of each sample in an appropriate solvent (e.g. DI water or EtOH)[1] and sonicating the sample for 30 minutes (VWR Ultrasound cleaner, power level 9). The sample was then transferred in a PMMA cuvette (BRAND® UV cuvettes, 1 cm, 3 mL). After configuring the baseline with the pure solvent in which the sample was dispersed, the analysis was made on a spectra range from 200 to 800 nm. The data was finally collected using the UV-Probe software.

---

[1] If the sample is stored as a powder, which is not the case for AuNPs for example.

3.4 Scanning Electron Microscopy (SEM)

Scanning electron microscopy (SEM) is a characterization technique offering high magnification surface characterizations with a great depth of field, as well as elemental composition analysis when coupled with Energy-dispersive X-ray spectroscopy (EDX), introduced in the next section 3.5.
A typical set-up is shown in Figure 3.6a. An electron beam is typically emitted from a cathode filament (electron source) towards an anode. The beam is then focused in a very fine spot size with condenser lenses and subsequently deflected on the sample surface with an objective lens and scan coils. When the beam hits the sample surface, it generates secondary electrons (cfr. Figure 3.2) which are then detected by a scintillator-photomultiplier component (secondary electron detector) to produce an image of the surface.

As shown in Figure 3.2a, since secondary electrons come from several nm within the surface, the brightness of the signal depends on the surface exposed to the primary beam. Hence, steep surfaces and edges tend to be brighter than flat surfaces because of this so-called edge effect.
EDX is often coupled with SEM because the primary electron beam also generates X-rays. In addition, as shown in Figure 3.6a, back-scattered electrons can also be detected in SEM, although topological contrast is less pronounced than with secondary electrons [147].

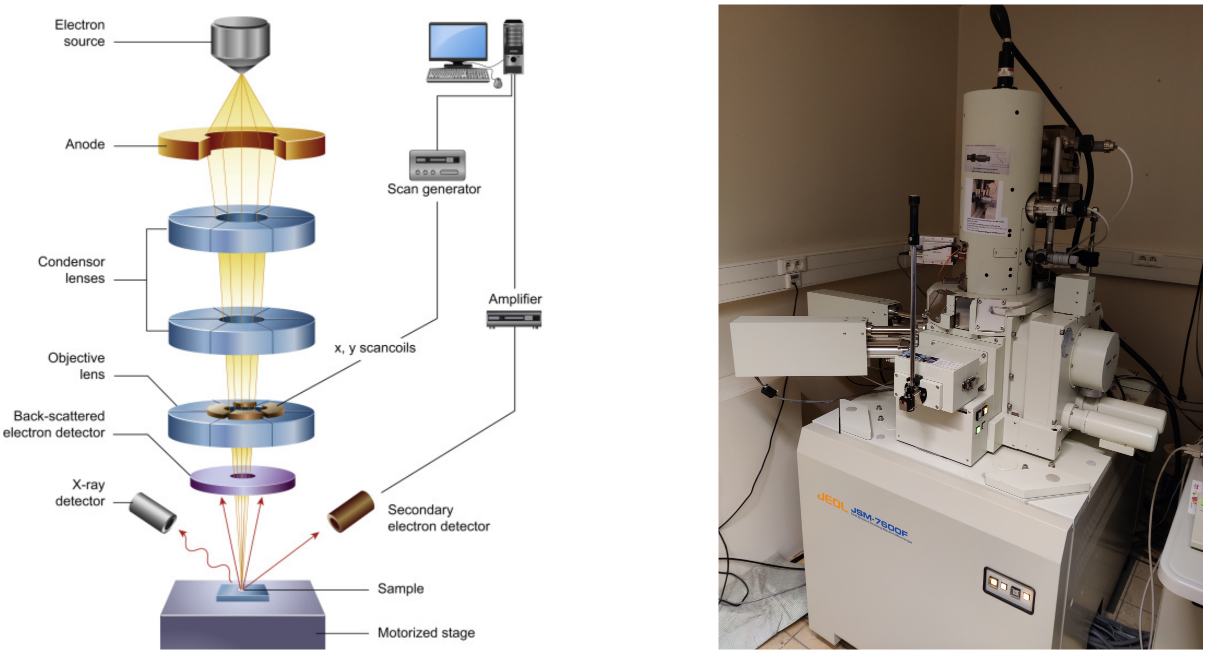

(a) (b)

Figure 3.6: (a) Schematic set-up of a SEM, taken from [155], (b) JEOL® JSM-7600F SEM.

In this study, SEM analyses were performed by Delphine Magnin on a JEOL® JSM-7600F, shown in Figure 3.6b. The instrument could perform between 0.1 and 30 kV. The higher the voltage, the higher the energy of the electron beam and thus the deeper the analysis in the sample.
The non-metallic samples (*i.e.* the different papers) were prepared by Delphine Magnin and consisted of a metallization of the sample with a gold coating of 8 nm, deposited with a plasma evaporator. The coating should not affect the characterization of the sample up

to x50000 magnification, from which gold grains might appear on the images. Chromium coating is also possible but tends to oxidize with time, in opposition with gold. Metallic samples such as iron-oxide or gold nanoparticles did not need any metallization and were analyzed on a holed carbon film deposited on a copper grid (CF-1.2/1.3-2 Cu-50, Electron Microscopy Sciences, C-flat^{TM}, Protochips, USA), usually used for transmission electron microscopy (TEM).

3.5 Energy-dispersive X-ray spectroscopy (EDX)

Energy dispersive X-ray spectroscopy (EDX) is a technique that is typically performed in association with a scanning electron microscope (SEM), which was introduced in section 3.4. As shown in Figure 3.7, when an incident electron (in orange) kicks an inner electron out of the atom, it creates a void on an electron shell (K, L, M, ...). Consequently, an electron from an outer shell will migrate to this void and release its excess energy in the form of an X-ray.

EDX utilizes these X-rays emitted from the sample to characterize the elemental composition of the sample. The energy of the X-ray is characteristic of the element which emitted it. Hence, EDX measures the number of emitted X-rays versus their energy in order to provide information about the elements present in the sample [147].

The EDX used in this study was implemented within the scanning electron microscope (SEM) JEOL® JSM-7600F and will thus be called SEM-EDX in the next chapters. The sample preparation is thus the same as the one for the SEM (cfr section 3.4). A fitting coefficient of 0.4019 was used for the bremsstrahlung.

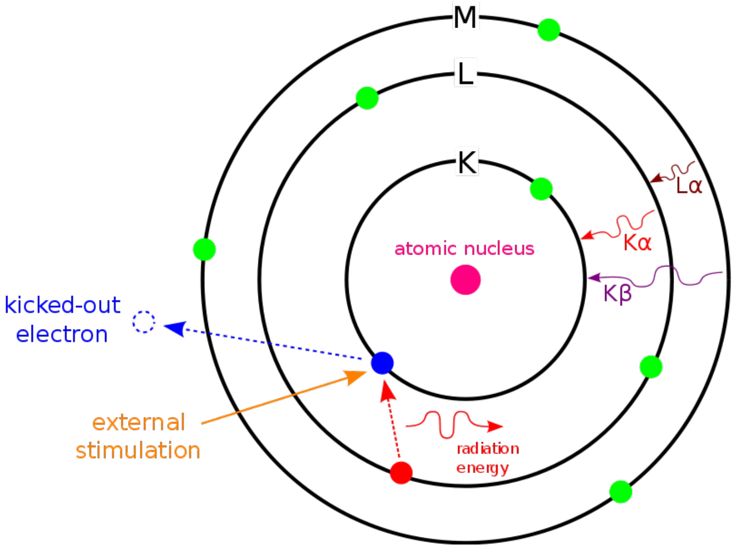

Figure 3.7: Principle of EDX, taken from [156].

3.6 X-ray Diffraction (XRD)

X-ray diffraction (XRD) provides information about the crystalline structure of the sample, *i.e.* lattice parameters, size of crystalline phases, presence of metallic phases, presence of imperfections, degree of crystallinity, etc.

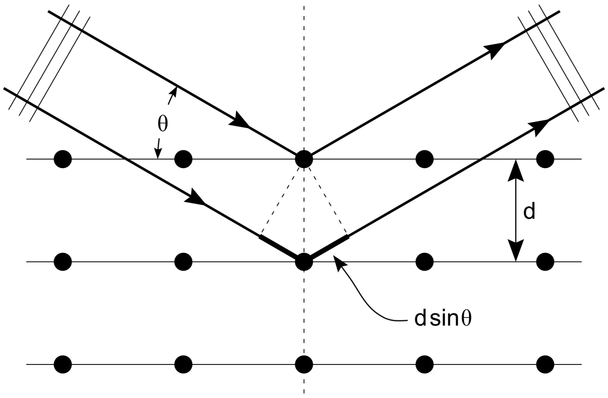

Figure 3.8: Schematic representation of X-ray diffraction on a crystal lattice, taken from [157].

A schematic representation of the XRD working principle is shown in Figure 3.8. An X-ray source bombards the sample with X-rays of wavelength λ (nm). The latter is then diffracted given Bragg's law (Eq. 3.4), where n (-) is the diffraction order, d (nm) is the distance between two successive layers of atoms and θ (°) is the angle of incidence [157].

$$n\lambda = 2d\sin\theta \tag{3.4}$$

Once the measurement done, a diffractogram made of peaks with different intensities is obtained. It represents the crystallographic identity card of the sample. Afterwards, the latter can be compared with reference patterns in order to identify the species and phases present in the sample.

Finally, the nanoparticle crystallites size D (nm) can be calculated with Scherrer's equation (Eq. 3.5), where k is a shape factor taken as 0.89 in this study, λ (nm) is the wavelength of the incident X-rays, β (°) is the full width at half maximum of the diffraction peak after correction of the instrumental broadening and θ (°) is the diffraction angle [158].

$$D = \frac{k\lambda}{\beta\cos\theta} \tag{3.5}$$

Diffractograms were collected by Dr. Julien Mahy using a D8 Advance (Bruker, USA) diffractometer equipped with a Cu-Kα (0.15409 Å) anode and a LynxEye detector. A few milligrams of each sample were deposited on an epoxy sample holder, previously covered with a very thin layer of commercial moisturizer (Nivea®). Data were collected for 2θ values ranging from 5° to 80°, with a step of 0.15° and a time/step of 0.15 s at room temperature. The obtained 2D diffractograms were analyzed using the DIFFRAC.EVA software (Bruker, USA), azimuthally integrated using the Fit2D software and calibrated with a LaB6 standard diffractogram.

Chapter 4

Results

Within the development of low-impact paper-based biosensors for bacteria detection in water samples, this study aims at better understanding the role of nanoparticles in lateral flow assays. As a reminder, nanoparticles are the main signal transducers of biosensors. Their unique properties make it possible to implement electrical and magnetic detection methods in addition to the more widespread colorimetric one in order to provide quantitative results. This chapter groups the results of this study that are discussed in Chapter 5. First, gold and magnetic nanoparticles are synthesized, functionalized, characterized and compared with commercial units. Then, the microstructure of the papers and their microfluidic properties are analyzed with and without nanoparticles.

1 Nanoparticles for LFAs

In the following, gold and iron-oxide magnetic nanoparticles are investigated in depth. Their synthesis and functionalization are studied up to the stage of preparation for further conjugation with bioreceptors.

1.1 Gold nanoparticles

Gold nanoparticles (AuNPs) are the most common NPs used in biosensing applications because of their biocompatibility, intense red color, interesting electrical properties and relatively simple production.
In this section, AuNPs synthesized with the Turkevich method are characterized by TEM, DLS and UV-Vis spectroscopy at first. They are further called "homemade AuNPs". Then, commercial AuNPs provided by Unisensor® are characterized in the same way.

1.1.1 Homemade AuNPs

Five homemade gold nanoparticles solutions were synthesized with different molar ratios (MR) of NaCt to gold precursor ($HAuCl_4$). One of them in shown by TEM in Figure 4.1 for a MR of 2.3. The black spheres indicate the gold spheres with various sizes depicted by black arrows. Different sizes in the range of 10 to 30 nm are observed. The nanoparticles are overall well dispersed.
Figure 4.2 shows the DLS curves for the five investigated MR. As a general comment, it should be noted that the latter characterization technique is qualitative. Only the breadth and position of the peaks can be compared between different samples. Larger areas under the curve do not mean that there are more nanoparticles in the analyzed sample.

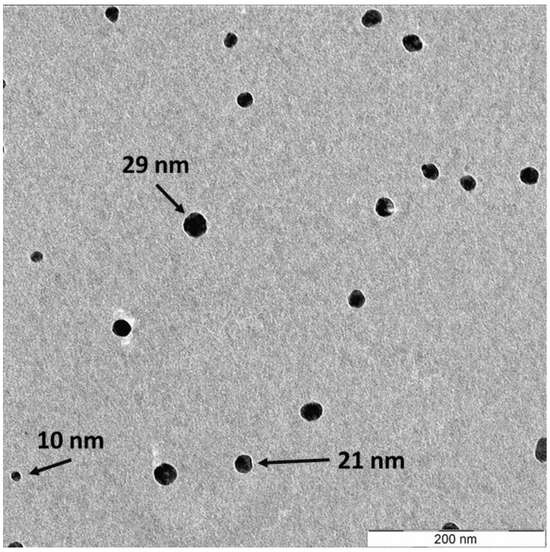

Figure 4.1: TEM image of the homemade AuNPs synthesized with a MR of 2.3. Some particle sizes are indicated by black arrows.

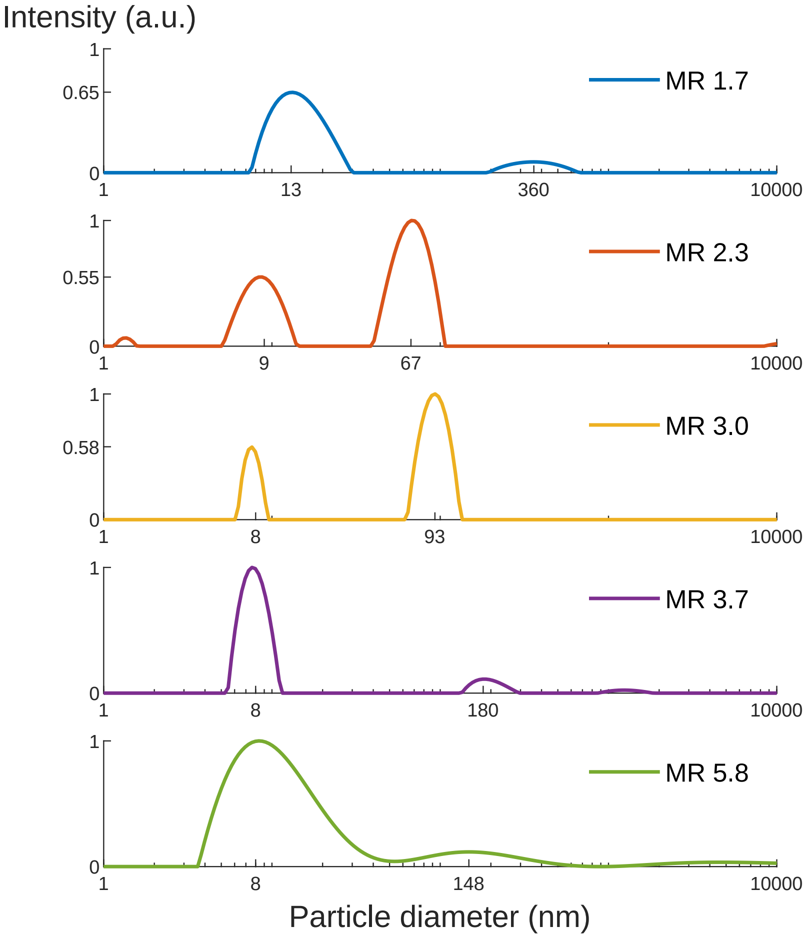

Figure 4.2: Particle size distribution of the homemade AuNPs synthesized with different MR.

The DLS curves from Figure 4.2 reveal bimodal distributions for each batch, with a first peak around 10 nm and a second one above 50 nm. The first peak shifts from 13 to 8 nm as the MR increases from 1.7 to 5.8, which indicates that the synthesized AuNPs get smaller correspondingly.
Moreover, the breadth of the first peak decreases as the MR increases from 1.7 to 3.7 and increases again thereafter. This indicates that the AuNP solutions become more monodisperse except for a MR of 5.8. Finally, the height of the second peak decreases compared to the first one as the MR increases from 2.3 to 5.8.

The characteristic UV-Vis curves of the different homemade AuNPs can be seen in Figure 4.3. For each investigated MR, the absorption curve adopts the typical shape of AuNPs described in section 2.3. Three main characteristics are observed: (i) non-zero absorption towards UV wavelengths, (ii) the characteristic absorption peak at 521 nm, (iii) zero absorption from 600 nm to the infrared rays which accounts for the red color of AuNPs.
Data below 300 nm is not provided because the PMMA flask containing the sample in the spectrometer interferes with the AuNPs and falsifies the data. The height of the peak decreases with the MR from 3.7 to 1.7. The curves peak at 514 nm for each batch except for 1.7 whose peak is shifted to 521 nm. Finally, the breadths of the MR 1.7 and 5.8 peaks are larger than the other ones.

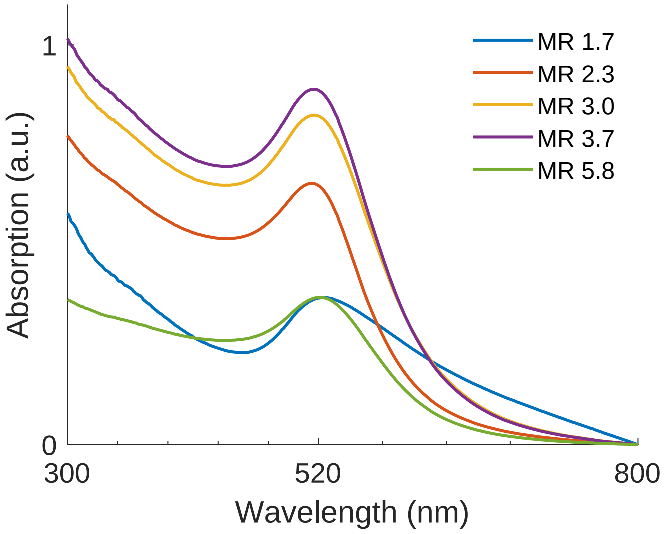

Figure 4.3: Absorption spectrum obtained by UV-Vis spectroscopy for the homemade AuNPs synthesized with different MR.

1.1.2 Commercial AuNPs

Figure 4.4 shows the TEM micrograph of the commercial AuNPs provided by Unisensor® and stabilized with NaCt. They have a spherical shape and are well dispersed. Some particle sizes measured by the TEM software are marked with the black arrows. Overall, they have monodisperse sizes.

The DLS curve shown in Figure 4.5a represents the particle size distribution of the commercial AuNPs. One narrow peak is observed, which indicates that the AuNPs have uniform sizes around 35 nm.

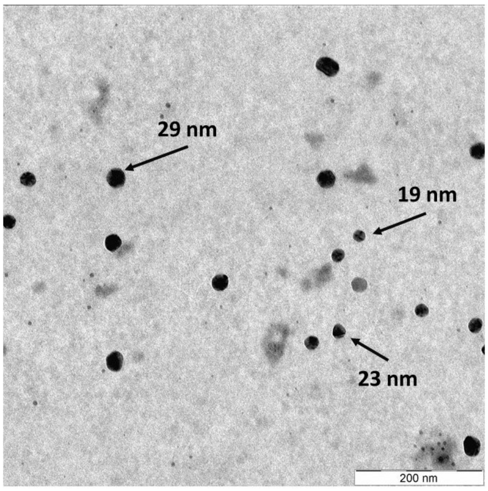

Figure 4.4: TEM image of the commercial AuNPs. Some particle sizes are indicated by black arrows.

The UV-Vis spectrum of the commercial AuNPs shown in Figure 4.5b reveals the three main characteristics, including a non-zero absorption towards UV wavelengths, the absorption peak at 521 nm and zero absorption from 600 nm to the infrared rays.

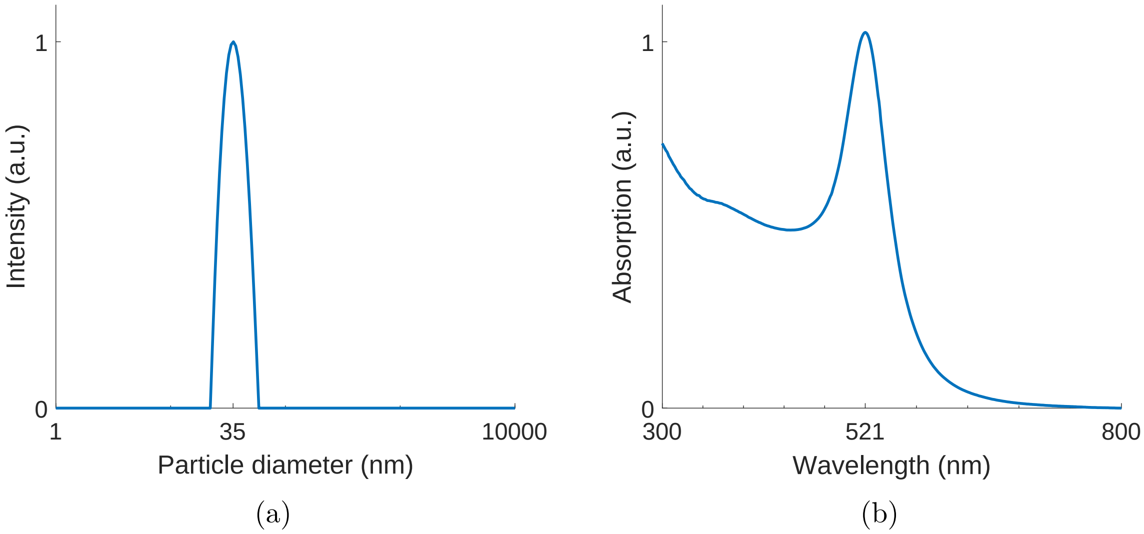

Figure 4.5: Characterization of the commercial AuNPs by (a) DLS and (b) UV-Vis spectroscopy.

1.2 Magnetic nanoparticles

Iron-oxide nanoparticles offer colorimetric and magnetic detection opportunities to LFAs, as well as pre-concentration of the sample to increase the test sensitivity. In what follows, magnetic cores were first synthesized and then coated with silica for further bio-conjugation.

1.2.1 MNP synthesis

Four different iron-oxide magnetic nanoparticles are investigated and characterized below. First, MNPs synthesized by co-precipitation (MNP-CP), thermal decomposition (MNP-TD) and hydrothermal method (MNP-H) are characterized, followed by commercial MNPs.

Co-precipitation

The TEM image in Figure 4.6a shows the iron-oxide magnetic nanoparticles synthesized by co-precipitation (MNP-CP). The dark area in the lower right corner corresponds to a cluster formed by many aggregated nanoparticles. It appears very dark since the electrons from the TEM beam could not be transmitted through it. Small spherical particles are observed at the edge of the aggregate. The grey and white backgrounds represent the carbon film of the TEM grid and one of its hole, respectively.

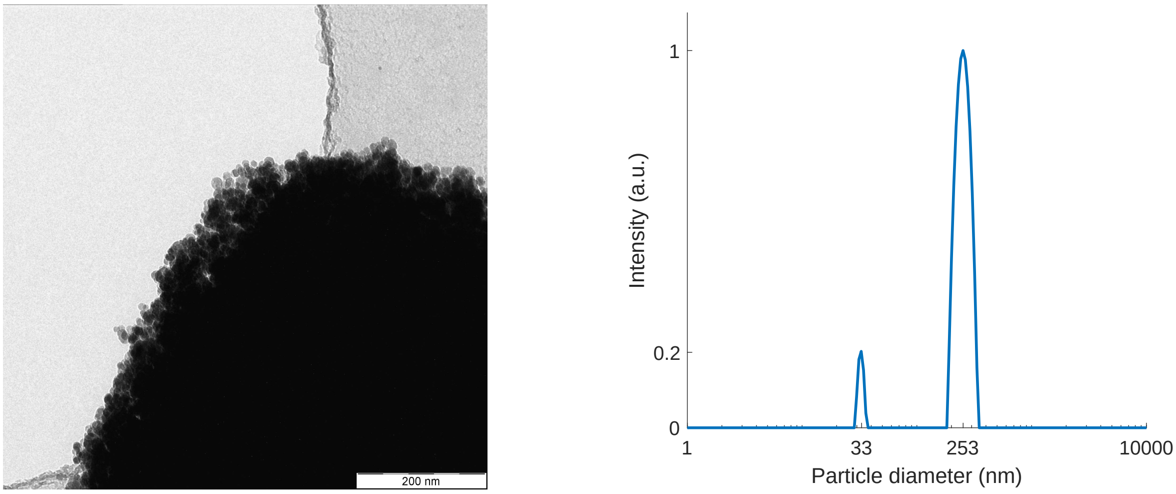

(a) (b)

Figure 4.6: Characterization of MNP-CPs by (a) TEM and (b) DLS.

The DLS curve in Figure 4.6b shows a bimodal particle size distribution for the MNP-CPs. Two peaks at 33 nm and 253 nm are observed. While the former cannot be associated to the average particles size or to small aggregates of several NPs, the latter relates the presence of large aggregates. The intensity of the peaks indicates that the presence of clusters is very important.

The XRD diffractograms shown in Figure 4.7 provides information regarding the phase composition of the MNPs obtained by co-precipitation. The pattern of the MNP-CPs is provided alongside the reference ones of magnetite (Fe_3O_4) and maghemite (γ-Fe_2O_3). The two latter phases have very close patterns. The peaks of the XRD pattern match the peaks of magnetite and maghemite. It cannot be concluded whether the MNP-CPs are totally made out of magnetite, maghemite or out of a binary mixture of both phases.

With Scherrer's formula (Eq. 3.5), the average size of the iron-oxide crystallites is estimated to be equal to 14.2 nm. Detailed calculations are provided in Appendix B.

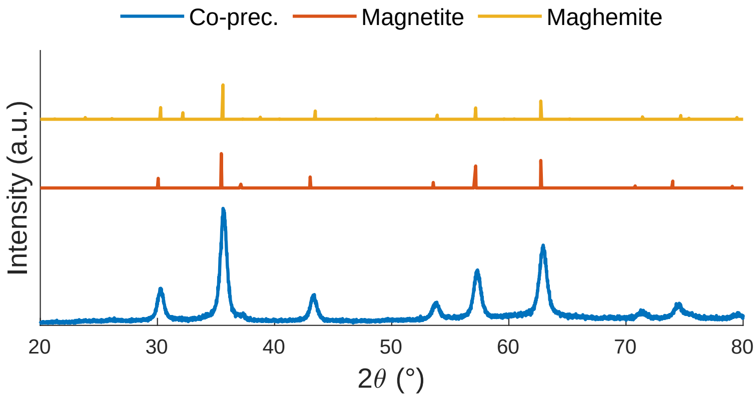

Figure 4.7: XRD diffractogram of the MNP-CPs alongside the reference patterns of magnetite and maghemite.

The DLS curves in Figure 4.8 show the effect of surfactants on the MNP-CP size distribution. On the one hand, it appears that PVP leads to a bi-modal size distribution with one peak at 200 nm and one at 1281 nm. On the other hand, CTAB also leads to a bi-modal size distribution with aggregates sizes around 844 nm. In both cases, the addition of surfactants increased the size of the aggregates significantly.

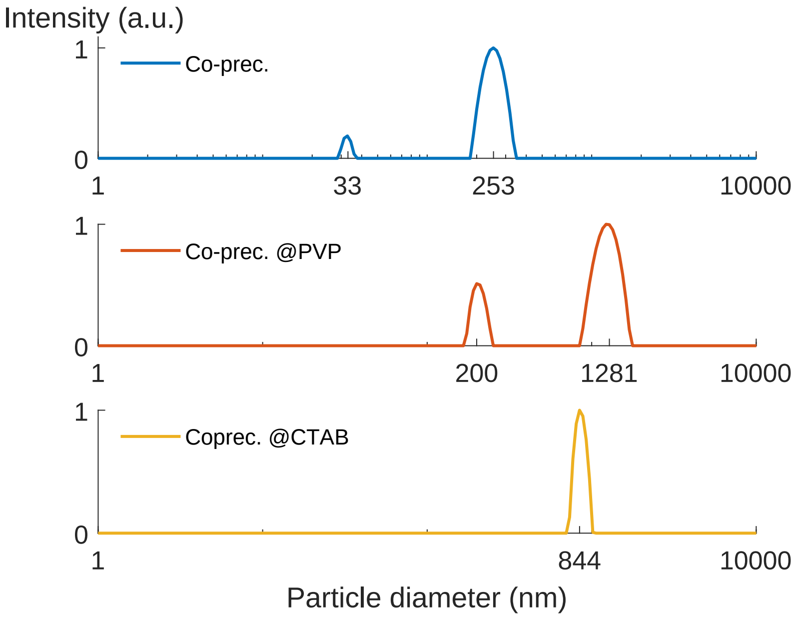

Figure 4.8: DLS curve of the MNP-CPs with and without addition of surfactants (PVP and CTAB).

Thermal decomposition

The TEM micrographs of the MNPs synthesized by thermal decomposition (MNP-TD) shown in Figure 4.9a reveal dispersed nanoparticles with various shapes (spherical, triangular, hexagonal, ...). Some particles are very small compared to the other ones.

The DLS curve in Figure 4.9b reveals three peaks in the MNP-TD size distribution. A first narrow peak at 13 nm is observed, while two significantly smaller peaks at 78 and 1840 nm probably correspond to clusters.

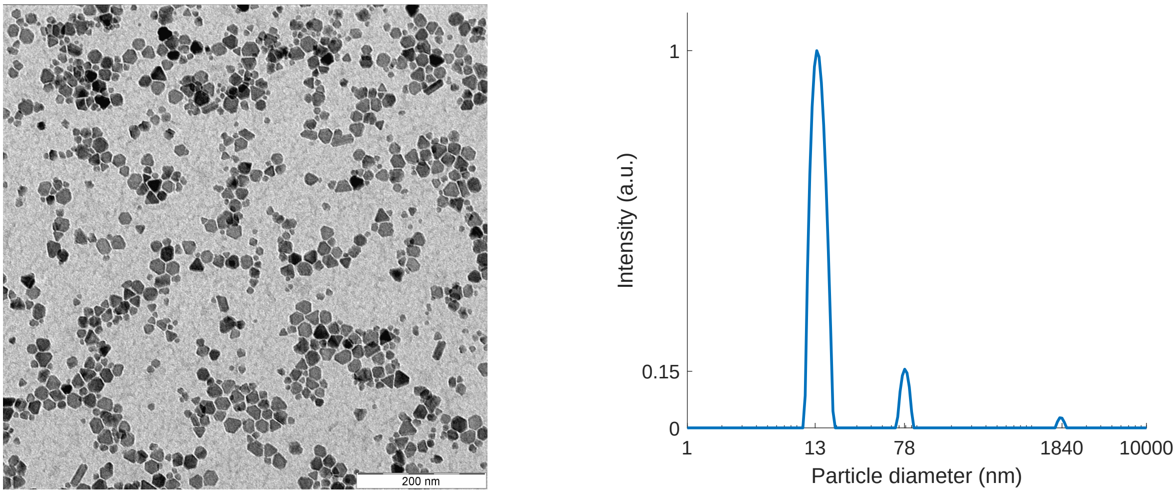

(a)

(b)

Figure 4.9: Characterization of MNP-TDs by (a) TEM and (b) DLS.

Figure 4.10 represents the XRD diffractogram of the MNP-TDs alongside the reference patterns of magnetite (Fe_3O_4) and maghemite (γ-Fe_2O_3). It cannot be concluded whether the MNP-TDs are totally made out of magnetite, maghemite or out of a binary mixture of both phases.
Using Scherrer's formula (Eq. 3.5), the average size of the iron-oxide crystallites is estimated to be equal to 12.4 nm. Detailed calculations are provided in Appendix B.

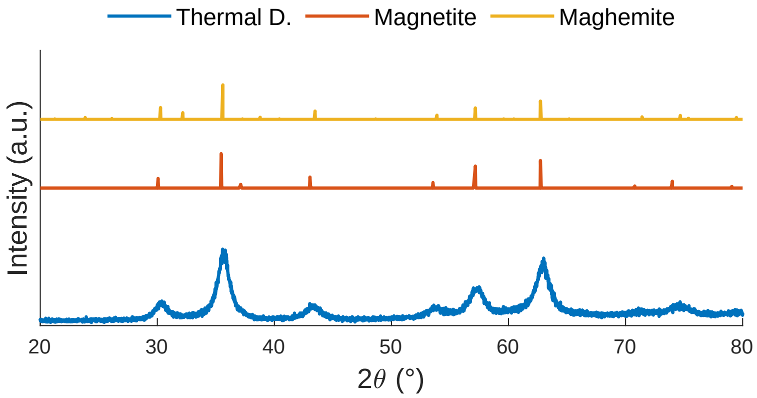

Figure 4.10: X-ray diffraction pattern of the MNP-TDs with reference patterns of magnetite and maghemite.

Hydrothermal

The MNPs obtained by hydrothermal method (MNP-H) are shown on the TEM micrograph in Figure 4.11a. Many small seeds of 2-5 nanometers and well dispersed are observed. Some slightly larger black particles reaching sizes of maximum 10 nm can also be seen.

Figure 4.11b shows the particle size distribution of the MNP-H measured by DLS. The broad peak indicates the presence of aggregates of various sizes around 375 nm.

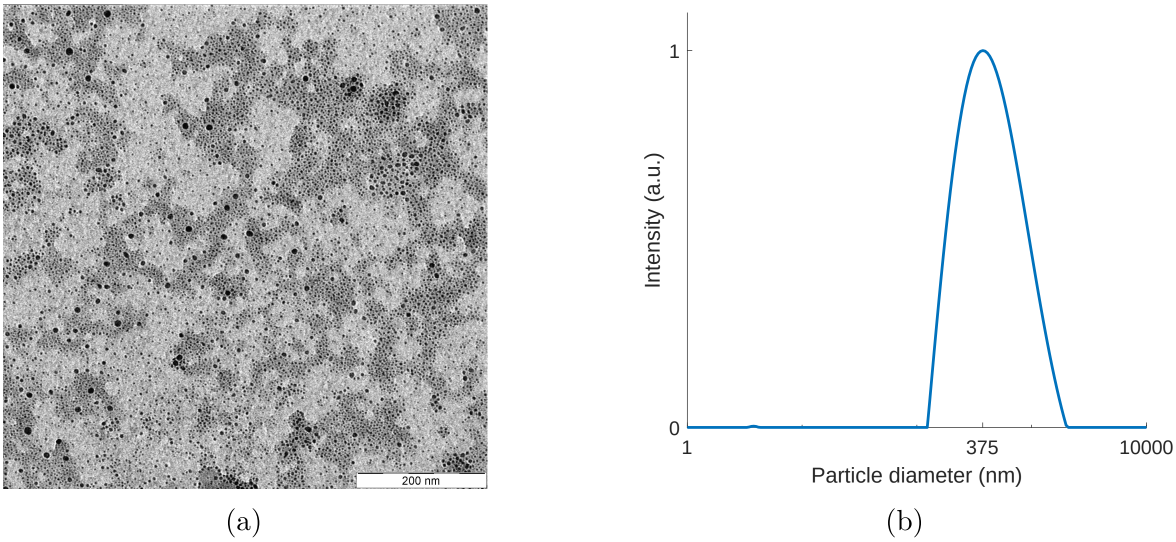

(a)

(b)

Figure 4.11: Characterization of the MNP-Hs by (a) TEM and (b) DLS.

Commercial MNPs

The TEM image in Figure 4.12 represents the commercial magnetic nanoparticles (Iron(II,III) oxide nanopowder, 50-100 nm particle size (SEM), 97% trace metals basis) purchased from Sigma-Aldrich®. The nanoparticles are more or less spherical. They have different sizes ranging from 100 to 200 nm and are partially agglomerated.

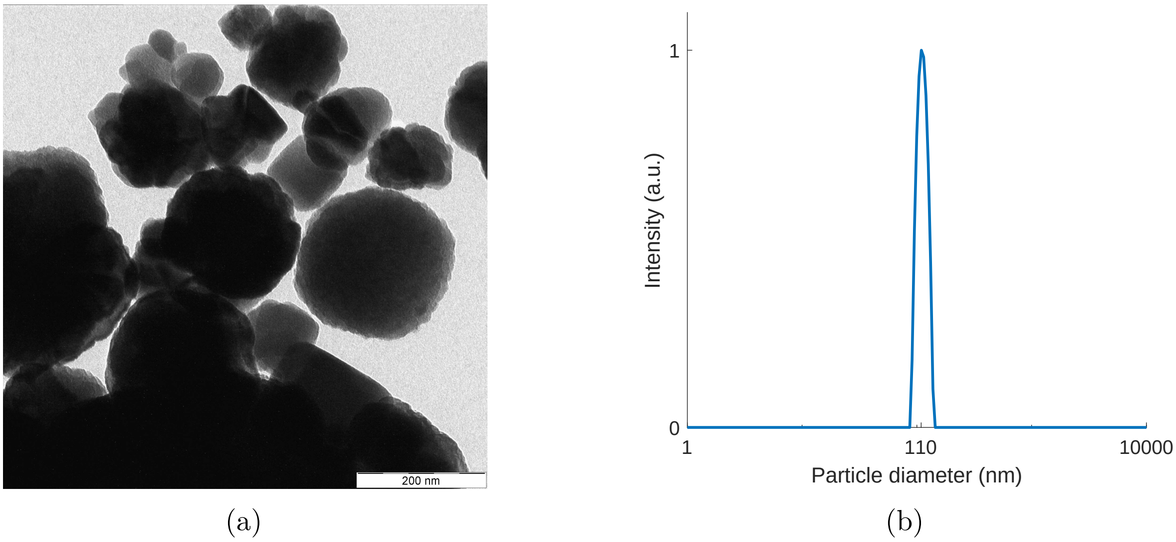

(a)

(b)

Figure 4.12: Characterization of the commercial MNPs by (a) TEM and (b) DLS.

The DLS curve in Figure 4.12b shows a single narrow peak, describing a good monodispersity of the MNPs with sizes around 110 nm, while 50 to 100 nm was specified by the supplier.

The SEM images shown in Figure 4.13 give information about the surface properties of the commercial MNPs, in addition to their size, shape and dispersion. Figure 4.13a shows that the MNPs form aggregates of 5-20 units on the TEM grid. The 1 μm holes in the carbon film can be seen in the background. The higher magnification in Figure 4.13b reveals a smooth surface of the commercial MNPs. The analyzed aggregate has a thickness of 2-3 units.

Some nanoparticles exhibit very bright edges. This is known as the edge effect and appears because more secondary electrons are released at steeper surfaces (cfr. section 3.4). Hence, these brighter areas do not mean that the composition of the MNPs changed.

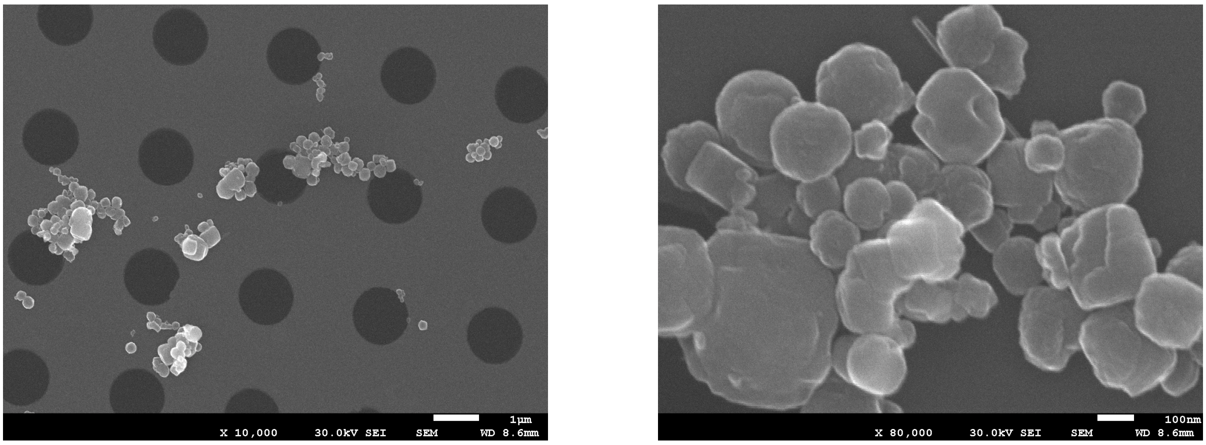

(a) (b)

Figure 4.13: SEM images of the commercial MNPs at (a) low and (b) high magnification.

The XRD diffractogram of the commercial MNPs is given in Figure 4.14, alongside the reference patterns of magnetite (Fe_3O_4) and maghemite (γ-Fe_2O_3). It cannot be concluded whether the commercial MNPs are totally made out of magnetite, maghemite or out of a binary mixture of both phases.

Using Scherrer's formula (Eq. 3.5), the average size of the iron-oxide crystallites is estimated to be equal to 67.2 nm. This can be correlated to the narrow widths of the peaks. Detailed calculations are provided in Appendix B.

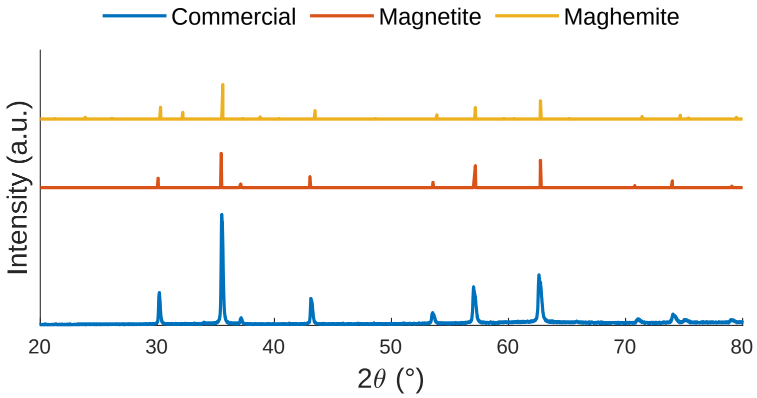

Figure 4.14: X-ray diffraction pattern of the commercial MNPs.

1.2.2 MNP @SiO_2

The MNPs presented before are coated with silica (SiO_2) by applying the Stöber method to offer functional groups for further binding with bioreceptors. The MNP-Hs are not further considered because they are too small. As a matter of fact, TEM is widely used for imaging MNP coated with silica (MNP @SiO_2) since it offers a strong contrast between the dark magnetic cores and the light silica, provided that the SiO_2 layer is thick enough.

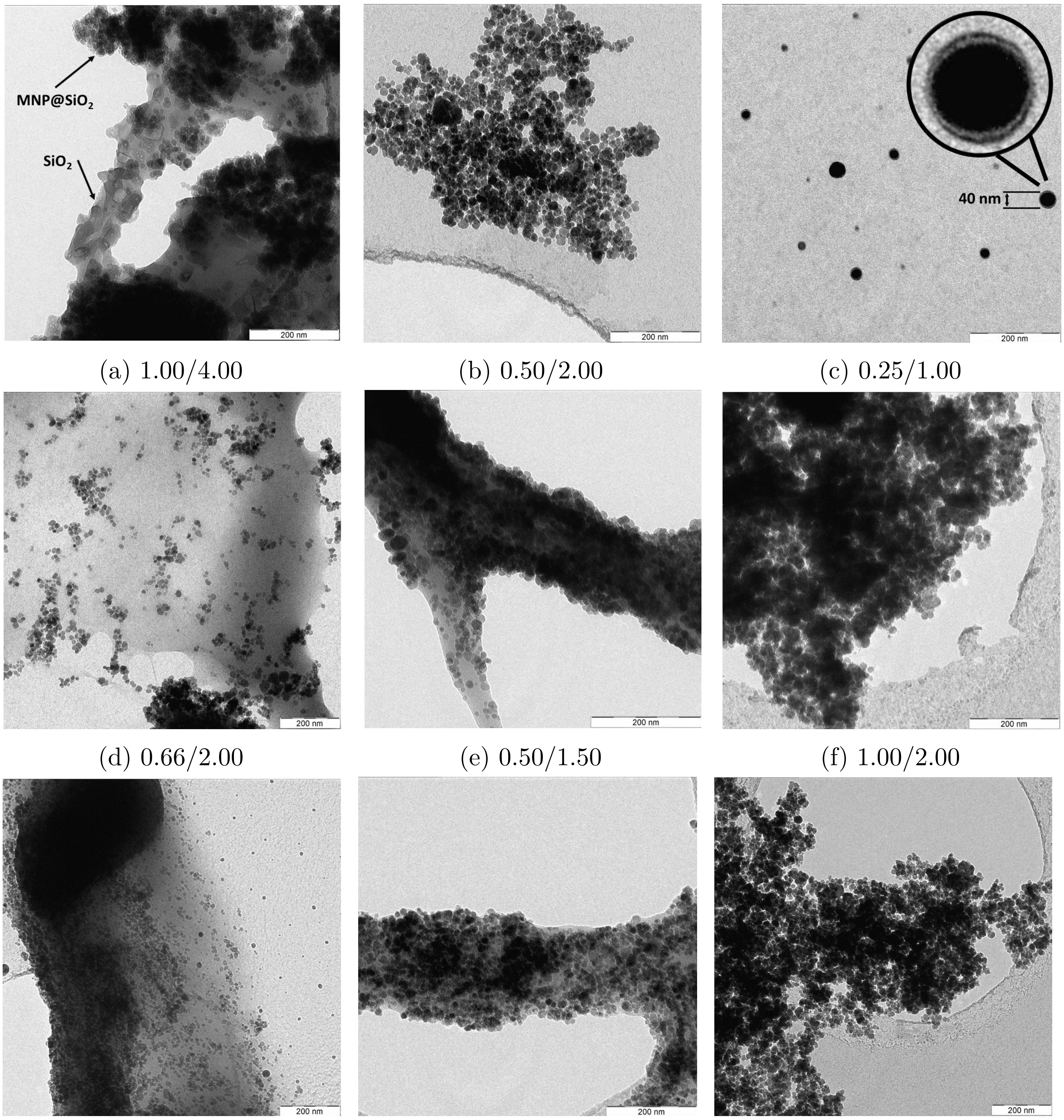

(a) 1.00/4.00 (b) 0.50/2.00 (c) 0.25/1.00

(d) 0.66/2.00 (e) 0.50/1.50 (f) 1.00/2.00

(g) 0.50/1.00 (h) 1.33/2.00 (i) 1.00/1.50

Figure 4.15: TEM micrographs of MNP-CP @SiO_2 with different AH/-TEOS volume ratios used.
For each image, the white box in the lower right corner indicates a scale of 200 nm and the respective volume ratios are mentioned in the captions.

Co-precipitation

When applying the Stöber method to the MNP-CPs, nine different volume ratios of ammonium hydroxide (AH) to TEOS are investigated, with respect to Table 3.2. The variables investigated are the absolute ratio (e.g. 1/4) and more specifically the volume ratio (e.g. 0.25/1.00 mL/mL) of chemicals used. The TEM micrographs for absolute ratios of 0.25 are shown in Figures 4.15a-c, 0.33 in Figures 4.15d-e, 0.5 in Figures 4.15f-g and 0.66 in Figures 4.15h-i.
On the one hand, the TEM micrographs in Figures 4.15b, f and i do not show any clear presence of silica. The black areas represent aggregates of MNP-CPs.
On the other hand, TEM micrographs in Figures 4.15a, d, e, g and h show large grey areas corresponding to SiO_2 puddles. The nanoparticles are not individually coated in the latter case. Instead, SiO_2 polymerized around the large clusters.
In Figure 4.15d, instead of having each MNP-CP coated with a thin silica layer, the MNPs are trapped in a large silica puddle. This is also observed in Figures 4.15e and g.
Finally, the TEM micrograph shown in Figure 4.15c shows several dispersed MNP-CP with some of them coated with a thin silica layer. An 8 times higher magnification made on a single nanoparticle is displayed on the same image. Although the contrast is low, a core-shell structure is clearly observed. The coated nanoparticles has a diameter of 40 nm and the shell thickness is equal to 4 nm. Similar observations can be done on the other nanoparticles in the same image.

One DLS measurement made on the MNP-CP @SiO_2 using a volume ratio of 1/4 mL/mL is represented in Figure 4.16. It is observed that the peak slightly shifted from 253 nm to 318 nm, showing that the MNP-CP clusters were coated instead of the particles individually. The peak at 32 nm disappeared after applying the Stöber method.

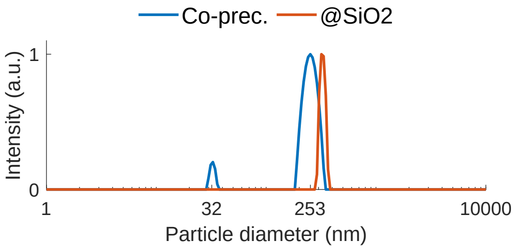

Figure 4.16: DLS curve of (a) the MNP-CPs and (b) the MNP-CP @SiO_2 using a AH/TEOS volume ratio of 1/4 mL/mL.

Thermal decomposition

The TEM image in Figure 4.17a shows the MNP-TD after the silica coating process. The nanoparticles are not dispersed. Dark spheres of around 80 nm can be detected in the aggregates, as depicted on the figure. They supposedly correspond to the MNP-TDs. It can furthermore be seen that they are covered with very small beads, assumed to be made of SiO_2. Hence, a coating made of small silica beads was probably formed around the magnetic cores instead of a homogeneous shell.

The DLS curves in Figure 4.17b show the size distribution of MNP-TDs before (upper blue curve) and after (4 lower curves) the silica coating. The MNP-TD @SiO_2 were dispersed in four different solvents with different pH. A single peak shifted to larger sizes beyond 100 nm is observed for each solvent. Dispersion in EtOH leads to smaller aggregates

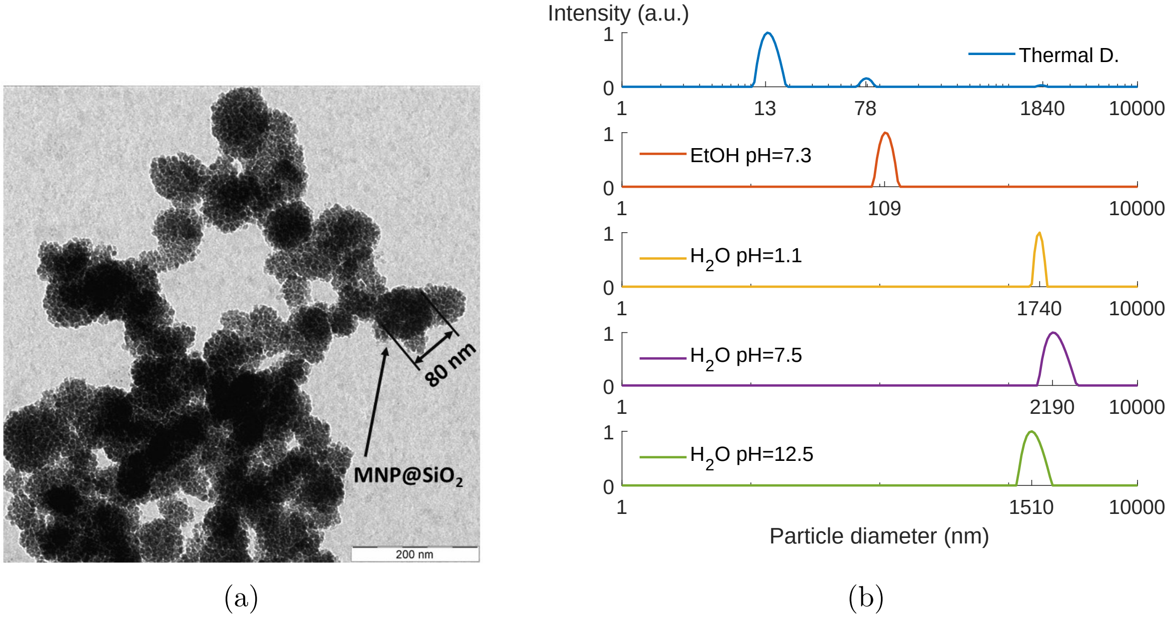

Figure 4.17: (a) TEM micrograph of MNP-TD @SiO$_2$ and (b) DLS curve of the MNPs before and after silica coating in different solvents with different pH.

by one order of magnitude than in water. Although the different pH of water all induce large aggregates, basic pH leads to the smallest ones.

Commercial MNPs

The silica coating applied to the commercial MNPs cannot be seen on the TEM micrograph in Figure 4.18a. Only black nanoparticles are observed, without any silica layers or puddles. The DLS curve in Figure 4.18b shows that the peaks before and after the silica coating are both located around 110 nm. The particle size was not influenced by the Stöber process.

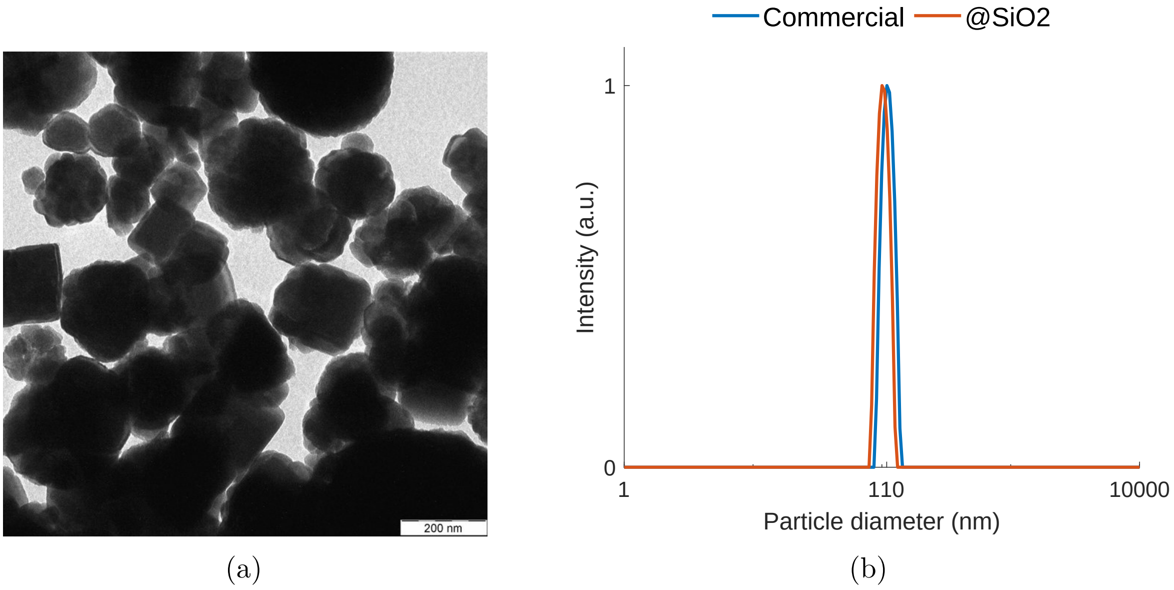

Figure 4.18: (a) TEM micrograph of commercial MNPs after silica coating and (b) DLS curve of the MNPs before and after silica coating.

1.2.3 MNP @Mesoporous SiO_2

The MNPs presented before are now coated with mesoporous silica (SiO2), again to offer functional groups for further binding with bioreceptors.

Co-precipitation

A mesoporous silica layer around the MNP-CPs cannot be seen in Figure 4.19a. Instead, a dark aggregate of several μm is observed. The spherical shapes of the nanoparticles at the edge of the aggregate can be distinguished.

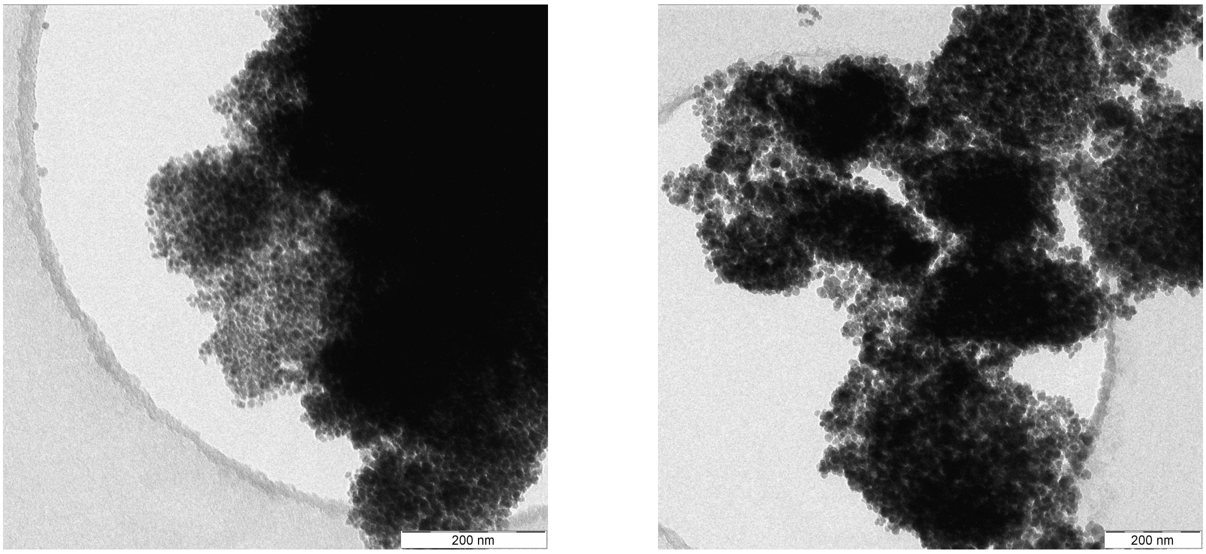

(a) (b)

Figure 4.19: TEM micrographs of mesoporous silica coatings on (a) MNP-CPs and (b) MNP-TDs.

Thermal decomposition

As shown by TEM in Figure 4.19b, no mesoporous silica is observed around the MNP-TDs. Instead, particles form aggregates of hundreds of nanometers with elongated shapes. The nanoparticles can be individually distinguished at the edge of the aggregates

Commercial MNPs

Figure 4.20b and b respectively reveal low and high magnifications of TEM images of the commercial MNP coated with mesoporous SiO_2. The micrographs indicate clearly the presence of mesoporous silica uniformly deposited onto the magnetic cores. Figure 4.20a shows that almost all the particles were covered, more or less individually. Concentrations of mesoporous silica trapped between MNPs are observed in the upper left corner of the same image. A higher magnification in Figure 4.20b reveals the mesoporous structure of the silica coating. The coating is ∼15 nm thick. Moreover, the coating seems to follow the shape of the particles well.

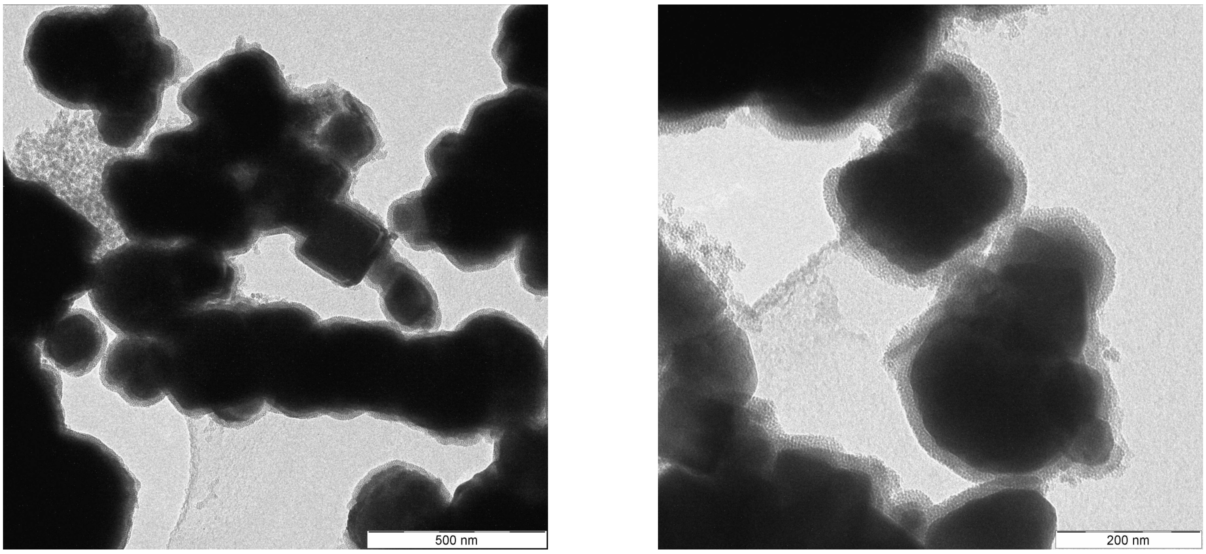

(a) (b)

Figure 4.20: TEM micrographs of mesoporous coated commercial MNPs at (a) low and (b) high magnification.

1.3 MNP @AuNP

In addition to silica, another way to provide functional surface groups for further bio-conjugation of the MNPs is to coat them with AuNPs, whose bio-functionalization is more straightforward. Given their large size of ∼110 nm, only the commercial magnetic nanoparticles were considered. In this way, the AuNPs can form a complete shell around the magnetic cores.

1.3.1 MNP @Commercial AuNPs

Commercial AuNPs provided by Unisensor® were attached to the MNPs as shown in the TEM images in Figures 4.21a and 4.21b. The little black spheres correspond to the AuNPs while the large dark areas correspond to the magnetic cores. The 35 nm gold seeds are present in small amounts.

1.3.2 MNP @Homemade AuNPs

The TEM micrographs shown in Figures 4.22a and 4.22b show the commercial MNPs coated with homemade AuNPs (MNP @AuNP). The surface of the cores is rough due to the deposition of the gold seeds. The whole surface of the MNPs are covered by AuNPs with equal densities.

The SEM images shown in Figures 4.23a and 4.23b also reveal the presence of gold seeds around the magnetic cores. The small white dots represent the homemade AuNPs. The contrast between both nanoparticles is strong. The magnetic cores are not fully covered with AuNPs but they have equal densities at the surface. Some nanoparticles exhibit very light edges due to the edge effect previously introduced.

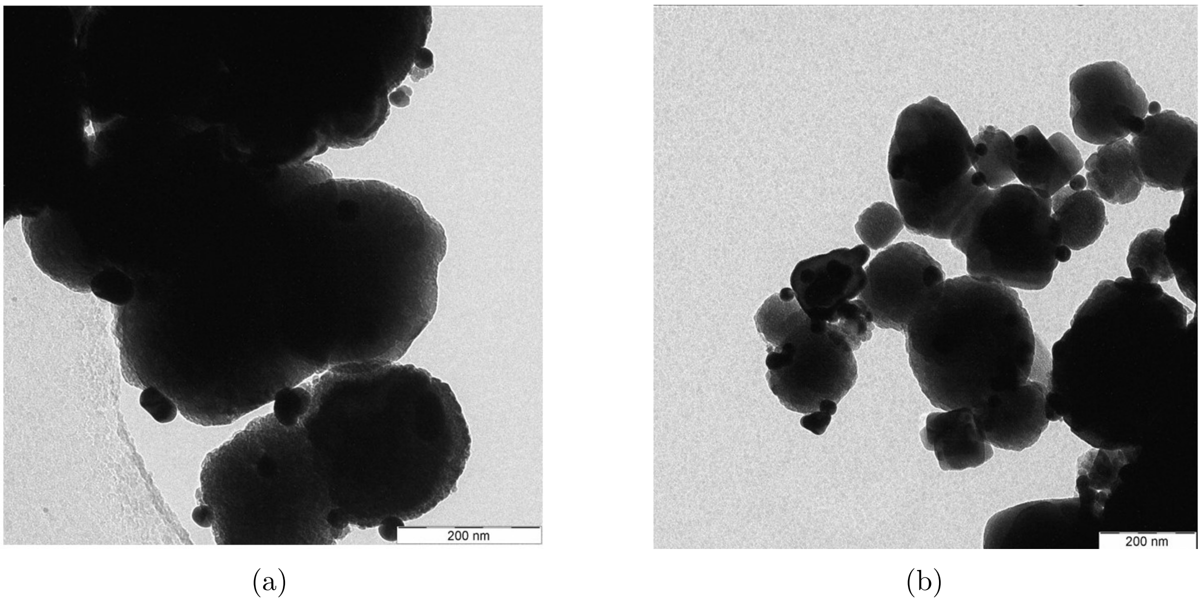

(a) (b)

Figure 4.21: TEM micrographs of the commercial MNP @Commercial AuNPs at (a) low and (b) high magnification.

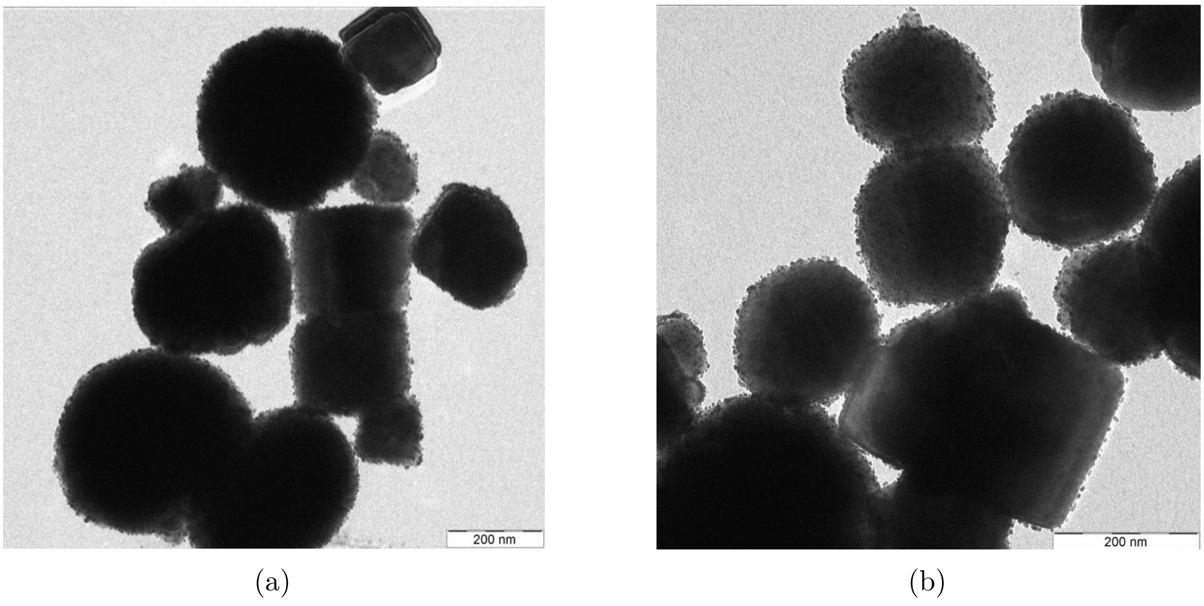

(a) (b)

Figure 4.22: TEM micrographs of the commercial MNP @Homemade AuNPs at (a) low and (b) high magnification.

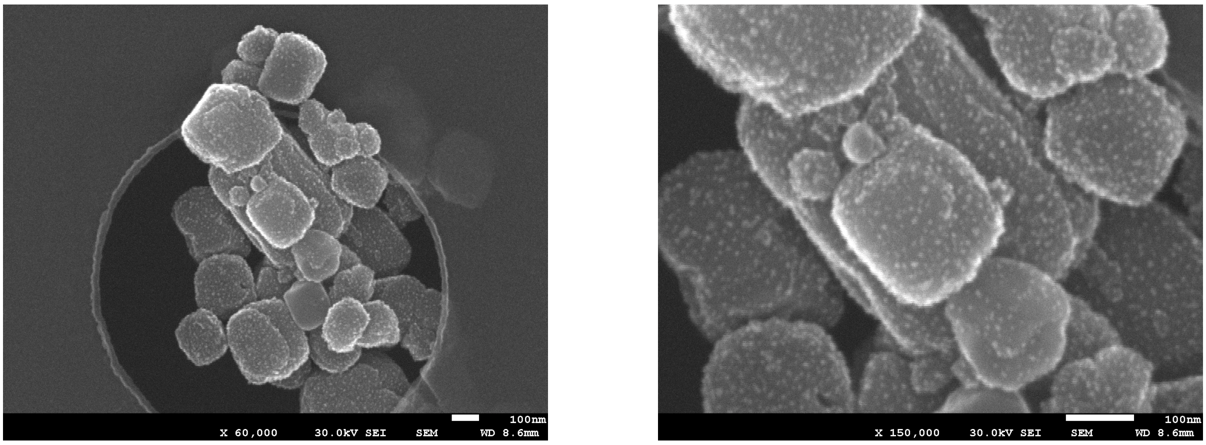

(a) (b)

Figure 4.23: SEM images of the commercial MNP @Homemade AuNPs at (a) low and (b) high magnification.

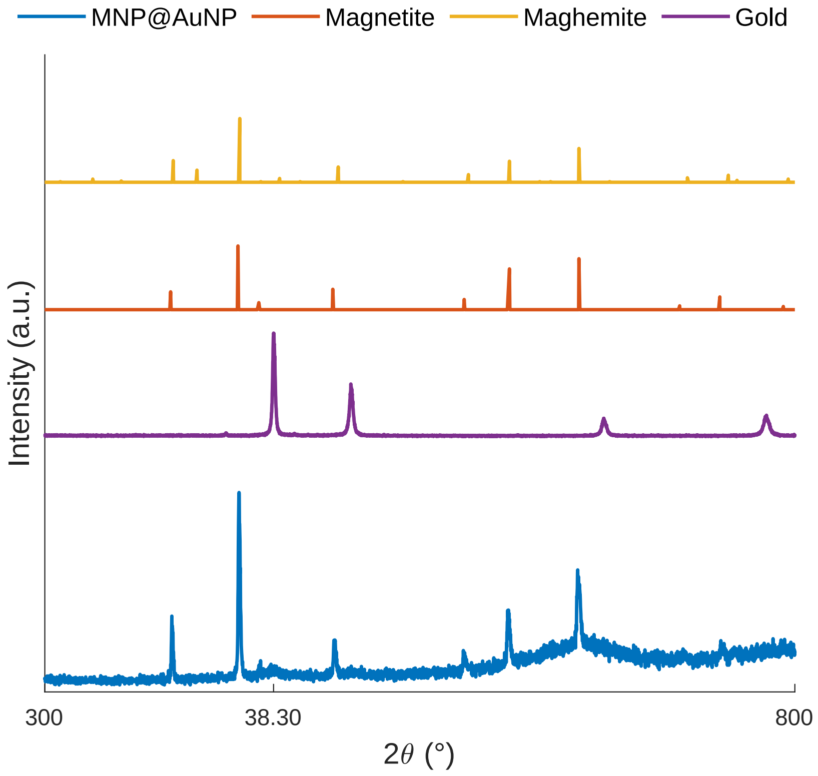

Figure 4.24: X-ray diffractogram of the commercial MNP @Homemade AuNPs.

The XRD diffractogram of the commercial MNPs @AuNPs shown in Figure 4.24 corresponds to the pattern of magnetite and maghemite. However, a small peak at 38.30° is observed and is not present in the pattern of magnetite nor maghemite. As a matter of fact, it confirms the presence of gold at the surface of the MNPs, whose reference pattern is also represented in purple[1].

Figure 4.25 shows the SEM-EDX spectrum of the MNPs @AuNPs. The iron and oxygen peaks refer to the iron-oxide magnetic core. Presence of gold at the surface is also confirmed to a lesser extent. The spectrum also reveals existence of carbon and copper at the surface. This is due to contamination from the copper TEM grid and the carbon film on which the nanoparticles were deposited.
Furthermore, Table 4.1 gives the mass and atomic percentages of the elements detected at the surface. The ratio between the atomic presence of gold and iron is equal to 1.26%, which indicates that there is about 100 times more iron at the surface than gold. Finally, the large presence of carbon and copper indicates that the TEM grid contaminated the sample significantly.

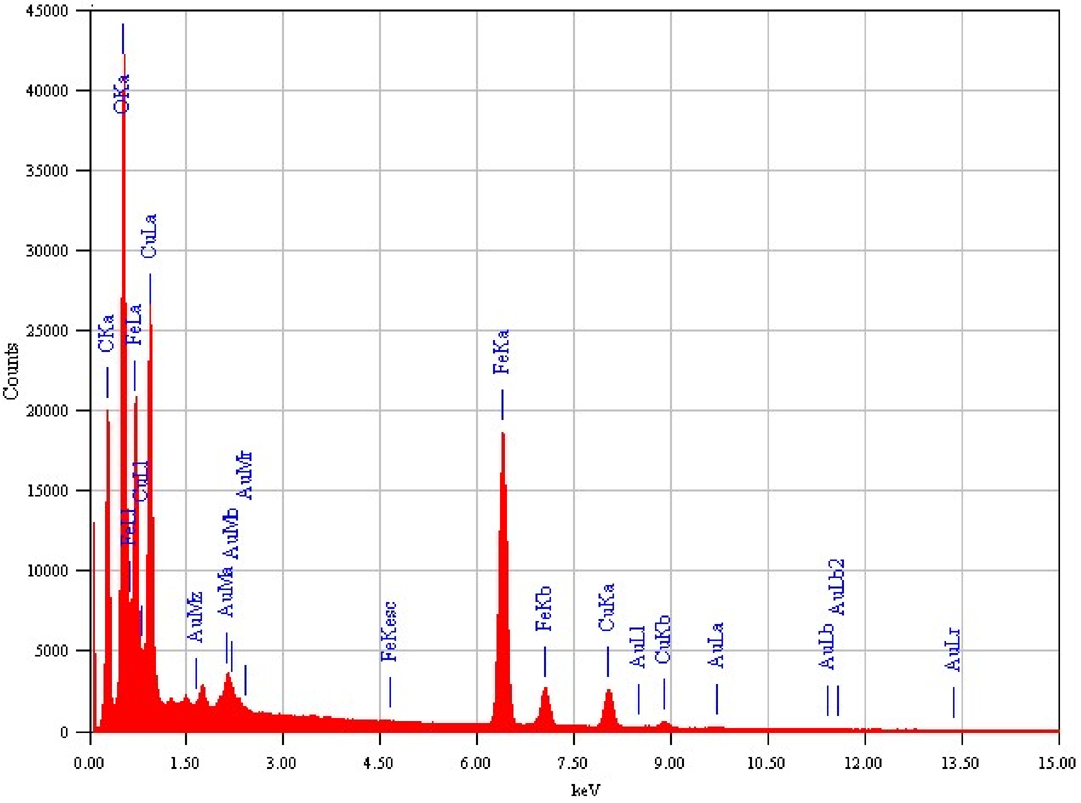

Figure 4.25: SEM-EDX spectrum of the commercial MNP @Homemade AuNPs. Each peak corresponds to the energy (keV) released by the electrons of a certain element (Au, Fe, ...) from a certain shell when migrating from a certain shell to an inner shell (Ka, Mb, ...), cfr. Figure 3.7.

---

[1] The reference pattern for gold was taken from the RRUFF Project website. `https://rruff.info/gold/display=default/`

Table 4.1: Elemental composition of the commercial MNP @Homemade AuNPs determined by SEM-EDX.

Element	Mass%	Atomic%
Carbon	26.62	47.66
Oxygen	26.07	35.04
Iron	35.00	13.48
Copper	10.80	3.65
Gold	1.51	0.17

Finally, Figure 4.26 shows the commercial MNPs after three cycles of AuNP deposition. The black magnetic cores can be observed with several small spheres attached to it, representing the homemade gold nanoparticles. The density of AuNPs at the surface is significantly reduced.

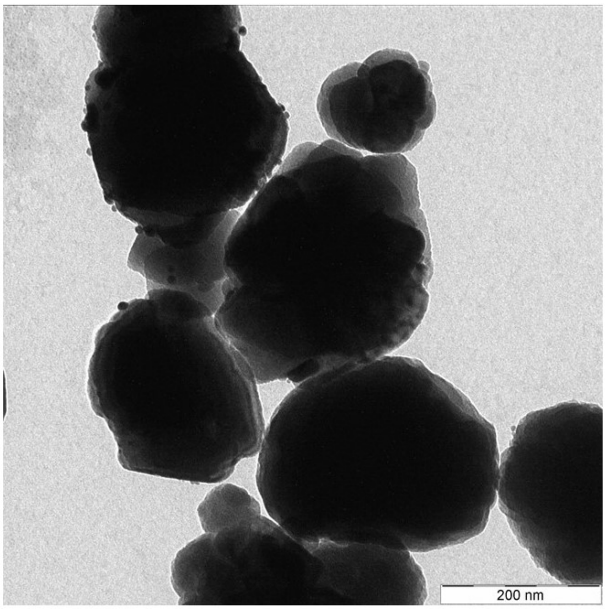

Figure 4.26: TEM micrograph of the commercial MNP @Homemade AuNPs after three cycles.

2 Microfluidics in LFAs

Let us now zoom out from the nanoscale to the microscale to study the integration of the nanoparticles in the lateral flow assays. To this end, the microstructure of the different papers is analyzed at first. Afterwards, the microfluidic properties of the LFA strips is assessed with water. Finally, the evolution of nanoparticles in solution through the LFA strip is evaluated with the naked eye.

2.1 Microstructure of papers

The microstructure of the papers (*i.e.* cellulose, glass fiber and nitrocellulose) composing the LFAs are analyzed by SEM operating at 2 keV. Low (x100) and high (x1000) magnifications are given for each material. The parameters used for the SEM are given in the black strip at the bottom of each image. LM means low magnification, GB means gentle beam.

2.1.1 Cellulose

Figure 4.27 shows the SEM images of the cellulose fiber (Surewick® C083, Merck-Millipore) typically used for sample and absorbent pads. At low magnification (Figure 4.27a), a dense fibric microstructure can be seen. Many fibers of few μm large are entangled and form the porous material. They do not have a preferential direction. At high magnification (Figure 4.27b), only few pores of 5-10 μm are observed, reflecting the high density of the cellulose.

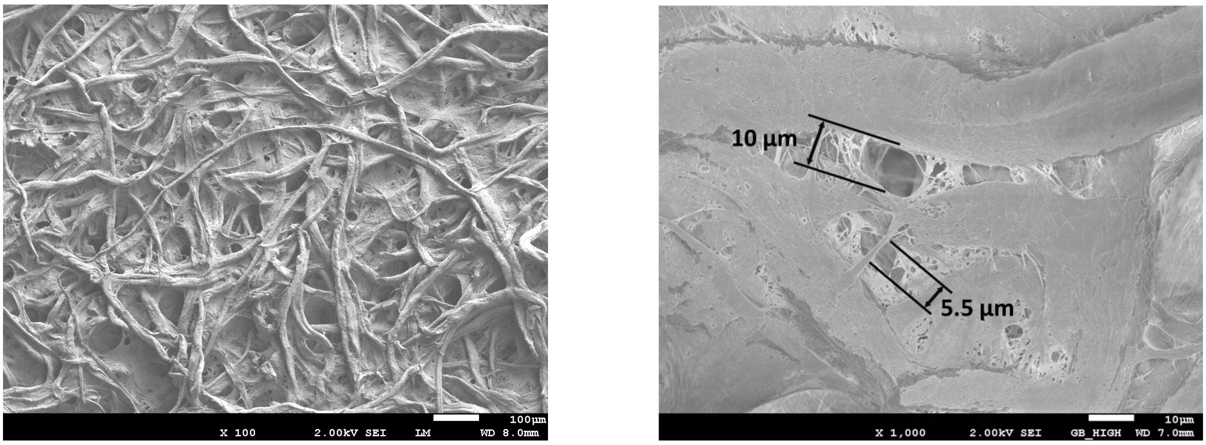

(a) (b)

Figure 4.27: SEM image of cellulose fibers (Surewick ® C083, Merck-Millipore) for sample and absorbent pads at (a) low (x100) and (b) high (x1000) magnification.

2.1.2 Glass fiber

The SEM image in Figure 4.28 reveals the microstructure of glass fiber (ReliaFlow™ 8950, Ahlstrom-Munksjö) used for conjugate pads at low and high magnification. At low magnification (Figure 4.28a), straight glass fibers randomly oriented are observed. Some groups of 4-5 fibers stuck together can also be seen. Much space between the fibers is observed. The material is very porous. At high magnification (Figure 4.28b), it is depicted that the diameter of the fiber is around 20 μm large. Moreover, the surface of the fiber looks very smooth.[1]

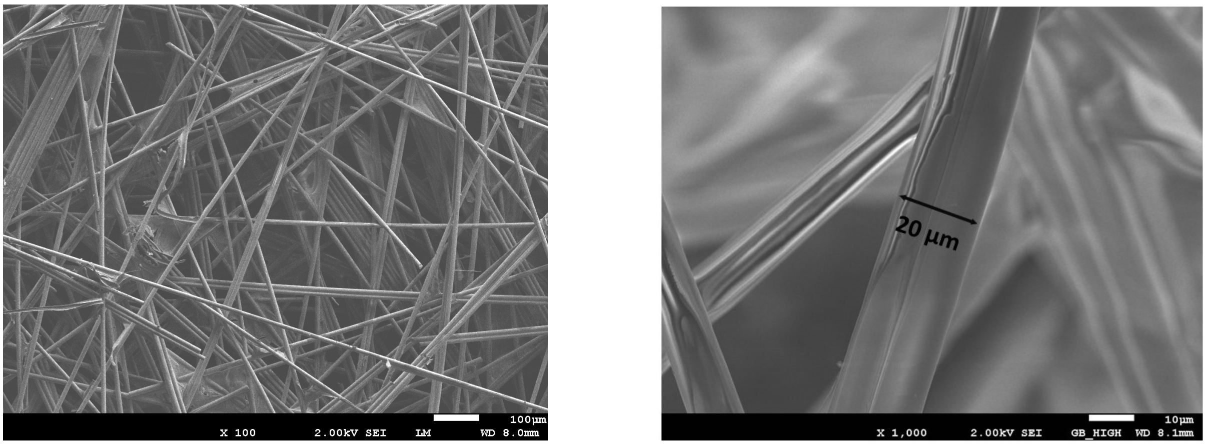

(a) (b)

Figure 4.28: SEM image of glass fiber (ReliaFlow™ 8950, Ahlstrom-Munksjö) for the conjugate pad at (a) low (x100) and (b) high (x1000) magnification.

2.1.3 Nitrocellulose

The SEM images of NC (Unisart® CN95, Sartorius) for the membrane are shown in Figure 4.29. At low magnification, a porous foam-like microstructure is observed. No distinct fibers can be seen. The white depositions at the surface probably come from external contamination (e.g. dust). At high magnification, a porous network of NC fibers is observed. The pores are several tens of micrometers wide.

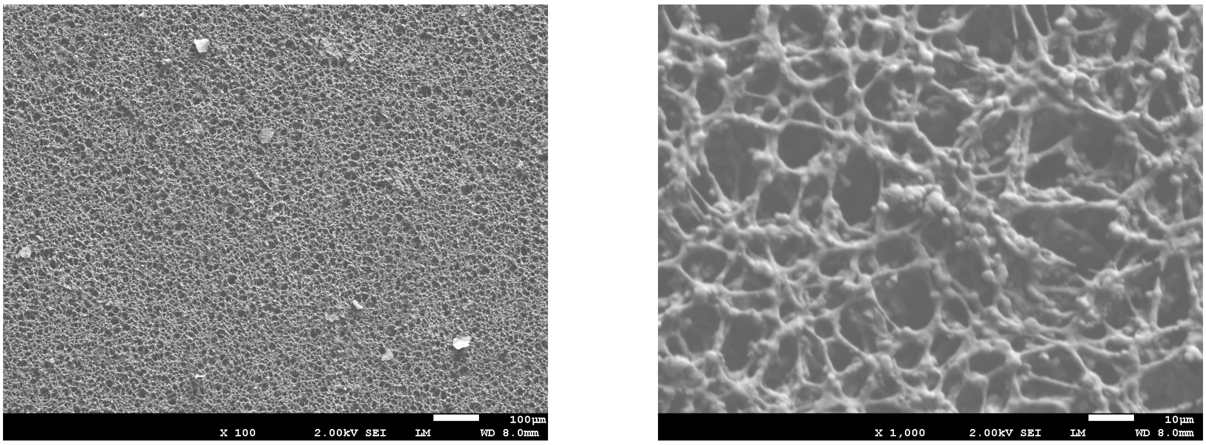

(a) (b)

Figure 4.29: SEM image of nitrocellulose (Unisart® CN95, Sartorius) for the membrane at (a) low (x100) and (b) high (x1000) magnification.

---

[1] The reason why it is called "glass fiber" makes sense as the fiber looks shiny and somehow transparent.

2.2 Capillary flow in LFAs

After characterizing the microstructure of the LFA materials, their microfluidic properties are first studied with water and then with NPs in solution.

2.2.1 Water front evolution in different assemblies

One reference test (Ref.) and three other tests were assembled such that only one material changes for each test, either for the sample pad (SP), membrane (M) or absorbent pad (AP). The four different cases are summarized in Table 3.4.
When the sample is dropped onto the SP, it flows by capillarity towards the conjugate pad, enters the membrane at 20 mm, the AP at 43 mm (2 mm overlap) and reaches the end after 60 mm.

The evolution of the water front over time in the four strips is shown in Figure 4.30a. Pictures of the respective tests are given in Figure 4.30b. In general, when flowing through the membrane, *i.e.* from 20 to 43 mm, the capillary flow rate[1] of the water front decays exponentially.
After 43 mm, the water front does not evolve for a certain time. This is due to the overlap between the absorbent pad and the membrane. Water needs to accumulate to overcome the overlap and continue its flow. When the front starts progressing again, a similar curve with a decreasing capillary speed over time is observed but with much lower slope (*i.e.* capillary flow rate).

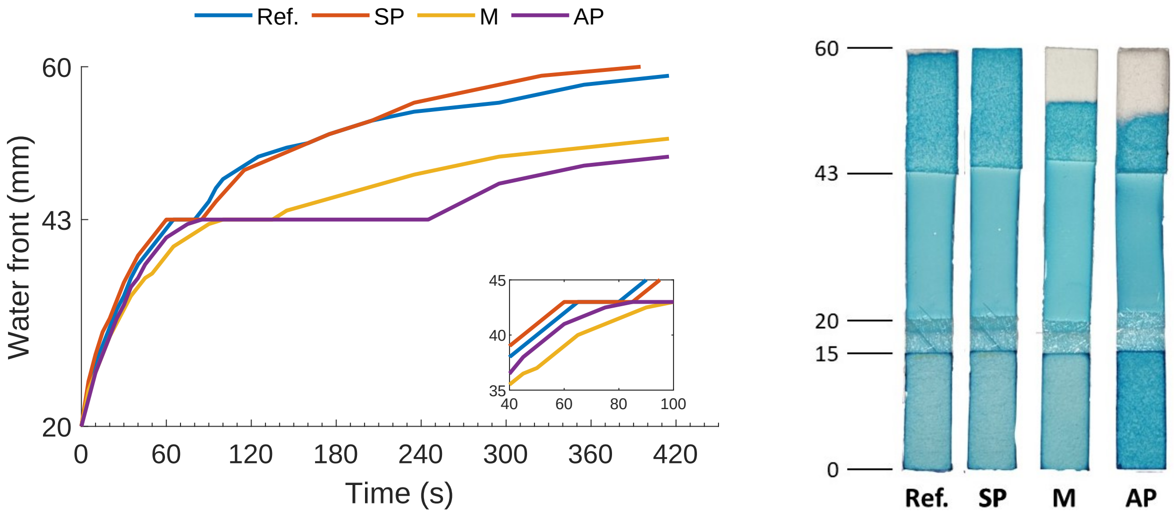

(a)

(b)

Figure 4.30: (a) Evolution of the water front over time in the four different LFA strips for which either the SP, M or AP is changed (cfr. Table 3.4) and (b) pictures of the respective strips after the test.

---

[1] The capillary flow rate is the evolution of the water front over a time interval, hence the slope of the curve here.

SP change First, when reducing the capillary flow time of the sample pad from 86 (Ref. curve) to 240 sec/4cm (SP curve)[1], there is no significant change in the water front evolution. Some deviations between the red and blue curves are due to inaccuracies during the measurement.
Furthermore, both curves end around 60 mm (58 mm for the reference curve), which means that the water front reached the end of the test. This can also be observed with the pictures in Figure 4.30b.

Membrane change Second, reducing the capillary flow time of the NC for the membrane from 95 to 155 sec/4cm has a significant effect on the evolution of the water front, as it can be seen in Figure 4.30a and especially in the lower right box. Indeed, the yellow curve takes 40 seconds more for the front to reach the end of the membrane. The time interval at the overlap between the membrane and the AP appears to be longer too (40 seconds compared to 15 for the reference curve).
Moreover, the water front stopped at 52 mm in the AP. This is also observed on the respective strip in Figure 4.30b.

AP change Finally, increasing the capillary flow rate of the absorbent pad from 86 to 50 sec/4cm only significantly affects the water front evolution at the overlap at 43 mm. Before that, differences between the purple and blue curves are assumed to come from inaccuracies during the measurements.
It takes over 2 more minutes for the water front to overcome the overlap compared to the reference strip. Moreover, the front does not reach the end of the test but stops at 50 mm in the AP, as shown in Figure 4.30b.

2.2.2 Nanoparticle flow in LFA strips

After studying the capillary flow rate inside LFA strips with water, different nanoparticle solutions are now dropped on the sample pad and their evolution is analyzed.

Figure 4.31 shows 5 LFA strips on which 300 μL of different nanoparticle solutions have been dropped. First of all, the gold nanoparticles exhibit a red color while the iron-oxide nanoparticles are black and brown.
Overall, most of the nanoparticles are trapped in the sample pad and none is visible in the absorbent pad. However, in each case, some NPs have reached the membrane, even the homemade AuNPs although it is not clear on the picture.

The commercial AuNPs are the most dispersed in the membrane, although much of them were trapped in the SP.
The commercial MNPs exhibit a black color while the MNP-CPs and MNP-TDs are brown. The MNPs all formed a clear front in the membrane. No MNP was visible beyond these fronts with naked eye.

---

[1] This might be confusing but the capillary flow time indeed decreases when it takes more time for the water front to cover 4 cm.

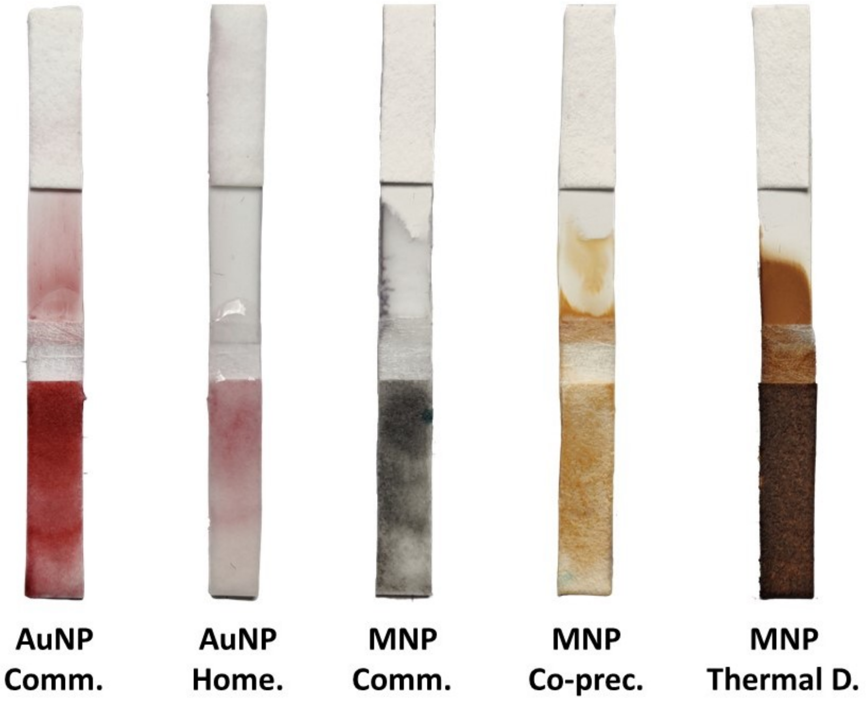

Figure 4.31: Flow of different NP solutions in LFA strips. From left to right, commercial AuNPs, homemade AuNPs (MR=2.3), commercial MNPs in EtOH, MNP-CPs in EtOH and MNP-TDs in hexane were dropped on the sample pad.

Chapter 5

Discussion

Nanoparticles are the signal transducers of LFAs: they bind to specific bioreceptors in order to translate their interactions with the target analyte into a signal. This signal can be of different types, depending on the nanoparticle, such as colorimetric, electrical or magnetic to name a few. As a matter of fact, nanoparticles are the main elements enhancing the sensitivity, stability and limit of detection of the LFA.

A three-step zoom out regarding the integration of NPs in lateral flow assays for bacteria detection in water is presented hereafter. First, the characteristics of AuNP, MNP @SiO_2 and MNP @AuNP are discussed at the nanoscale. Then, at a microscale, their integration into the fibric microstructure of different papers is analyzed. Finally, their macroscopic behavior in complete LFAs is assessed.

1 Nanoparticles for LFAs

Nanoparticles significantly improve the detection performance of LFAs. On the one hand, gold nanoparticles exhibit an intense red color and possess interesting electrical properties, providing colorimetric and electrochemical detection schemes to the LFA. On the other hand, iron-oxide magnetic nanoparticles exhibit dark colors and respond to external magnetic fields, offering colorimetric and magnetic detection to the LFA, as well as pre-concentration of the sample to increase the sensitivity.

Once synthesized, the nanoparticles need adapted functional groups at their surface for further conjugation with specific bioreceptors. By completely covering the NPs with these, the probability of attachment to the target analyte (e.g. bacteria) and thereby the sensitivity of the test is significantly increased. Moreover, since bacteria already have comparable sizes with the pores of the paper (several microns), it is important that the grafted nanoparticles do not increase their size even more. Otherwise, clogging of the pores might occur and the rate of transfer through the membrane might be disturbed, thereby falsifying the test. Hence, they should ideally form a layer of several nm thick around the bacteria and not bind as clusters of hundreds of nm. Meanwhile, the nanoparticles have to keep their respective colorimetric, electrochemical or magnetic properties.

To sum up, size, shape and dispersion of the NPs are of major concern and were characterized by different techniques discussed in section 3. As a reminder, it was mentioned that there is no perfect characterization technique for assessing the properties of nanoparticles. Their results must be compared together in order to draw thorough conclusions. This strategy is adopted in the following discussion for AuNP, MNP @SiO2 and MNP @AuNP.

1.1 AuNP: Influence of the molar ratio

From the five investigated molar ratios of citrate to gold, the one equal to 3.7 led to the most promising AuNPs for LFA applications. Dispersed nanoparticles with sizes ranging from 6 to 10 nm were obtained (Figure 4.2). This is in accordance with Shi *et al.* [159], stating that MR $>$ 3.5 lead to small ($\sim$10 nm) and monodisperse AuNPs. For MR $<$ 3.5, less citrate is available to stabilize the AuNPs which leads to bimodal size distributions[1], as observed in the same figure and confirmed by Dong *et al.* [84].

The properties (shape, dispersion) of the homemade AuNPs were comparable with the commercial ones by TEM and UV-Vis spectroscopy. Although the TEM image (Figure 4.1) shows AuNPs resulting for MR 2.3, it is assumed that the AuNPs from MR 3.7 would look very similar since the latter molar ratio was shown to lead to an even better dispersion.

Outlooks Although the AuNPs synthesized with MR 3.7 presented promising properties. They formed few 180 nm sized aggregates that might hinder their performance in the LFA. To make them vanish, higher molar ratios could be considered in further research. However, excessive MR are known to induce aggregation. The maximum MR is still a matter of debate: Shi *et al.* [159] state that 4.0 already leads to higher polydispersity and aggregation, while Zabetakis *et al.* [160] mention 17.0. In this study, it was shown that MR 5.8 led to much more polydisperse AuNPs. Hence, the molar ratio leading to perfectly dispersed AuNPs should lie between 3.7 and 5.8 and is to be further investigated, e.g. by increasing the MR by steps of 0.2.
Finally, it is reported in the literature that the sensitivity of colorimetric LFA tests could be significantly improved when the AuNP size increases from 6-10 to 20-30 nm AuNPs (like the commercial ones) because they exhibit an even more intense red color [16, 17]. The Turkevich method used in this study cannot lead to such sizes and could be modified consequently. As an example, iso-ascorbic acid was used by Andreescu *et al.* [161] instead of NaCt to form 30-40 nm citrate capped AuNPs. The impact of larger sizes on the electrochemical properties is to be confirmed.

1.2 MNP @SiO_2

Coating the MNPs with SiO_2 offers many advantages for LFA applications: it provides functional groups for further bio-conjugation with antibodies, protection against chemical oxidation or degradation of the magnetic core and it stabilizes the MNPs [116–118]. All the magnetic cores synthesized in this study were coated with a silica layer, except the MNP-H. Their very small sizes ($\leq$10 nm) would have made the SiO_2 coating very difficult.[2]

General comments The UV-Vis spectroscopy results for MNPs are presented in Appendix C but did not provide key information regarding the investigated properties.
Moreover, while the distinction between magnetite and maghemite is not always clear on the X-ray diffractograms, both phases are known to exhibit good magnetic properties.

---

[1] The growth mechanism of AuNPs indeed depends on the initial quantity of NaCt used. As a matter of fact, when adding the reducer as last step of the Turkevich method, large numbers of golden seed particles ($\sim$4 nm) are formed. If there is sufficient citrate, the seed particles are stabilized and the AuNPs grow. If there is not enough citrate, they aggregate and result in larger and less spherical AuNPs [84].

[2] As a matter of fact, the study was inspired from revealed the formation of clusters of 210 nm made of many magnetic seeds with average sizes of 6 nm [141]. Although such clusters could not be seen here, the mentioned NP size corresponds to what is observed by TEM (Figure 4.11a). The latter technique is more reliable than DLS which shows a broad peak around 375 nm.

Hence, the exact phase composition of the MNPs is not very important at this stage for LFA applications and it will thus not be discussed further. However, the XRD characterization was still useful to confirm that iron-oxide nanoparticles were each time synthesized and to determine the size of the nanoparticles.

MNP-TD: Formation of silica beads

Before applying the silica coating, the MNPs synthesized by thermal decomposition exhibited a narrow size distribution without aggregating much (Figure 4.9a). As a matter of fact, the dispersion of the MNP-TDs is due to the oleylamine used during the synthesis. They act as ligands (cfr. section 2.4) around the NPs and prevent interactions between neighbouring particles.
Similar TEM and XRD characterizations of MNP-TDs were shown by Xu *et al.* [140] and Mourdikoudis *et al.* [162], except that they obtained exclusively spherical particles while different geometries were obtained here. The variety of shapes might hinder the bio-conjugation and the consistent flux of NPs through the membrane, subsequently reducing the sensitivity of the LFA test [17]. One cause could be the lower temperature maintained at 270 °C instead of 300 °C. As a reminder, this choice was deliberate to avoid any risk of explosion.

Silica coating The coating of the MNP-TDs with SiO_2 significantly destabilized the particles, leading to aggregates of 100 to 2000 nm (Figure 4.17). There are two reasons for this. On the one hand, the oleylamine ligands cannot prevent aggregation anymore because of the silica. On the other hand, the change of polarity of the solvent from hexane (non-polar) to EtOH or H_2O (polar) might also take responsibility for the loss of the dispersion (Figure 4.17b). Since this solvent change was done before the silica coating and imposed by the Stöber method, the NPs might already have been aggregated when the coating starts. This could have in turn affected the uniformity of the coating. In addition, the magnetic stirring might also have hindered the dispersion of MNPs during the procedure.
Moreover, while a homogeneous shell of silica was expected as shown by Zhang *et al.* [163], the MNP-TDs were in reality covered by small beads (Figure 4.17a), supposedly made out of SiO_2. One reason could be the presence of oleylamine hindering a homogeneous polymerization of SiO_2 around the core.

Outlooks Instead of coating the MNP-TDs with SiO_2 which seems problematic, one solution could be to take advantage of the oleylamine ligands by exchanging them with groups having phosphonate groups at one end (with a large affinity to iron-oxide) and the specific antigen at the other end [164, 165]. Although very interesting, this might not be adapted to water quality assessments with LFAs since it is more complicated than silica coating and the magnetic core would be less protected from chemical oxidation due to water molecules.

MNP-CP: Influence of AH to TEOS ratio

Although very easy to apply, direct co-precipitation led to > 200 nm sized aggregates (Figure 4.6). As a matter of fact, in contrast to MNP-TDs covered with oleylamine ligands, the MNP-CPs surfaces are hydrophobic and thus aggregate significantly in solution [118]. To overcome this, different dispersion method were performed to separate and stabilize the MNP-CPs. However, neither longer ultrasonication, nor adding surfactants like CTAB or PVP improved the dispersion of the particles.

In addition, the MNP-CPs resulted in a small peak at 33 nm on the DLS curve whereas XRD gave an average size of 14.2 nm. It is difficult to determine which technique gives the correct size. Either the DLS measured the hydrodynamic radius of 2 nanoparticles at a time, or they are made of 2 crystallites of 14.2 nm.

In general, XRD provides more precise information regarding the size of crystalline nanoparticles, since DLS does not make a difference between single nanoparticles and aggregates in solution. However, it cannot be ensured that the nanoparticles are each made of one single crystallite. Since TEM showed that the MNP-CPs at the edge of the clusters had similar sizes to the XRD value, 14.2 nm is considered to be the best estimation of the MNP-CP size.

Silica coating From the nine investigated volume ratios of AH to TEOS (Figure 4.15), only one (0.25/1.00 mL/mL) led to the expected spherical and dispersed core-shell structures. This result can be used in further research if the same amounts of the same MNP-CPs are considered. Otherwise, the ideal ratio of AH to TEOS is to be similarly established by trial and error. The core-shell structure depicted in Figure 4.15c has a magnetic core of 32 nm and a silica shell thickness of ∼4 nm.[1] Similar structures were observed by Faaliyan *et al.* [166] (MNP 20 nm, SiO_2 2.5 nm).

Outlooks The advantage of the Stöber method is that the shell thickness can theoretically be tuned from 2.5 to 200 nm by playing with the initial TEOS concentration [118, 167–169]. However, as it was shown in this study, changing this parameter might not always lead to the expected core-shell structures but rather to puddles of silica or incomplete coatings. Furthermore, although thick shells stabilize and protect the cores from oxidation, they also decrease their magnetic properties. As an example, a decrease of 40% in the saturation magnetization was observed for MNPs of 20 nm with a silica shell of 5 nm [170]. Hence, there is an optimal shell thickness stabilizing and protecting the core sufficiently while not decreasing the magnetic properties too much.

Commercial MNP: No visible SiO_2

The commercial magnetic cores were found by DLS to have sizes around 110 nm and by XRD to be made out of two iron-oxide crystallites of 67.2 nm on average.

No silica could be seen by TEM after applying the Stöber method to the commercial MNPs, probably because the quantities of chemicals used were not adapted to the ∼10 times larger cores than the MNP-CPs and MNP-TDs. The contrast between the non-mesoporous silica and the MNP could not be seen. The presence or absence of SiO_2 cannot be concluded and could be further determined by X-ray photoelectron spectroscopy (XPS) for example.

General perspectives regarding the Stöber method for MNPs @SiO_2

To sum up, MNP-CPs were successfully coated and stabilized with a thin silica layer of ∼4 nm. The next step consists of an additional coating with carboxylic acids for further bio-conjugation [171]. The carboxyls can be characterized by Fourier-transform infrared spectroscopy (FTIR) and the bioreceptors by DLS or UV-Vis to name a few [61, 172]. However, it was shown that the Stöber method was challenging for coating MNPs with uniform SiO_2 layers and well dispersed [117]. Other methods like inverse micro-emulsion exist but are more complicated [124, 173].

---

[1] A large MNP core was depicted here, which is why the size of 32 nm does not fit with the average size of 14.2 nm determined by XRD.

In addition, the aggregation of the MNPs might simply come from their intrinsic magnetic properties, independently of the Stöber method. Indeed, they may not be perfectly superparamagnetic. Because a strong magnet was used to verify their magnetic response and because of the magnetic stirring, the MNPs may possess a very low remanent magnetization but large enough to attract the neighbours and form aggregates. To verify this, the hysteresis loop of the magnetic cores should be characterized in further research. Superconducting quantum interference device (SQUID) is the most promising technique but is difficult to access and requires much efforts [61, 117, 139]. Vibrating-sample magnetometry (VSM) [61, 174] and Ferromagnetic resonance (FMR) [175] could be used instead. If this is confirmed, non-magnetic stirring methods like vortex mixers could be further used since the MNPs are significantly attracted by the magnetic bar when stirring.

1.3 MNP @Mesoporous SiO_2

The commercial MNPs were successfully coated with a mesoporous silica shell (Figure 4.20) while the procedure did not work for MNP-CP and MNP-TD, probably because of their reduced size.

The mesoporous SiO_2 layer around the commercial MNPs was ∼15 nm thick. The TEM images are comparable with other inorganic materials, like silver nanoparticles [176] and palladium nanoparticles supported on carbon black [69]. The average pore size was not characterized but should be around 2 nm as given by Haynes *et al.* [69] since the same protocol was used in this study.

General perspectives regarding mesoporous SiO_2

Although localized concentrations of mesoporous silica were observed by TEM, the commercial MNPs were overall successfully coated with mesoporous SiO_2. They can further be coated with carboxyls and subsequently with bioreceptors.

This opens new potential opportunities for LFA applications. First, it makes the use of ∼100 nm sized nanoparticles in LFAs possible, whereas the Stöber method appeared no to enable this. This is advantageous since the strength of the magnetic response increases with the NP size, enhancing further magnetic quantification as well as faster immuno-separation.

Second, the mesoporous structure increases the surface area of the nanoparticle, thereby potentially increasing the amount of antibodies attached at the surface which could in turn increase the sensitivity of the test.

Nevertheless, these promising opportunities are to be confirmed by further research. The mesoporous structure could on the other hand negatively affect the sensitivity of the test, since proteins might be trapped in the pores, therefore becoming unable to catch the target bacteria. The core might also not be completely protected from chemical oxidation given the mesoporous structure of its shell. To remedy this, blocking the mesoporous structure could also be further investigated.

1.4 MNP @AuNP

So far, two types of nanoparticles have been discussed in depth. On the one hand, AuNPs offer colorimetric and electrochemical detection schemes to LFAs. They have sizes ranging from 5 to 30 nm and can be conjugated to bioreceptors as such. On the other hand, MNPs offer colorimetric and magnetic detection schemes as well as the possibility to pre-concentrate the target analyte before the assay. They have sizes from several nanometers to hundreds of nanometers and require additional coatings for conjugation to bioreceptors. Knowing this, the following question arises: why not combine both types of nanoparticles to take advantage of all their properties at the same time?

Given the order of magnitude separating the size of the gold and magnetic nanoparticles, a MNP-AuNP core-shell structure can be imagined and would bring many advantages. Since the AuNPs are simply deposited on the MNP surface, their sizes and thus their plasmon band resonances should not be significantly affected. Therefore, the MNP-AuNP structures would adopt the intense red color of the shell for colorimetric detection. If not, the dark color of the magnetic core can still be detected with the naked eye.
Moreover, since the AuNPs are at the surface, their electrical properties can still be used for electrochemical quantification. Finally, the magnetic properties of the core would still be available either for magnetic detection (e.g. with GMR or MPQ) and for pre-concentration of the sample, provided that the AuNP shell does not decrease the magnetic properties too much. Regarding the bio-conjugation of these core-shell structures, they would not differ much from the usual and relatively straightforward procedure for AuNPs.

First promising results

In this study, AuNPs were successfully deposited on MNPs. In particular, when comparing the SEM images before (Figure 4.13) and after (Figure 4.23) gold deposition, the home-made AuNPs formed a clear homogeneous coating on the commercial MNPs, better than with the commercial AuNPs. The size contrast between the two particles led to a very thin layer of gold which did not increase the size of the MNPs significantly.

However, the ratio of gold on the iron-oxide surface was only equal to 1.26%. This should be significantly increased in order to benefit from the colorimetric and electrical properties of the AuNPs. To this end, three cycles of AuNP deposition were performed but only few AuNPs remained in the end. This was probably due to the washing steps between the cycles removing the AuNPs and deteriorating the APTES coating. Instead, only one cycle could be performed but with much more concentrated solutions of AuNPs, as it was done in [177].

In addition, the SEM images are very similar with the ones from Hwang *et al.* [126] shown in Figure 1.19, where 160 nm sized MNPs were coated with 8 nm sized AuNPs. As a comparison, Salgueriño *et al.* [177] obtained 170 nm sized MNP @SiO_2 subsequently coated with 15 nm AuNPs for biomedical applications. Some of their results are shown in Appendix C. In a nuthsell, theyr confirmed the superparamagnetic behavior of the MNP @AuNP structures as well as their optical properties with a shift of the UV-Vis peak from 520 to 540 nm. These results are very promising for further electrical and magnetic quantification with LFAs and should be confirmed in further study.

Perspectives regarding MNP @AuNP

To summarize, Figure 5.1 schematically resumes how such core-shell MNP-AuNP structures could be integrated to LFAs. After the immuno-separation step by means of a magnet, the concentrated sample is dropped onto the sample pad (SP). As the labels are already contained in the sample, no conjugate pad is needed. Once the front has reached the end of the absorbent pad (AP), three different measurements can be done.
First of all, the sample flows through the detection area (DA). Detection antibodies are pre-immobilized at this area, similarly to the test and control lines. This is where the magnetic or electrochemical signal can be measured and quantified. As shown in Figure 1.21, the strip can be easily placed in the different magnetic readers. For the electrochemical detection, this is where the electrodes will measure the signal.
Beyond the DA, the test and control lines, TL and CL respectively, work in the same way as in colorimetric tests. They are required to give a first idea to the user whether the test has worked correctly and whether the sample contains the target analyte or not.

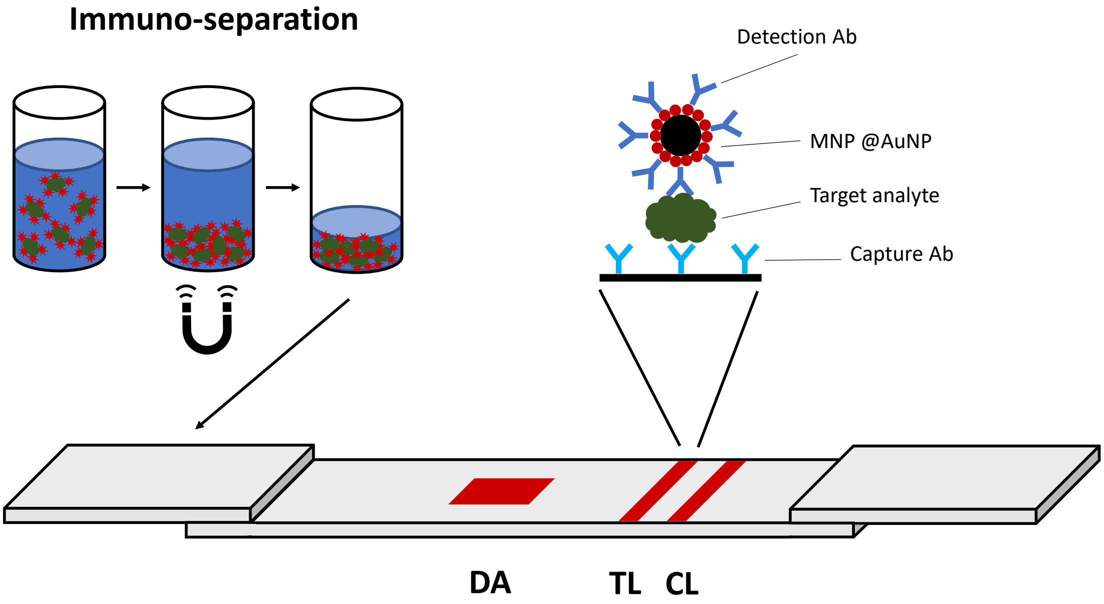

Figure 5.1: MNP-AuNP core-shell structure for lateral flow assays with pre-concentration step.

To sum up, MNP @AuNP core-shell structures integrated to LFAs as shown in Figure 5.1 respond to the main goals of this project, which is to develop paper-based biosensors for quantitative bacteria detection in water samples. Such hybrid nanoparticles have the potential to bring a simple, affordable and precise detection of bacteria in remote area water samples. They offer the opportunity to quantify the target analyte in water samples thanks to their colorimetric, electrical and magnetic properties. This would in turn make it possible in order to comply to the levels of contamination depending on the local legislations or on the type of analyte.
In this case, further research would consist of three parallel paths: (i) an increase of the gold density on the magnetic nanoparticles, (ii) the bio-conjugation of the core-shell structures and (iii) the characterization/quantification of their colorimetric, electrical and magnetic properties.

1.5 General perspectives of NPs for biosensors

Now that different NPs have been successfully synthesized and made ready for further bio-conjugation, future work consists of characterizing and quantifying their colorimetric, electrical or magnetic properties, in parallel to their bio-conjugation and improvement of the syntheses. In this regard, perspectives are drawn hereafter for each detection method.

- First, both gold and magnetic nanoparticles enable colorimetric detection. Their red, brown and black colors were observed with the naked eye. UV-Vis spectroscopy was also used to analyze the optical properties of AuNPs. This was also done for MNPs (Figure C.1) but did not provide much information. It was said that the latter technique, when calibrated, could be used for quantification of AuNPs. However, such curves might be difficult to obtain for PoC devices since it requires NPs in solution and not concentrated in papers.

- Second, MNPs enable magnetic quantification and pre-concentration of the analyte in the sample under an applied magnetic field. The magnetic properties were qualitatively confirmed in this study, both by approaching a strong magnet and by Magnetic Force Microscopy (Figure C.2). The following steps are to quantify these properties, especially the remanent and saturation magnetization of the MNPs. To this end, SQUID, Vibrating-sample magnetometry (VSM) and Ferromagnetic resonance (FMR) were mentioned to be the best options. In addition, the miniaturization of the magnetic readers introduced in section 2.4.9 might also be a limiting factor in the future.

- Third, in addition to AuNPs, the electrical properties of MNPs could also be investigated for electrical and electrochemical detection. In this way, MNPs could potentially provide three different detection methods. Towards the development of impedimetric sensors, Hotta *et al.* [178] found that the real part of the permittivity of 50-180 nm magnetite nanoparticles varied between 5 and 7 from 0.915 to 10 GHz at room temperature. In addition, MacKay et al. [179] demonstrated that nanoparticles at the surface of an electrode can interact with the double layer of this electrode in a measurable way.

- Fourth, in the spirit of developing low-impact biosensor, it would be very beneficial to interpret the optical and electrical signal with a smartphone. Semi-quantitative and even quantitative results were obtained based on the colorimetric properties of AuNPs by using the camera of smartphones as LFA reader [17, 180]. This looks more difficult for electrical and magnetic detection given the limited tools available in smartphones.

2 Microfluidics in LFAs

After discussing the nanoparticle properties in depth, their behavior in the different papers used for LFAs is further investigated. First, the microstructure of the papers analyzed by SEM are discussed. Then, the influence of the pads on the microfluidics of the test is assessed. Finally, the behavior of NPs in complete LFAs is analyzed.

2.1 Impact of pore size on analyte flow

In general, the three materials observed by SEM reveal a fiber microstructure with pore sizes in the micrometer range (Figure 4.27-4.29). The largest pores were found in glass fiber (< 100 μm), followed by nitrocellulose ($\sim$10-30 μm) and cellulose ($< 10\mu$m). Although very large compared to nanoparticles (8-200 nm in this study), pores of only few microns can cause two main problems: (i) some nanoparticles might electrostatically bind to the fibers, agglomerate and therefore clog the small pores, (ii) the target analyte (e.g. bacteria of 1-5 μm) might be larger than the pores and thus not flow through the strip, thereby falsifying the test outcome. As an example, Bergua *et al.* [181] have shown that the choice of NC for the membrane has a significant effect on the flow of big analytes ($\sim$2 μm) through the test.

2.2 Impact of pad materials on capillary flow rate

For all four assemblies in Figure 4.30, an exponential decay of the capillary flow rate can be seen in the membrane (20-43 mm) and absorbent pad (43-60 mm). This is similar to what found by O. Crahay [144] in NC samples and can be explained by the fact that the capillary force due to the difference of pressure between the liquid and the void in the pores decreases as the water front increases.

The capillary flow speed in the NC membrane is a key parameter for the sensitivity of the LFA test and determines the placement of the test and control lines. If the flow is too fast, the antibodies at the TL and CL will not have time to bind with the target analyte, which decreases the sensitivity of the assay. One solution is to decrease the pore size of the NC. Indeed, Figure 4.30 shows that this significantly decreases the capillary speed in the membrane, especially during the 25 last millimeters. However, lower pore size might hinder the flow of large analyte such as bacteria, as it will be discussed later on.

Changing the material for the absorbent pad affects the time interval during which the liquid front no longer advances between the membrane and the AP. To remedy this, the overlap between the membrane and the AP can be increased from 2 mm (as it was done in this study) to over 10 mm. Such large overlaps were observed on commercial SARS-CoV-2 and on tests provided by Unisensor®.

2.3 Nanoparticle behavior in LFAs

The SEM images and the macroscopic pictures of the tests (Figure 4.31) reveal similar outcomes. For each NP investigated, it appears that many nanoparticles are stuck in the sample pad, which is made of cellulose containing small pores of 2-5 nm.

On the one hand, this is due to the formation of non-specific bonds between the NPs and the fibers. In reality, detergents and blocking agents are added to the SP such that the nanoparticles only bind to the TL and CL and nowhere else in the test [17, 28]. This was not done in this study and represents the next step in the development of the water quality tests. As an example, Parolo *et al.* [17] mentioned the use of Tween 20 as detergent and BSA, milk or casein as blocking agent in the sample pad.

On the other hand, even with blocking agents, the SEM images of the SP (Figure 4.27) reveal a dense structure with only few pores of several microns visible. This might be problematic for the flow of bacteria. Hence, as the sample pad porosity was shown not to influence the capillary flow rate of the test (Figure 4.30), the porosity of the SP should be increased to enhance the test sensitivity. Materials like cotton or glass fiber for the SP have been reported in the literature for bacteria detection and could be further investigated [57,181,182].

A similar discussion applies to the nitrocellulose for the membrane. Indeed, less and less NPs are visible with the naked eye as the front advances in the membrane, which suggests that more and more NPs bind to the NC fibers. This again shows the importance of blocking agents. However, Parolo *et al.* [17] mention that the blocking of the membrane is generally not required when the reagents in the SP are sufficient, which facilitates the LFA fabrication.
Moreover, in order to enhance the flow of bacteria through the membrane, a highly porous NC should be chosen in further research. Even though this would increase the capillary flow rate significantly, there are ways to slow it down, with small wax pillars in the membrane for example as it was shown in Figure 1.5b [29].

Chapter 6

Environmental impact assessment

1 Introduction to responsible design

In recent decades, nanotechnology has brought fascinating enhancements for many engineering applications including electronics, consumer products, alternative energy, medicinal uses and water quality assessment. In particular, lateral flow assays are gaining more and more attention in biosensing fields, both in the literature as on the market. They are sold everywhere in the world as pregnancy tests since 1971 and, more recently, as autotests for SARS-CoV-2. The fact that they are the only autotests available to anyone in the current pandemic illustrates the power of lateral flow assays [127, 183].

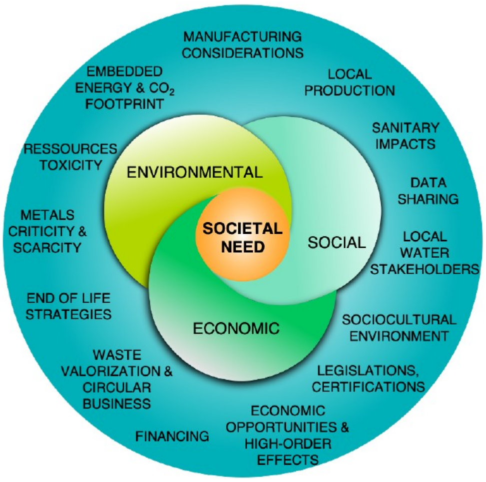

Figure 6.1: Emergence of research questions for the multidimensional analysis of affordable water quality sensors [184].

Despite the very promising properties of lateral flow assays, information regarding their environmental impacts (e.g. extraction of raw materials, energy-consuming processes, carbon footprint) and health risks (e.g. toxicity) is severely lacking. Since LFAs are for single use, they produce significant amounts of waste. As an illustration, pregnancy tests generate over 1000 tons of non-recyclable waste every year, only in the U.S. [185].

Moreover, there is an increasing concern that exposure to the nanoparticles contained in LFAs may lead to severe adverse health effects on the human body, environmental contamination and associated effects on ecosystems. Indeed, after disposing the LFA strip in landfills, the nanoparticles often end in water sources or soils. Given their nanometric size, they might finally end in our body through water or food ingestion [183, 186].

Along with environmental impact assessments, there are many other critical questions emerging for the development of low-impact biosensors for bacteria detection water samples, as given in Figure 6.1. There is a critical need to integrate holistic impact assessments (performances, environment, socio-economic) at the technology design level to anticipate new technology-related consequences hidden at first sight, and to make deliberate and informed choices with these consequences in mind [144, 184].

2 Goals, Scope and Cases definition

The goal of this study is to assess the environmental impact of the different parts of a LFA (pads and nanoparticles) and propose end-of-life (EoL) strategies. To this end, three different cases are compared based on different criteria. The first case corresponds to a standard[1] LFA without any pre-stored nanoparticles. The second case is the same but this time with the pre-stored nanoparticles. The third case is a 100% biodegradable LFA test.

The function is the same for each case: to detect the presence of bacteria in remote area water sources with the lowest environmental impact possible. The considered geometry for each test of each case corresponds to the one shown in Figure 3.1 which was used in the experimental section.
The considered functional unit is the manufacturing of 1 million of each of these tests. Most of the generic data is taken from Granta EduPack 2021 (level 3[2]), an academical software providing materials and process information among other tools.

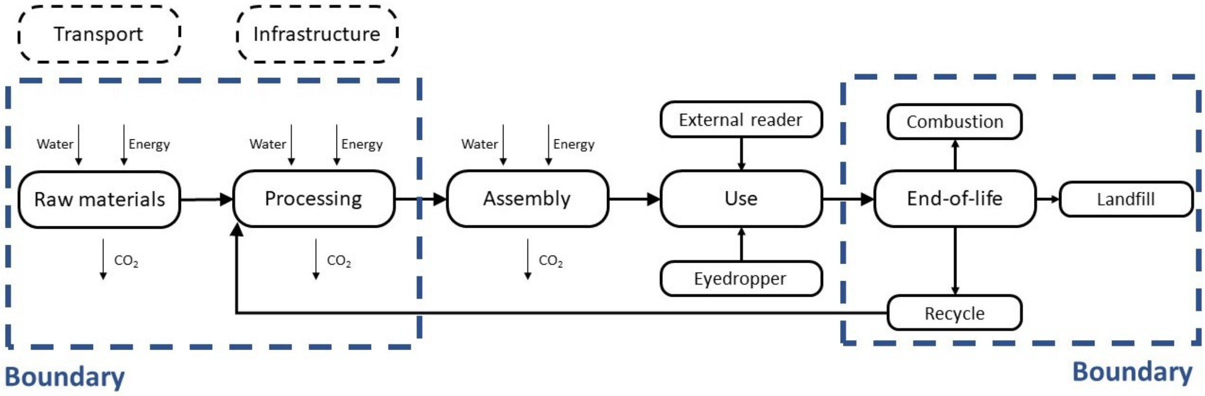

Figure 6.2: Boundaries of the study for each case.

The boundaries of this study are represented in Figure 6.2. The environmental impact of the raw materials production, primary processing and end-of-life are discussed. Since the goal is to compare the environmental impact of the different components of an LFA, transport of materials, infrastructures, assemblies and use phases are not considered. It is assumed that these steps have a similar environmental impact for the three cases[3].
The use phase is not considered either for the similar reasons. Indeed, in the three cases, an eyedropper is required to deposit the sample onto the test and the same external reader

---

[1] By standard LFAs, the author means LFAs considered since the beginning of the study, with all the components described in section 2.1.

[2] The level is specific to the EduPack software: a high level represents a more detailed database.

[3] As a matter of fact, few information is known regarding large scale assemblies of LFA strips, especially for the striping, soaking, drying and cutting steps (cfr. Figure 1.4). Hence, they are not considered in this study. However, their impacts would probably have been very similar for the three cases.

is required for quantification. Finally, the impact assessment of nanoparticles takes the synthesis into account but not the spraying of these onto the conjugate pad.

2.1 Case 1: Standard LFAs without nanoparticles

The first case is a standard LFA test without any pre-stored nanoparticles. The materials considered for each pad in EduPack are gathered in Table 6.1. Since all the materials could not be found in the database, some deviations had to be made. However, no material close to nitrocellulose for the membrane could be found in the database. Hence, previous work made by O. Crahay [144] was used for unbacked nitrocellulose and can be found in Appendix D.

Table 6.1: Name of the material taken from the EduPack database, their corresponding part of the LFA and their geometry.

Pad	EduPack material name	Level	Length (mm)
Sample pad	Cellulosics fiber (Rayon)	3	15+0.2
Conjugate pad	Polyester (chopped glass fiber, preformed)	3	5+0.2
Membrane backing	Polyester (cast, flexible)	3	35
Absorbent pad	Cotton fiber	3	15+0.2
Adhesive card	Polyester (cast, flexible)	3	70
Release liner	Paperboard	3	70
Housing cassette	Polypropylene (PP)	2	

The considered material for sample pad (SP), conjugate pad (CP) and membrane backing (MB) in the database correspond to the real material. The sample and absorbent pads were chosen to be made out of different materials in order to compare their impacts. Cotton fiber has been reported several times in the literature for sample and absorbent pads in LFAs [17, 28].
The adhesive card (AC) and its release liners (RLs) were assumed to be made out of polyester and paperboard, respectively, based on the information found on the website of the supplier (*i.e.* Kenosha®).

Finally, given the dimensions of the LFA (7 mm wide, 70 mm long and several μm thick), the housing cassette was decided to be 20 mm wide, 90 mm long and 10 mm thick such that the tests could properly fit in it. It was assumed that the latter was made out of polypropylene[1] (PP), a strong thermoplastic typically used for packaging and protections, inspired by the housing cassette of SARS-CoV-2 autotests.

2.2 Case 2: Standard LFAs with nanoparticles

While the properties of bulk materials at the molecular level are widely understood, their surface chemistry and chemical reactivity change when their sizes are downed to the nanoscale [79, 127]. In this second case, gold and iron-oxide NPs are considered in addition to the standard LFA in order to study how their integration affects LFAs.
On the one hand, 8 to 40 nm spherical AuNPs, either covered with antibodies or with

---

[1] Since less information is known about the housing cassettes, level 2 was considered for PP to use more general data for the material, without making a distinction between its homo- or copolymer form.

NaCt, are considered. On the other hand, 20-300 nm spherical iron-oxide MNPs are investigated, either with or without a silica coating. The environmental impacts of their synthesis will be assessed based on the raw materials production and primary processing, followed by a general discussion regarding their toxicity to human health and to soils.

It should be noted that this study focuses on the synthesis of nanoparticles on a lab scale. Although the synthesis procedures are certainly different in industries, the goal here is to give a first idea regarding the environmental impact of nanoparticles.

2.3 Case 3: Biodegradable LFAs

The third case considered is an entirely biodegradable LFA, inspired by the Lia® pregnancy tests. In February 2021, Lia Diagnostics® released the world's first biodegradable and "flushable" home pregnancy test, as shown in Figure 6.3. The Lia test is made out of cellulose and biodegrades as fast as toilet paper (∼ 10 weeks). It does not contain glass fiber, nitrocellulose nor plastic. Hence, the Lia® test can either be flushed or composted and is more than 99 percent accurate, like a traditional pregnancy [185, 187].

(a) (b)

Figure 6.3: Two pictures of the Lia® pregnancy tests showing (a) a general overview of the test and (b) a comparison with traditional tests made out of plastic [185].

Since the test is recently available only in the U.S., little information about the exact composition and manufacturing of the Lia® tests is known. The few details Lia® Diagnostics have revealed is that they are fully made out of cellulose and they do not have any polyester backing, adhesive card, housing cassette, glass fiber or nitrocellulose.

The goal here is not to assess the environmental impacts of these pregnancy tests but rather inspire from this eco-design to compare standard and potentially biodegradable LFAs, knowing that 100% biodegradable LFAs exist on the market.
Hence, the tests in this third case have the same geometry as in the previous cases but are made out of a single type of paper this time, without any adhesive card, polyester backing or housing cassette.

Since no information is available about the type of paper, two papers from the EduPack database are considered: cotton fiber and tissue paper. They are the most probable ones for rendering LFA tests totally biodegradable without affecting the working principle [17, 28]. Cellulosics fiber was not considered since it not biodegradable according to the EduPack database.
It might be that the Lia tests are actually made out of hybrid materials, like combination of tissue paper and cotton fiber for example. However, considering this complicated case is not relevant at this stage of the study but should be kept in mind for further research.

In addition, no information was found whether Lia Diagnostics® uses nanoparticles and, if so, which ones. Furthermore, the company did not want to disclose any details. However, as it can be seen on Figure 6.3a, it seems that they use red labels like AuNPs, as standard LFAs do. Since these tests are biodegradable, unlike AuNPs, other biodegradable nanoparticles should have probably been used, like dyed PLGA nanoparticles for example [188, 189]. Consequently, nanoparticles will not be considered for this case.

3 Environmental impacts of the three cases

The comparison between the three cases is mainly based on three environmental impacts, namely the cumulative energy demand (CED), carbon footprint and water usage. They respectively represent the energy used, carbon dioxide emitted and volume of water needed throughout the production of a material, including the extraction and processing of the raw and auxiliary materials.

These data are available for each material in the EduPack dataset. The final CED, carbon footprint (CO_2) and water usage for the manufacture of 1 million tests of each case are gathered as such in Table 6.2. Both primary material production and processing steps are considered. The detailed calculations are presented in Appendix D.
The table is indeed very dense and does not present the data in a very illustrative way. However, the discussion will not be based on this table since the data are represented later on in graphical form. It is still given in case the reader wants more precise information or exact values of the impacts.

Table 6.2: Mass balance and environmental impacts for 1 million LFA tests of each of the three cases introduced in section 2. Data was taken from the EduPack database, [190] and [191].

Standard LFA	**Mass (kg)**	**CED (MJ)**	**CO_2 (kg)**	**Water (L)**
Sample Pad (SP)	34.63	3043.20	131.52	7895.41
Conjugate Pad (CP)	2.45	313.23	19.11	649.42
Membrane (M)	12.86	1175.10	96.55	?
Membrane Backing (MB)	34.91	3453.54	169.67	7178.01
Absorbent Pad (AP)	21.78	925.09	61.63	161172.23
Adhesive card (AC)	226.14	22369.27	1099.02	46493.36
Release liner (RL)	62.82	2676.05	2431.06	5025.44
Housing cassette (HC)	5191.00	537507.29	29050.91	193105.20
Total without HC	395.58	33955.48	4008.56	228413.87
Total with HC	5586.58	571462.76	33059.47	421519.07

Nanoparticles	**Mass (g)**	**CED (MJ)**	**CO_2 (kg)**	**Water (L)**
AuNP	2.148	2685.00	?	?
MNP	0.081	?	0.012	0.547
MNP @SiO_2	0.768	?	5.733	238.266

Biodegradable LFA	**Mass (kg)**	**CED (MJ)**	**CO_2 (kg)**	**Water (L)**
Cellulosics fiber	142.59	12530.81	541.56	32510.52
Cotton fiber	89.67	3809.18	253.77	663650.36
Tissue paper	94.33	4621.93	104.70	152806.50

3.1 Impact of standard LFAs without NPs

Figure 6.4 provides information about the impact of the different components of 1 million standard LFAs. The impact of the nanoparticles (AuNP, MNP and MNP @SiO_2) are also given but will be discussed later on.

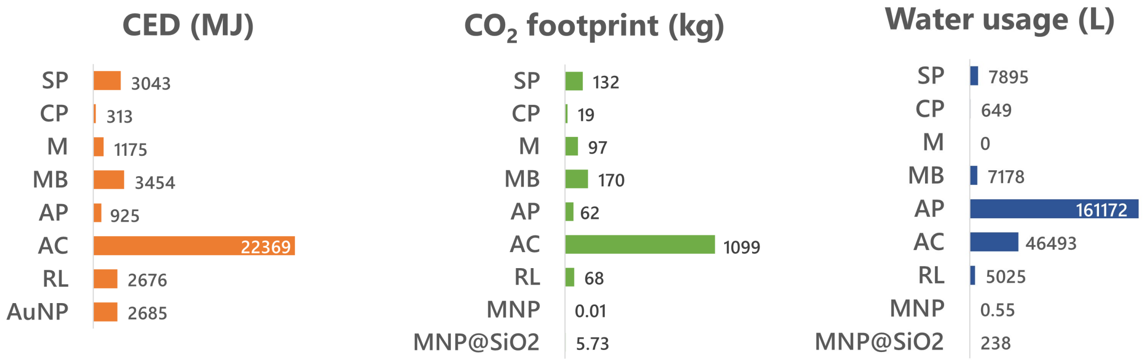

(a) (b) (c)

Figure 6.4: Environmental impacts of the different parts of 1 million standard LFAs based on (a) CED, (b) carbon footprint and (c) water usage.

First of all, it can be seen that almost all the components have a non-negligible impact for the three criteria. The conjugate pad (CP), made out of glass fiber, clearly has the lowest environmental impact. It appears that the membrane (M), made out of nitrocellulose (NC), also has a low CED and carbon footprint. This is quite surprising since NC manufacturing is known to be a polluting process [144]. No conclusion can unfortunately be made on its water usage due to lack of data. However, it should be non-negligible since many steps during the manufacture of NC involve water, like absorption of chemicals in water for example (cfr. Appendix D).

In addition, the polyester membrane backing (MB) is not the most impacting part of the LFA either. As a matter of fact, its impacts are very close to the sample pad (SP), made out of cellulosics fiber. This is surprising since one material is made from cellulose, the most abundant organic polymer on Earth, while the other is a synthetic polymer, coming from oil extraction. These high impacts for cellulosics fiber come from the extraction from raw materials, not from the primary processing.

Since sample pads and absorbent pads (AP) can both be made out of cotton fiber or cellulose, it is interesting to compare their environmental impacts. Figure 6.4 shows that cellulose (SP) has a larger CED and carbon footprint than cotton fiber (AP) by one order of magnitude. On the other hand, the water required for the cotton fiber huge compared to cellulose (two orders of magnitude).
There is a trade-off between choosing cellulosics or cotton fiber for the sample and absorbent pad: either the CED and carbon footprint are moderately increased or the water usage is strongly increased.

Finally, the adhesive card (AC, made out of polyester) clearly has the largest environmental impacts. Although this is partially due to the fact that it is the LFA-component with the largest surface area (70×7 mm^2 while 17×7 mm^2 for the SP and AP) and hence the largest mass per unit, it is also because of the material it is made out of (*i.e.* polyester).

Indeed, the RL has the same surface area but has much lower environmental impacts. The adhesive card is thus a crucial point to work on in order to improve the environmental impact of LFAs. Many other materials could improve the environmental impact of the AC. One solution could be to replace the polyester by recycled cardboard. Regarding the release liners, less solutions appear since it is already made out of paperboard, considered as an environmental-friendly material. However, as it will be discussed in the following section, their carbon footprint could be significantly reduced since the release liner is detached from the adhesive card during the LFA assembly and can therefore be easily recycled by the manufacturer.

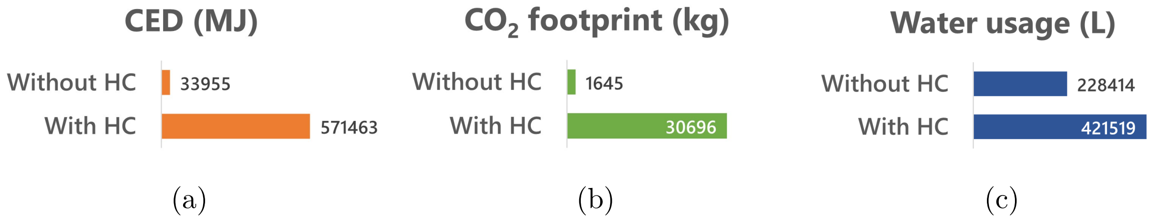

(a) (b) (c)

Figure 6.5: Comparison between a standard LFA with and without a housing cassette (HC) based on (a) CED, (b) carbon footprint and (c) water usage, both without NPs.

As already mentioned, standard LFAs available on the market are often stored in a housing cassette (HC) made supposedly out of polypropylene (PP). As it can be seen in Figure 6.5, the latter component increases the environmental impact of the LFA massively when compared to LFAs without HC. Although the dimensions of the HC influence the mass balance and thus the observed data significantly, it is clear that the housing cassette is the main component to work on in order to design more environmental-friendly LFAs.

Since the HC does not affect the working principle of the LFA, one solution could be to simply remove it. Indeed, it is mainly utilised to avoid any user mistakes, like dropping the sample somewhere else than the SP or compressing/damaging the membrane [17, 28]. Hence, by making an effort to ensure that the user handles the test correctly, e.g. with an efficient user guide provided with the test, the environmental impact of the test could be significantly improved. This was done for the Lia® tests, as shown in Figure 6.3.
Moreover, the probability of user mistakes is important for pregnancy tests or SARS-CoV-2 autotests since most of the users do not necessarily take such tests many times in their lifetime. On the contrary, for frequent water quality tests, users would use them much more often (once or even several times a day). Hence, the user would be more familiar with the working principle and make less mistakes.

3.2 Impact of nanoparticles on standard LFAs

In addition to the impacts of standard LFAs, the ones of gold and iron-oxide nanoparticles are assessed here. In addition, a general overview of their toxicity on human health and in soils is given afterwards.

Environmental impacts of nanoparticles

Few information regarding life-cycle assessments (LCAs) of nanoparticles was found in the literature. Data for assessing the environmental impacts of AuNPs and MNPs (coated with SiO_2 or not) were taken from LCAs made by Leng *et al.* [191] and Feijoo *et al.* [190], respectively. As it can be seen in Table 6.2, these studies did not provide the CED for the MNP synthesis neither the CO_2 footprint and water usage of AuNPs. Moreover, their synthesis protocols were not exactly the same as the ones described in this study.[1] However, these data give a first estimation of their environmental impacts when integrated to LFAs.

It is interesting to notice in Figure 6.4a that the production of AuNPs is not the component requiring the most energy. The CED is actually in the same range as many other components (SP, B and RL). Similarly, the carbon footprint and water usage of MNPs and MNPs @SiO_2 is also in the same range as the other components, if not smaller. Hence, as a first overview, the synthesis of nanoparticles does not seem to be the most impacting part of an LFA, when compared to the adhesive card or housing cassette.

Other interesting information is provided by Figure 6.4. First, the carbon footprint and water usage of MNP @SiO_2 are larger by two orders of magnitude than the naked MNPs. This comes essentially from the isopropanol (IPA) considered by Feijoo *et al.*[2]. In this study, no IPA was used, which would reduce the carbon footprints and water usage to even lower values.
Finally, even though CEDs cannot be compared with carbon footprints and water usages, it is tempting to say that the AuNPs seem to have larger environmental impacts than MNPs. This could be interesting to assess with a complete LCA in further research.

Health toxicity of nanoparticles

Assessing the toxicity of nanoparticles means studying the adverse poisoning effects of these particles to humans, animals and the environment [79]. The toxicity of gold and magnetic nanoparticles was reviewed in sections 2.3.5 and 2.4.7.
To cut a long story short, current knowledge is not sufficient enough to give a general conclusion regarding the toxicity of gold nanoparticles. Although AuNPs appear to present toxic effects on human health (especially on cells), more research is needed to confirm *in vitro* with *in vivo* results.
Regarding iron-oxide nanoparticles, since a normal male adult stores ∼4000 mg of iron in its body, injection of small quantities should not pose iron-linked toxicity issues[3]. However, injection of higher amounts might lead to oxidative stress and cardiac toxicity, corresponding to the *in vitro* results. Silica coating could lead to similar effects [81].

Toxicity in soils

In addition to toxicity on human health, the increasing use of nanoparticles has also raised concern in ecological and agricultural fields. In particular, soil contamination is of major concern given its importance in agriculture and in ecosystems, since it is the largest receptor for nanoparticles on earth. Javed *et al.* [192] have reviewed the effect of many different nanoparticles on soils. As an example, nanoparticles negatively affect crop growth, acting as undetectable poison in the plant, including the eatable parts. Taylor *et al.* [193] have shown that the root lengths of *Arabidopsis* seedlings grown on nutrient plates containing

---

[1] As an example, they use Polyoxyethylene (5) nonylphenylether (Igepal® CO-520) and cyclohexane before the silica coating of the MNPs, which appeared to have significant environmental impacts.

[2] They use IPA during the synthesis to stop disrupt the microemulsion used to form the silica coating

[3] Indeed, MNPs "(...) are taken up by the cells via receptor-mediated endocytosis and are presumably metabolized in the lysosomal compartment, which has (...) hydrolytical enzymes, and proteins that participate in the iron metabolism. The released free iron is then incorporated into the iron stores of the body, then gradually found as hemoglobin and in part bound to transferrin, and is mostly eliminated slowly via faecal route.", Reddy *et al.* [81]

100 mg/L of AuNP were reduced by 75%. Moreover, they observed that accumulation of nanoparticles can influence the pH of soils, affecting in turn the availability of the nutrients for plants. They also showed that metallic nanoparticles including iron-oxide reduce the amount of microscopic organisms in the soil, essential for the growing of plants. Finally, they concluded that AuNPs were non-destructive in soils up to 33 mg per kg of soil.

To sum up this toxicity assessment of nanoparticles, the studies presented in section 2.3 and 2.4 proving AuNPs and MNPs generally consider large concentrations, while only 0.002 mg of AuNPs and 0.00008 mg of iron-oxide were estimated to be used used for each LFA test (cfr. appendix D). This is reminiscent of Parcelsus and his statement: *"Sola dosis facit venenum"*, translated as "Only the dose determines the poison". Consequently, Fratoddi *et al.* [83] claim an "urgent need for standardization of employed protocols to enhance our understanding of AuNP-induced cytotoxicity".

3.3 Impact of eco-design on LFAs

In this third and last case, the standard LFAs assemblies are compared with LFAs made out of one single biodegradable material, inspired from the Lia® pregnancy tests.

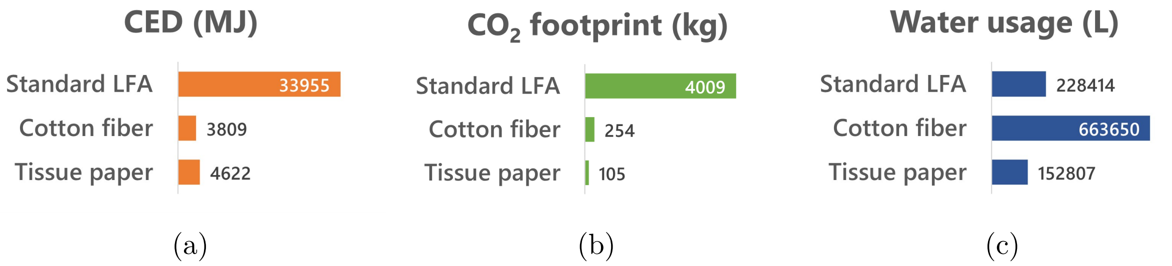

Figure 6.6: Comparison between a standard and a biodegradable LFA made of cotton fiber or tissue paper based on (a) CED, (b) carbon footprint and (c) water usage. Nanoparticles are not considered.

It can clearly be observed from Figure 6.6 that standard LFAs have a much larger CED and CO_2 footprint than the biodegradable tests made out of cotton fiber and tissue paper. This is not surprising since no adhesive cards nor membrane backing are used in the latter case, which were found to have the largest environmental impacts for standard LFAs.
Regarding the water usage, while the consumption of standard LFAs is in the same range as the ones made out of tissue paper, the water consumption is three times larger for tests made out of cotton fiber.

To sum up, manufacturing biodegradable tests made out of one single material seem to have a very positive impact on the environment, especially regarding the CED and the CO_2 footprint, while the water usage remained in the same order of magnitude.
Although very interesting on an environmental point of view, much research lies behind these biodegradable tests. The use of the different pads and materials have been proven to be essential for the proper functioning of the standard LFAs. Replacing them by one single material, whether it is cotton fiber or tissue paper, is not that easy. This makes the new Lia® pregnancy tests even more impressive.

4 End-of-life strategies

Lateral flow assays are for single use. They thus produce significant amounts of waste: 5.5 tons per 1 million tests based on the mass balance from Table 6.2. However, all the different parts of LFAs are not necessarily intended to finish in landfills. Some are biodegradable or recyclable for instance. Hence, in order to enlarge the responsible design discussion for lateral flow assays, the end-of-life of the different materials is discussed.

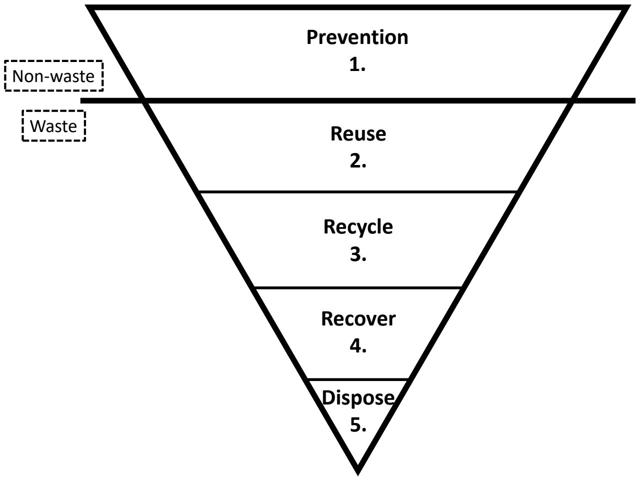

Figure 6.7: Waste hierarchy, inspired from [194].

To this end, the waste hierarchy proposed in the Waste Framework Directive 2008/98/EC (WFD2008) and shown in Figure 6.7 will be used as model for assessing the possible ways to treat LFA tests after being used for detection of bacteria in water samples.
The waste hierarchy defines the preferred approach to treat waste. In the WFD2008, waste is defined as “any substance or object which the holder discards or intends to discard or is required to discard” [194].

Prevention

According to Figure 6.7, the best strategy is prevention. This means rethinking the needs and redesigning business models in order to prevent any waste creation. Since the goal of this project is to fight against water pollution by bringing information about water potability, it is assumed that the prevention has already been optimized and will thus not be further discussed.

Reuse

The second strategy is to prepare the object and its components so that they can be re-used without any pre-processing. Although difficult since many components are contaminated with nanoparticles and bacteria after use, this could be a very interesting research topic for LFAs. One could for example think of designing modular LFAs, where the sample and absorbent pads could be unplugged from the test, washed, dried and re-used for another test. However, this is a bit Utopian since LFAs are very sensitive to any contamination or damage of their pads. As an example, if all the bacteria are not totally washed away, the following tests could lead to false results.
However, all the components are not necessarily contaminated by the sample or by nanoparticles. The housing cassette could surely be designed such that it could be re-used

for each test. One way would be to sell many LFA strips with only one housing cassette designed as an openable box, such as shown in Figure 6.8. The user would then simply open the box, withdraw the used LFA, dry the box if necessary, place the new strip, close the box and drop the new water sample. This would significantly reduce the huge environmental impacts of the HC.
In addition, since the HC ensures a proper functioning of the test[1], it would not be simply removed, like Lia Diagnostics® did for their test. Instead, it would be re-usable. Further improvements could be brought regarding the re-usability of the HC, for example by replacing polypropylene with a more durable material like stainless steel or even wood.

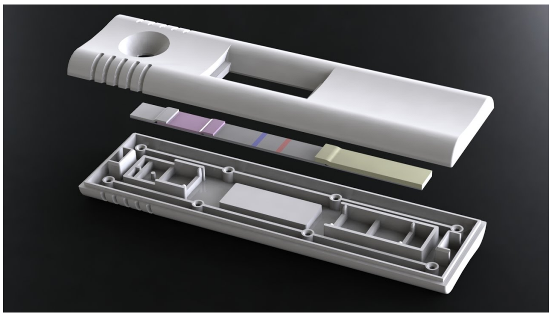

Figure 6.8: Openable Housing cassette containing the LFA strip [195]

Recycle, Recover, Biodegrade, Dispose

The next three strategies are discussed together thereafter. In the waste hierarchy, the third best strategy is recycling, *i.e.* converting the material into a new one of similar grade. Then come the other recoveries in fourth place, including energy recovery from combustion for example, where the calorific content of a material is recovered by combustion. Finally, the fifth and worst strategy in the waste hierarchy is disposal in landfills, where nothing is recovered at all from the material. It should be noted that biodegradability does not appear in the waste hierarchy. In reality, it is included in this fifth strategy, but remains better than disposing non-biodegradable materials. Interestingly, while biodegradability is widely thought to be a very nice strategy for end-of-life of materials, it is in reality at the end of the waste hierarchy, since no material neither energy is recovered from it [196].
Except for the housing cassette for which an EoL strategy has already been proposed, the waste hierarchy can be used to do the same for the other materials used in LFAs. To this end, Table 6.3 shows whether the materials do (in green) or do not (in red) comply to one of these strategies. Since data for nitrocellulose is not given in the EduPack database, it was assumed to be close enough to celluloid, corresponding to plasticized NC with 20% of camphor. Since it is made from NC, it was assumed that if celluloid is recyclable or biodegradable, then it is the case for virgin NC too.

First of all, it appears that nitrocellulose, paperboard and polypropylene, initially thought to be the worst materials for the environment, are the only recyclable materials in standard LFAs. Tissue paper is also recyclable and will be discussed later on. Recycling the NC membrane after using the LFA test is very complicated since it contains nanoparticles, bacteria and other micro-organisms from the sample. In addition, since it is most often provided with a polyester backing by the suppliers, which is not recyclable given Table 6.3, energy recovery from its combustion seems to be the best end-of-life strategy for the

---

[1] As a reminder, the goal of the housing cassette is to avoid any user mistakes like dropping the sample on the wrong pad or damaging the membrane.

Table 6.3: The materials used in an LFA and how they suit to the waste hierarchy, according to the EduPack database.

Material	LFA part	Recycle	Combustion	Biodegradable	Landfill
Cellulosics fiber	SP	x	x	x	v
Glass fiber	CP	x	v	x	v
Polyester	B, AC	x	v	x	v
Nitrocellulose	M	v	v	x	v
Cotton fiber	AP	x	v	v	v
Paperboard	RL	v	v	v	v
Polypropylene	HC	v	v	x	v
Tissue paper		v	v	v	v

membrane and its backing.
On the other hand, as it was already discussed, instead of recycling the polypropylene, it is even better to re-use it. Furthermore, after re-using it several times, the housing cassette could be recycled instead of disposed in landfill.

Furthermore, it was found in the previous sections that the release liner was a component of the standard LFA with one of the largest environmental impact after the adhesive card. This impact is significantly reduced since paperboard is recyclable. Since the RLs are removed during the LFA assembly, they are not contaminated by the sample and do not stick to any other component. Hence, it can be easily sorted out by the manufacturer for further recycling. Re-use of the release liners could be difficult since the adhesive cards might not be manufactured at the sample place where the LFAs are assembled.

It appears that the remaining materials can all be combusted to recover energy from it, except cellulosics fiber. The end-of-life of the adhesive card, made out of polyester, could be the same as the backed NC which sticks to it, *i.e.* combustion for energy recover. The same goes for the absorbent and conjugate pads made out of cotton and glass fiber, respectively. The problem comes from the sample pad, made out of cellulosics fiber. Indeed, since it can only be disposed in landfills, either the whole test should follow the sample pad in landfills or the sample pad could be made out of cotton fiber as the absorbent pad, at the expense of increasing the water usage of the test significantly. However, since cellulosics fiber had a larger CED and CO_2 footprint and no energy can be recovered from it, replacing it with cotton fiber seems to be a better option.

Finally, going back to the biodegradable tests either entirely made out of cotton fiber or tissue paper, it appears at first in Table 6.3 that both materials are indeed biodegradable. However, as already mentioned, although biodegradable tests are better than disposing them in landfills, the EoL strategy could be even more improved by recycling some non-contaminated parts or recovering energy from it. Since cotton fiber is not recyclable and requires a huge amount of water in contrast to tissue paper, the latter seems to be the best choice for eco-designing LFAs. Although this seems difficult to design given the complex microfluidic properties of tissue paper compared to cotton fiber or nitrocellulose, it has been done by Lia Diagnostics®, which used a material similar to tissue paper.

5 Conclusions and outlooks

In this introduction to responsible design for lateral flow assays, the most impacting parts and materials of the assembly were pointed out and end-of-life strategies were proposed for large scale manufacturing.

First, there is a trade-off between selecting cellulosics or cotton fiber for the sample and absorbent pads. The former has a much lower water usage while the latter has a lower CED and carbon footprint, can be recycled and is biodegradable. Cotton fiber seems to be a more suitable choice but further study should be undertaken to confirm it. After use, if both pads are made out of cotton fiber, they can be partially[1] withdrawn from the adhesive card and recycled.

Second, it was observed that the adhesive card has the largest environmental impact of the LFA strip. One solution is to make it out of another material than polyester, like recycled cardboard for example, and try to design the LFA strip such that the adhesive card can be withdrawn and recycled separately from the other pads and membrane. If this appears to be too difficult, it would adopt the same end-of-life as the backed nitrocellulose, namely combustion for energy recovery imposed by the polyester backing.
Furthermore, it might also be interesting to assess the toxicity of the glue used on the adhesive card should be studied, as well as the different buffer and blocking agents used to prepare the different pads.

Third, the conjugate pad made out of glass fiber would follow the same strategy as the adhesive card (*i.e.* combustion for energy recovery) since it relies on the unique properties of glass fibers which cannot be recycled. It is the LFA part with the lowest environmental impact.

Fourth, the release liners are already made out of an environmental-friendly material, *i.e.* paperboard. Since they are detached from the adhesive card during the assembly and are thus not contaminated by the sample, they can be easily sorted out and recycled by the manufacturers themselves.

Fifth, the housing cassette made out of polypropylene respectively multiplies the CED, carbon footprint and water usage of LFAs by 17, 8 and 2. It is therefore the main component for which the environmental impacts have to be reduced. Two solutions are proposed. On the one hand, the housing cassette is omitted, like Lia® tests did, and the manufacturer provides a clear use guide to prevent any error of manipulation from the user. On the other hand, the housing cassette is designed as an openable box where the strips can be inserted and withdrawn after use, thereby decreasing its environmental impact significantly.
While the first option fits to the best strategy in the waste hierarchy, *i.e.* prevention, the second one is more attractive since the housing cassette still reduces the potential user mistakes and protects the LFA. In this strategy, the housing cassette can be made out of another more durable material, like stainless steel or wood, in order to increase its lifetime. A material selection procedure should be undertaken in order to find the best material for this application.

---

[1] It has been experienced that, although a thin layer of cotton fiber remains stuck to the adhesive card, most of the pad can be effectively removed.

Sixth, although non-negligible, the impact of nanoparticles does not seem to have a critical impact on the CED, carbon footprint and water usage of LFAs. However, a complete LCA should be undertaken since the data was taken from the literature, which did not use the same synthesis procedures as in the experimental section of this study. Moreover, the data might change when considering large scale manufacture of nanoparticles. It could also be interesting to compare the environmental impacts of MNPs coated with silica or with AuNPs, as proposed in the previous sections. Moreover, given the lack of information available in the literature, even though it seems that gold and iron-oxide nanoparticles are not totally harmful, it is difficult to make a final conclusion regarding the toxicity of these nanoparticles since it depends much on their concentration. However, at this stage, the toxicity of the nanoparticles appeared to be a minor point towards the development of low-impact biosensors.

Finally, eco-design inspired from the Lia® test clearly offers many advantages since it does not require any nitrocellulose, glass fiber or polyester. The best solution would be to make LFAs out of tissue paper because of its low CED, CO_2 footprint and water usage, try to recycle them if recycling facilities are available and interested, if not, dispose them in a compost given their biodegradable properties. However, much research is required, especially regarding the microfluidic properties, since the tissue paper should adopt similar properties as cotton fiber, glass fiber and nitrocellulose, altogether. Ideally, a partnership with the Lia Diagnostics® company would help considerably since they apparently managed to reach this goal.

Chapter 7

Conclusions and perspectives

Within the development of low-impact paper-based biosensors for quantitative bacteria detection in remote area water samples, this master thesis aimed at studying gold and magnetic nanoparticles for LFA applications in order to open new electrical and magnetic detection opportunities.

First of all, gold nanoparticles were synthesized, characterized and compared with commercial ones. The impact of the molar ratios of NaCt to $HAuCl_4$ on the size, shape and dispersion of the particles was investigated. A molar ratio of 3.7 led to promising 8 nm sized AuNPs ready to be conjugated with bio-receptors. They were found to have a low polydispersity and a good dispersion.

Then, iron-oxide magnetic nanoparticles were synthesized and subsequently coated with silica. Three different synthesis methods were investigated, from which co-precipitation and thermal decomposition led to sizes of around 14 and 12 nm, respectively. The former was successfully coated with a 4 nm thick shell and made ready for further bio-conjugation. The latter was proposed to be coated with phosphonate groups instead of silica in order to take advantage of the already existing ligands. In addition, larger MNPs of around 110 nm were successfully coated with a mesoporous silica layer of 15 nm thick, proposing higher surface area for further bioreceptor attachment.

Furthermore, magnetic cores were successfully coated with homemade AuNPs. Although the density of gold at the surface can be significantly improved, such core-shell structures offer the opportunity to combine colorimetric, electrical and magnetic detection altogether in one single LFA.

After that, the microstructures of the papers used in LFAs were characterized. The pores were observed to be much larger than the nanoparticles (several μm to maximum hundreds of nm) but the nanoparticles interacted much with the fibers. As a consequence, the use of blocking agents appeared to be very important for further research.

Finally, the environmental impacts of 1 million LFA tests was assessed to anticipate the adverse effects of the large-scale production of LFAs. It was found that the housing cassette was the most impacting component and an eco-design solution consisting of an openable box reusable after each assay was proposed. In addition, the impact of nanoparticles appeared not to be critical compared to the other components but this should be confirmed by further LCAs. Their toxicity was also concluded not to be critical but a severe lack of information appeared. Last, it was concluded that considering biodegradable tests reduces environmental impacts very significantly, but that it entails much research that should not be carried out at this stage of the project.

To conclude, this master thesis allowed to have a deep overview about the different ways to obtain nanoparticles for biosensing applications. Most of the gold and magnetic nanoparticles obtained in this study are ready for further conjugation with bioreceptors to subsequently detect and bind to the bacteria. They can further allow for colorimetric, electrical and magnetic detection to provide both qualitative and quantitative results about the presence of harmful bacteria in remote area water samples. To this end, AuNPs coated MNPs revealed the most promising properties since they combine these three detection methods altogether. Perspectives of this thesis consist of three main paths: (i) a deeper characterization/quantification of colorimetric, electrical and magnetic properties, (ii) the bio-conjugation of the NPs with the bioreceptors and (iii) the use of blocking agents for further microfluidic tests of NPs in LFAs.

Appendices

Appendix A

Bio-conjugation of nanoparticles: further information

Bio-conjugation via adsoprtion

Bio-conjugation *via* adsorption is especially used for AuNPs and CNPs. This strategy uses non-covalent modes of binding based on a combination of ionic and hydrophobic interactions of the antibody and the NP surface.

Hydrophobic interactions are due to attraction between hydrophobic parts of the antibody and the metal surface that result in the formation of a non-covalent bonds. Ionic interactions are formed between the negatively charged surface of the particles and the abundant positively charged groups in antibodies [74]. Generally, the NPs are incubated and left under orbital shaking with the antibody (time and temperature can differ from protocol to protocol). The pH of the NP colloidal suspension must be near the isoelectric point (pI)[2] in order to facilitate electrostatic interactions and Van der Waals forces with the antibodies. A blocking agent is used to avoid NP aggregation and unspecific binding to other molecules. Bovine serum albumin (BSA) is most often used. A centrifugation step is necessary afterwards to remove the excess BSA and the non-adsorbed antibodies [16].

Non-covalent strategies have several drawbacks: a high concentration of antibodies is necessary, antibodies orient randomly at the NP surface, the binding is influenced by changes in pH and Ab can desorb and be replaced by other molecules in biological samples as they are non-covalently conjugated [74, 75].

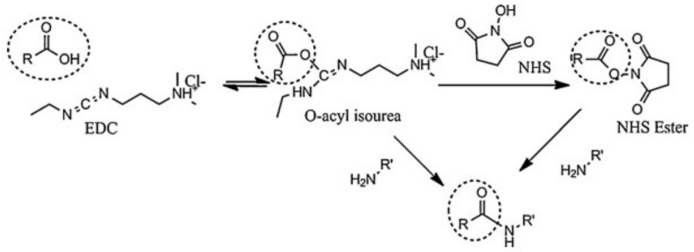

Figure A.1: Schematic carbodiimide coupling between a carboxylic acid and an amine group by means of EDC/NHS chemistry [73].

---

[2] The pI is the pH at which a molecule carries no net electrical charge [197].

Bio-conjugation via carbodiimide coupling

Bioconjugation *via* carbodiimide coupling covalently links carboxylic acids to amines via formation of a "zero length" amide bond [73]. After adding carboxylic groups in the form of a polymer coating in the primary coating step (see subsection 2.2.1), a peptide bond is formed between the nanoparticle and the label by means of EDC/NHS chemistry. This kind of chemistry uses 1-ethyl-3- (3-dimethylaminopropyl) carbodiimide (EDC) to "activate" the carboxylic groups to form a highly reactive intermediate reacting with the amine groups present in the antibodies and N-hydroxysuccinimide (NHS) to stabilise the intermediate. A schematic covalent coupling of carboxylic acid to an amine group by EDC/NHS cemistry is shown in Figure A.1. The main disadvantage of using EDC/NHS chemistry is that the number of binding sites can be negatively affected, as the carboxylic groups available from the labels can also react with the N-terminus primary amine of the antibodies, shown in green in Figure 1.13b [16, 73].

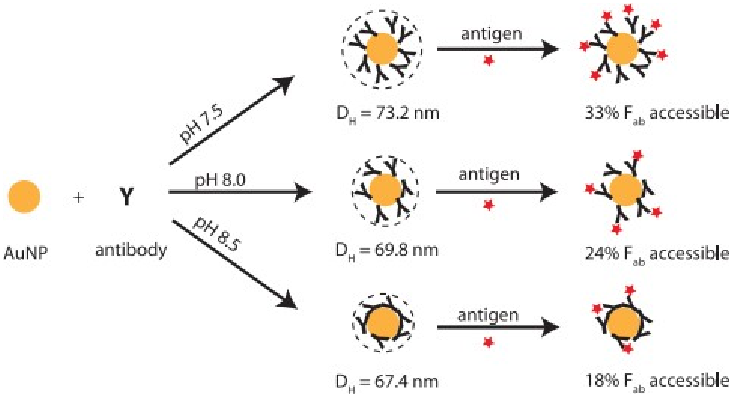

Figure A.2: Orientation of Ab on gold nanoparticles with different pH [198].

Parolo *et al.* [70] have reported that the orientation of the antibodies on the AuNPs has a significant effect on the LoD of the LFA test. The orientation can be controlled by varying the pH around the pI of the NP solution, for both bio-conjugation methods [70, 198, 199]. Briefly, the technique is based on the fact that when the pH of an antibody solution is lower than the pI of the antibody, the concentration of positive charges in the stem of the antibody is high. Thus, if the antibodies are in solution with negatively charged NPs, they most likely interact through their C-terminus with the surface of the NPs. This controlled approach guarantees that the antigen binding sites remain accessible [70]. As it can be seen in Figure A.2, by playing with the pH, it is possible to increase the amount of F_{ab} fragments accessible for antigen binding, which subsequently improves the LoD of the assay [198].

Appendix B

Crystallites size with Scherrer's equation

Scherrer's equation is rewritten in Equation B.1, where D (nm) is the nanoparticles crystallites size D, k is a shape factor equal to 0.89, λ (nm) is the wavelength of the incident X-rays, β (°) is the full width at half maximum of the diffraction peak and θ (°) is the diffraction angle.

$$D = \frac{k\lambda}{\beta \cos\theta} \tag{B.1}$$

Based on the values given in Table B.1, the crystallites sizes D can be estimated for the different MNPs.

Table B.1: Crystallites size D of nanoparticles based on Scherrer's equation B.1.

Sample	λ (nm)	2θ (°)	β (°)	D (nm)
Co-prec.	0.15	30.4	0.6	14.2
Thermal D.	0.15	30.6	0.7	12.5
Commercial	0.15	30.2	0.1	67.2

Appendix C

Additional results

UV-Vis spectra of MNPs

The UV-Vis spectra of three different MNPs are shown in Figure C.1. The observed colors of the MNP-CP, MNP-TD and commercial MNP solutions were orange, brown and black, respectively, with the naked eye. The negative absorption of the commercial MNPs is due to an error with the solvent calibration. Since the solution was black, it should have probably absorbed much for all wavelengths.

The curves of the MNP-CP and MNP-TD have different shapes than the AuNPs in Figure 4.3. No distinctive peak is apparent. Their absorption also tends to 0 towards infrared rays and to non-zero values towards UV wavelengths. This shape is confirmed by other studies such as [177].

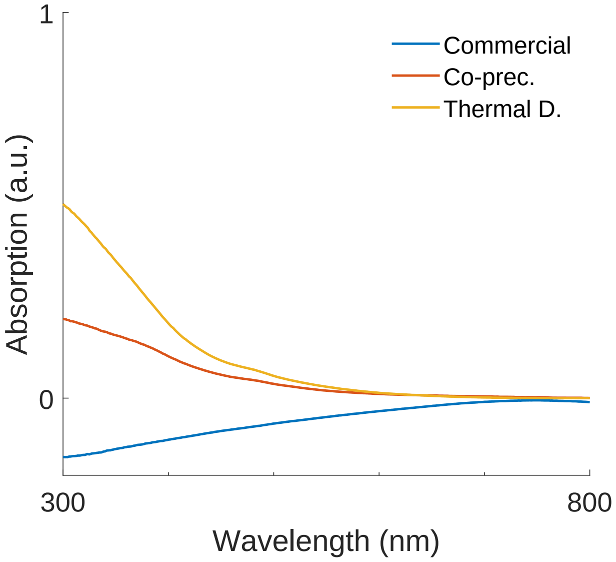

Figure C.1: UV-Vis spectra of MNP-CP, MNP-TD and commercial MNPs.

MFM on MNP @Mesoporous SiO_2

The commercial MNPs coated with mesoporous silica were characterized by Magnetic Force Microscopy (MFM) by Grégoire Le Brun. The resulting image are shown in Figure C.2.

Briefly, there are two operating modes with MFM. On the one hand, the tapping mode provides topographical information about the sample. The MFM tip is then close with the sample surface. On the other hand, the Lift mode provides information regarding the magnetic properties of the sample. The MFM tip is held further from the sample and only the magnetic forces are measured.

One single and more or less spherical MNP of ∼100 nm can be observed both by tapping and lift mode. In the latter mode, as a gradient is observed, it confirms the magnetic behavior of the commercial MNPs. The mesoporous SiO_2 cannot be distinguished because it is not magnetic.

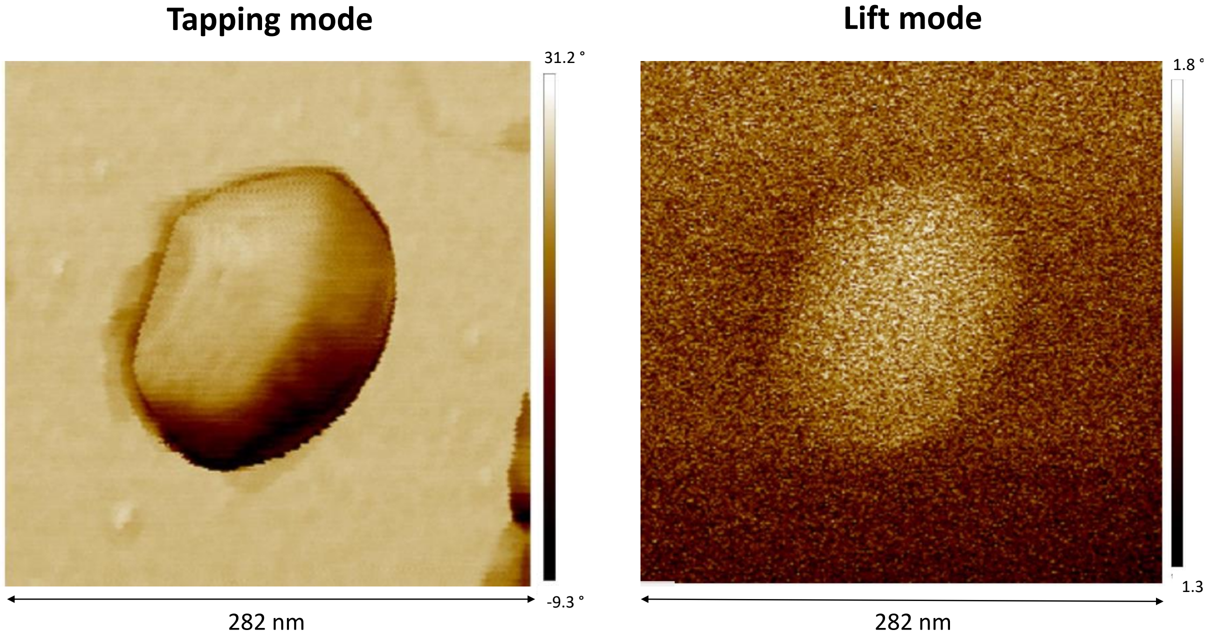

Figure C.2: MFM images of a single MNP @Mesoporous silica.

MNP @AuNP: Further results

The results shown below in Figures C.3 and C.4 come from Salgueriño *et al.* [177]. Similar results obtained by UV-Vis spectroscopy and SQUID could be obtained by further research using the MNP @AuNP presented in this study. In this way, the colorimetric and magnetic properties of these structures could be confirmed.

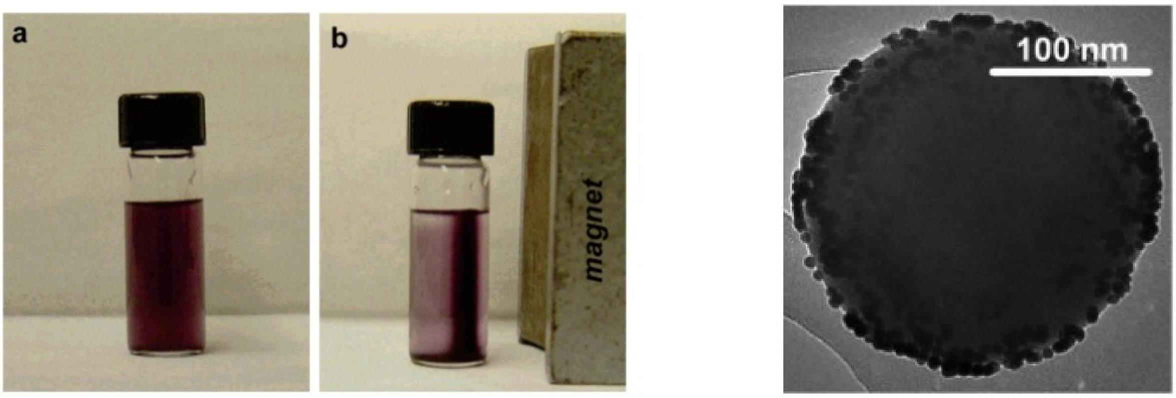

(a) (b)

Figure C.3: (a) MNP @AuNP before and after approaching a magnet to it, (b) TEM image of the MNP @AuNP [177].

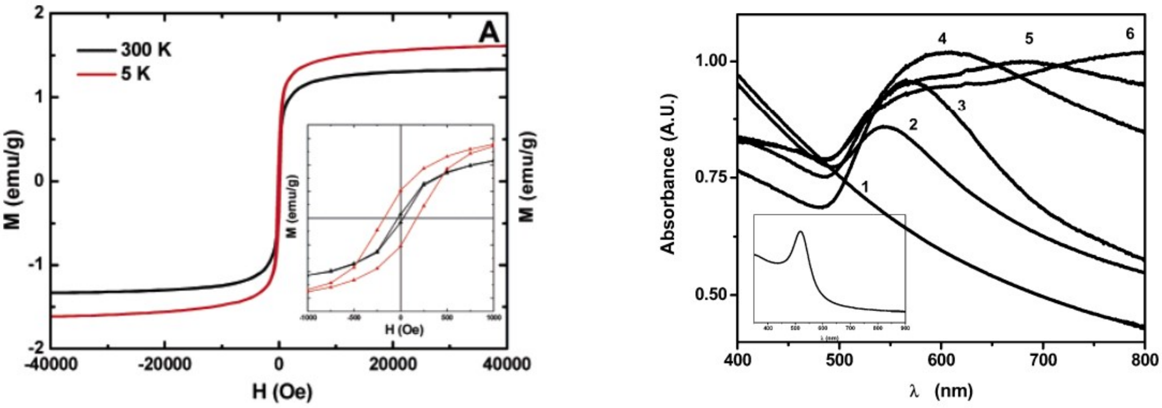

(a) (b)

Figure C.4: (a) Hysteresis loops recorded at 5 (red line) and 300 K (black line) by SQUID, (b) UV-Vis spectra of the MNP @AuNP where curves number 1 and 2 correspond to the magnetic spheres before and after deposition of the 15 nm gold nanoparticles. The inset shows the initial UV-Vis spectrum of the colloidal AuNPs [177].

Appendix D

Calculations behind environmental impacts

Nitrocellulose data

The processes from raw materials to nitrocellulose are described below and were taken from previous work made by O. Crahay [144]. The flowsheet of the different processes is shown in Figure D.1. The cumulative energy demands (CED) and carbon footprints of each chemical used are gathered in Table D.1.

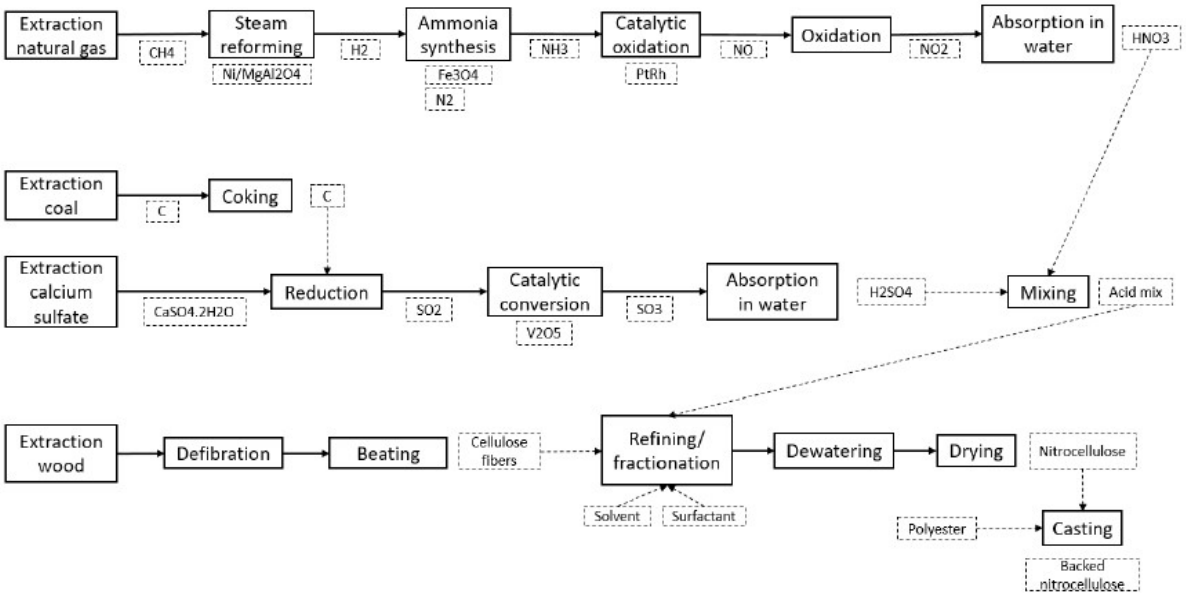

Figure D.1: Flowsheet of the manufacturing of nitrocellulose from raw materials to the final product.

Table D.1: Cumulative energy demand and carbon footprint of the chemicals used to manufacture 1 kg of nitrocellulose, taken from [144].

Chemical	CED (MJ/kg_{NC})	CO_2 footprint ($kg_{CO_2,eq}/kg_{NC}$)
CH_4	3.843	0.282
$Ni/MgAl_2O_4$	$1.309 \cdot 10^{-5}$	$8.904 \cdot 10^{-7}$
H_2	0.272	2.146
Fe_3O_4	$1.994 \cdot 10^{-7}$	$1.526 \cdot 10^{-8}$
N_2	0.099	0.009
NH_3	5.622	0.490
PtRh	0.057	0.029
HNO_3	-1.018	1.775
C	1.908	0.021
$CaSO_4 \cdot 2H_2O$ (gypse)	3.886	0.353
V_2O_5	$1.248 \cdot 10^{-4}$	?
H_2SO_4	0.878	0.178
Solvent (C_3H_6O)	48.540	1.569
Surfactant	$6.832 \cdot 10^{-5}$	$5.626 \cdot 10^{-6}$
Cellulosic fibers	27.272	0.655
Total	91.358	7.507

Standard LFAs

Mass balance

The mass balance for standard LFAs can be found in Table 6.2. The basis weights (g/m^2) were the ones given by the respective suppliers, shown in Table 3.3, except for the backing, adhesive card and release liner, for which the basis weights were determined with a microbalance. The mass of one pad was thus calculated by multiplying the basis weight by the pad area (cfr. Figure 3.1).

For the mass of the housing cassette, a hollow rectangle parallelepiped of 90x20x10 mm with walls of 1 mm thick was considered. The density of polypropylene (PP) is equal to 895 kg/m^3. Hence, one housing cassette weighs 5.19 g per unit and 1 million tests require 395.58 kg of PP.

Instead of taking the basis weights from the suppliers, the densities given by EduPack could have been used. This has been done and it gave a similar mass balance (same order of magnitude). Hence, to stay as close as possible to the real problem, basis weights from suppliers were kept.

Manufacture

Different processes for each material were described in the EduPack database. The energy, carbon footprint and water usage of each process was given by kg of material produced. Hence, by multiplying these with the mass balance from Table D.2, the values from Table D.3 are obtained.

Table D.2: Mass balance for a standard LFA, data from respective suppliers.

	Material	Basis weight (g/m^2)	Mass/unit (g)	Mass/1M (kg)
SP	Surewick® C083	291.0	0.035	34.63
CP	Reliaflow™ 8950	50.0	0.002	2.45
M	Unisart® CN95	52.5	0.013	12.86
B	Polyester	142.5	0.035	34.91
AP	Reliaflow™ 237	183.0	0.022	21.78
AC	KN-2211™	461.5	0.226	226.14
RL	Paperboard	128.2	0.063	62.82
HC	Polypropylene		5.191	5191.0

Table D.3: Embodied energy, carbon footprint and water usage for the primary production and processing of the pads for 1M tests.

	Primary production			**Processing**		
	Energy (MJ)	CO_2 (kg)	Water (L)	Energy (MJ)	CO_2 (kg)	Water (L)
SP	2957.32	124.66	7895.41	85.88	6.86	0.00
CP	124.95	4.36	551.25	188.28	14.74	98.17
M	1175.10	96.55	?	0.00	0.00	0.00
B	2370.56	84.14	6633.38	1082.99	85.58	544.64
AP	871.08	18.51	161149.80	54.01	43.12	22.43
AC	15354.57	544.99	42965.65	7014.71	554.03	3527.71
RL	2676.05	2431.06	5025.44	0.00	0.00	0.00
HC	342086.90	14379.07	193105.20	195420.39	14671.84	0.00

Standard LFA with NPs

AuNPs

Few LCAs for the synthesis of AuNPs are available in the literature. Leng *et al.* [191] calculated the cumulative energy demand of the synthesis of 1 mg of AuNPs (15 nm diameter) at room temperature and at 100°C. At room temperature, they obtained a CED of 1.25 MJ/mg for 15 nm sized AuNPs. This value is further considered since the AuNPs in this study were synthesized at this temperature.

In order to use this result to this study, the mass of AuNPs needed for 1 million LFA tests must be determined. Parolo *et al.* [17] stated in their tutorial that a solution of 100 μL of water with 20 nm AuNPs suspended were used, with an optical density (OD) of 0.45 at 520 nm. To keep a coherence with the data from Leng *et al.* [191], it was assumed that 15 nm AuNPs were used instead of 20 nm.

Data regarding the mass of AuNPs per mL of solution in function of the OD is provided by Bio-based Industries Joint Undertaking [200] and is gathered in Table D.4. No information for OD of 0.45 at 520 nm is provided. However, it can be seen that there is a linear relation between the OD and the number of particles per mL of solution. Hence, the values for an OD of 0.45 can be easily calculated. We get $2.148{\cdot}10^{-5}$ g/mL in this case. Since we use 100 μL per test, $2.148{\cdot}10^{-6}$ g of AuNPs are required for each test. Thus, for 1 million tests, 2.148 g of AuNPs are required.

Finally, the CED for the production of 2.148 g of 15 nm AuNPs for 1 million LFA tests is equal to 2685 MJ.

Table D.4: Information about the mass of AuNPs in solutions of different optical densities (OD) at 520 nm on the spectrum, taken from [200].

Diameter (nm)	OD @520 nm (-)	Mass 1 AuNP (g)	No. particles/mL (1/mL)	Mass AuNP/mL (g/mL)
15	1	$3.41{\cdot}10^{-17}$	$1.40{\cdot}10^{12}$	$4.77{\cdot}10^{-5}$
15	5	$3.41{\cdot}10^{-17}$	$7.00{\cdot}10^{12}$	$2.39{\cdot}10^{-4}$
15	10	$3.41{\cdot}10^{-17}$	$1.40{\cdot}10^{13}$	$4.77{\cdot}10^{-4}$
15	0.45	$3.41{\cdot}10^{-17}$	$6.30{\cdot}10^{11}$	$2.15{\cdot}10^{-5}$

MNPs

In the same way as for AuNPs, the environmental impacts of iron-oxide magnetic nanoparticles can be estimated. Feijoo *et al.* [190] compared four MNP synthesis based on co-precipitation to obtain sterically-stabilized MNPs, PEI coated MNPs, oleic acid coated MNPs and silica coated MNPs. In this study, oleic acid (similar to the naked MNPs obtained by co-precipitation) and silica coated MNPs obtained by co-precipitation are considered. Their sizes were respectively equal to 7.8 and 21.5 nm. The thickness of the silica shell is thus equal to 13.7 nm. The carbon footprint and water usage for each synthesis are gathered in Table D.5.

The mass of MNP required for 1 million LFA tests can be estimated from their density (g/cm^3). Sigma-Aldrich[1] gives a density of 5.2 g/cm^3 for the magnetic core. Similarly, the density of amorphous silica is equal to 2.2 g/cm^3.[2]
Assuming that the MNP core of 7.8 nm has a spherical shape, its volume is equal to $2.48{\cdot}10^{-19}$ cm^3. Similarly, the volume occupied by the silica coating is equal to $4.96{\cdot}10^{-18}$ cm^3. The mass per particle can thus be calculated and the values are presented in Table D.5.

Table D.5: Carbon footprint and water usage for MNP and MNP @SiO$_2$ synthesis, taken from [190].

MNP	Mass 1 particle (g)	CO$_2$ footprint (kg$_{CO_2}$/kg$_{MNP}$)	Water usage (L/kg$_{MNP}$)
MNP @Oleic acid	$1.29{\cdot}10^{-18}$	150.91	6727
MNP @Silica	$1.22{\cdot}10^{-17}$	7460.00	310000

The number of particles per test must now be considered. To this end, since few information are available, the same concentration of particles per mL as the gold nanoparticles is used, *i.e.* $6.3{\cdot}10^{11}$ mL^{-1}. This is an approximation but the real value should not be far since both considered NPs have similar diameters (20 nm for AuNPs and 21.5 nm for the MNP @SiO$_2$). Moreover, it is supposed that 100 μL of this solution is used for each test. In the end, for 1 million tests, 0.0813g of MNP or 0.769 g of MNP @SiO$_2$ are used. Based on this, the carbon footprint and water usage can be calculated given the data from Table D.5.

---

[1] `https://www.sigmaaldrich.com/catalog/product/aldrich/637106?lang=fr&region=BE`

[2] `https://en.wikipedia.org/wiki/Silicon_dioxide`

Biodegradable LFA

Mass balance

The mass balance for the biodegradable LFAs is given in Table D.6. The basis weights (g/m^2) were the same as for the standard LFA for cellulosics fiber and cotton fiber.
The basis weight of the tissue paper was calculated from the density given by EduPack (200 kg/m^3) and the assumed thickness of the paper (0.7 mm), inspired from commercial toilet paper.

Table D.6: Mass balance for a biodegradable LFA inspired from Lia® tests, with three material possibilities.

Material	Basis weight (g/m^2)	Mass/unit (g)	Mass/1M (kg)
Cellulosics fiber	291.0	0.14	142.59
Cotton fiber	183.0	0.09	89.67
Tissue paper	192.5	0.09	94.33

Manufacture

The embodied energy, carbon footprint and water usage for each material was calculated from the data given by EduPack and the mass balance from Table D.6. The final values for the primary production and processing are given in Table D.7.

Table D.7: Embodied energy, carbon footprint and water usage for the primary production and processing of 1M of each test.

	Primary production			**Processing**		
Material	Energy (MJ)	CO_2 (kg)	Water (L)	Energy (MJ)	CO_2 (kg)	Water (L)
Cellulosics fiber	12177.19	513.32	32510.52	353.62	28.23	0.00
Cotton fibers	3586.80	76.22	663558.00	222.38	177.55	92.36
Tissue paper	4621.93	104.70	152806.50	0.00	0.00	0.00

Bibliography

[1] ScienceDaily. Water scarcity, 2015. ScienceDaily, https://www.sciencedaily.com/terms/water_scarcity.htm, Accessed: 31/05/2021.

[2] UN-Water. Water Facts - Scarcity, 2021. UN-Water, https://www.unwater.org/water-facts/scarcity/, Accessed: 02/05/2021.

[3] World Data Lab. Water Scarcity Clock, 2021. World Data Lab, https://worldwater.io/, Accessed 31/05/2021.

[4] United Nations Children's Emergency Fund. Water scarcity: Addressing the growing lack of available water to meet children's needs., 2021. UNICEF, https://www.unicef.org/wash/water-scarcity, Accessed: 31/05/2021.

[5] World Health Organization. Water safety and quality, 2021. WHO, https://www.who.int/teams/immunization-vaccines-and-biologicals/diseases/tick-borne-encephalitis/water-sanitation-and-health, 31/05/2021.

[6] Claudio Parolo, Mariana Medina-Sánchez, Alfredo de la Escosura-Muñiz, and Arben Merkoçi. Simple paper architecture modifications lead to enhanced sensitivity in nanoparticle based lateral flow immunoassays. *Lab on a Chip*, 13(3):386–390, January 2013. Publisher: The Royal Society of Chemistry.

[7] Daniel Quesada-González and Arben Merkoçi. Nanoparticle-based lateral flow biosensors. *Biosensors & Bioelectronics*, 73:47–63, November 2015.

[8] Grégoire Le Brun. Scientific section of the proposal. *FRIA CALL 2019 - FRIA-B1*, 2019.

[9] Belgium.be. Autotest Covid-19 | Coronavirus COVID-19, 2021. https://www.info-coronavirus.be/fr/autotest/, Accessed: 12/04/2021.

[10] The Local. EXPLAINED: How France's new Covid home-testing kits work, April 2021. The Local, https://www.thelocal.fr/20210316/explained-how-frances-new-covid-home-testing-kits-work/, Accessed: 12/04/2021.

[11] Claudio Parolo and Arben Merkoçi. Paper-based nanobiosensors for diagnostics. *Chemical Society Reviews*, 42(2):450–457, December 2012. Publisher: The Royal Society of Chemistry.

[12] World Health Organization. A guide to aid the selection of diagnostic tests, 2017. WHO, http://www.who.int/bulletin/volumes/95/9/16-187468/en/, Accessed 31/05/2021.

[13] Adaris M. López-Marzo and Arben Merkoçi. Paper-based sensors and assays: a success of the engineering design and the convergence of knowledge areas. *Lab on a Chip*, 16(17):3150–3176, August 2016. Publisher: The Royal Society of Chemistry.

[14] Amenu Desalegn and Tafeese Temesgen. Assessing the Contamination Level of water and Determination of the Major Sources of Contaminants among Rural Community of Dire Dawa Administrative Council. *International Journal of Advanced Research in Biological Sciences*, 7(9):74–83, 2020.

[15] Joyce Margaret Ekopai, Nathan Lubowa Musisi, Howard Onyuth, Benigna Gabriela Namara, and Celsus Sente. Determination of Bacterial Quality of Water in Randomly Selected Swimming Pools in Kampala City, Uganda. *New Journal of Science*, 2017:e1652598, June 2017. Publisher: Hindawi.

[16] Enric Calucho, Claudio Parolo, Lourdes Rivas, Ruslan Álvarez Diduk, and Arben Merkoçi. Chapter Ten - Nanoparticle-based lateral flow assays. In *Comprehensive Analytical Chemistry*, volume 89 of *Paper Based Sensors*, pages 313–359. Elsevier, January 2020.

[17] Claudio Parolo, Amadeo Sena-Torralba, José Francisco Bergua, Enric Calucho, Celia Fuentes-Chust, Liming Hu, Lourdes Rivas, Ruslan Álvarez Diduk, Emily P. Nguyen, Stefano Cinti, Daniel Quesada-González, and Arben Merkoçi. Tutorial: design and fabrication of nanoparticle-based lateral-flow immunoassays. *Nature Protocols*, 15(12):3788–3816, December 2020. Number: 12 Publisher: Nature Publishing Group.

[18] Michael Holzinger, Alan Le Goff, and Serge Cosnier. Nanomaterials for biosensing applications: a review. *Frontiers in Chemistry*, 2, 2014. Publisher: Frontiers.

[19] Daniel Quesada-González and Arben Merkoçi. Nanomaterial-based devices for point-of-care diagnostic applications. *Chemical Society Reviews*, 47(13):4697–4709, July 2018. Publisher: The Royal Society of Chemistry.

[20] Kevin J. Land, Debrah I. Boeras, Xiang-Sheng Chen, Andrew R. Ramsay, and Rosanna W. Peeling. REASSURED diagnostics to inform disease control strategies, strengthen health systems and improve patient outcomes. *Nature Microbiology*, 4(1):46–54, January 2019. Number: 1 Publisher: Nature Publishing Group.

[21] Katarzyna M. Koczula and Andrea Gallotta. Lateral flow assays. *Essays in Biochemistry*, 60(1):111–120, June 2016.

[22] Shizhi Qian and Haim H Bau. Analysis of lateral flow biodetectors: competitive format. *Analytical Biochemistry*, 326(2):211–224, March 2004.

[23] Tohid Mahmoudi, Miguel de la Guardia, and Behzad Baradaran. Lateral flow assays towards point-of-care cancer detection: A review of current progress and future trends. *TrAC Trends in Analytical Chemistry*, 125:115842, April 2020.

[24] Shima Dalirirad and Andrew J. Steckl. Aptamer-based lateral flow assay for point of care cortisol detection in sweat. *Sensors and Actuators B: Chemical*, 283:79–86, March 2019.

[25] Shima Dalirirad and Andrew J. Steckl. Lateral flow assay using aptamer-based sensing for on-site detection of dopamine in urine. *Analytical Biochemistry*, 596:113637, May 2020.

[26] Babacar Ngom, Yancheng Guo, Xiliang Wang, and Dingren Bi. Development and application of lateral flow test strip technology for detection of infectious agents and chemical contaminants: a review. *Analytical and Bioanalytical Chemistry*, 397(3):1113–1135, June 2010.

[27] Laxmana Naik, Rajan Sharma, Bimlesh Mann, Kiran Lata, Y. S. Rajput, and B. Surendra Nath. Rapid screening test for detection of oxytetracycline residues in milk using lateral flow assay. *Food Chemistry*, 219:85–92, March 2017.

[28] EMD Millipore Corporation. Rapid laterial flow test strips - considerations for product development, 2013.

[29] Lourdes Rivas, Mariana Medina-Sánchez, Alfredo de la Escosura-Muñiz, and Arben Merkoçi. Improving sensitivity of gold nanoparticle-based lateral flow assays by using wax-printed pillars as delay barriers of microfluidics. *Lab Chip*, 14, September 2014.

[30] Gisele Elias Nunes Pauli, Alfredo de la Escosura-Muñiz, Claudio Parolo, Ivan Helmuth Bechtold, and Arben Merkoçi. Lab-in-a-syringe using gold nanoparticles for rapid immunosensing of protein biomarkers. *Lab on a Chip*, 15(2):399–405, December 2014. Publisher: The Royal Society of Chemistry.

[31] Jitendra N. Tiwari, Rajanish N. Tiwari, and Kwang S. Kim. Zero-dimensional, one-dimensional, two-dimensional and three-dimensional nanostructured materials for advanced electrochemical energy devices. *Progress in Materials Science*, 57(4):724–803, May 2012.

[32] Adeyabeba Abera and Jin-Woo Choi. Quantitative lateral flow immunosensor using carbon nanotubes as label. *Analytical Methods*, 2(11):1819–1822, 2010.

[33] Wanwei Qiu, Kwaku Baryeh, Sunitha Takalkar, Wei Chen, and Guodong Liu. Carbon nanotube-based lateral flow immunoassay for ultrasensitive detection of proteins: application to the determination of IgG. *Microchimica Acta*, 186(7):436, June 2019.

[34] Yan Huang, Tingting Wu, Fang Wang, Kun Li, Lisheng Qian, Xueji Zhang, and Guodong Liu. Magnetized Carbon Nanotube Based Lateral Flow Immunoassay for Visual Detection of Complement Factor B. *Molecules*, 24(15):2759, January 2019.

[35] Li Yu, Peiwu Li, Xiaoxia Ding, and Qi Zhang. Graphene oxide and carboxylated graphene oxide: Viable two-dimensional nanolabels for lateral flow immunoassays. *Talanta*, 165:167–175, April 2017.

[36] P. Noguera, G. A. Posthuma-Trumpie, M. van Tuil, F. J. van der Wal, A. de Boer, A. P. H. A. Moers, and A. van Amerongen. Carbon nanoparticles in lateral flow methods to detect genes encoding virulence factors of Shiga toxin-producing Escherichia coli. *Analytical and Bioanalytical Chemistry*, 399(2):831–838, January 2011.

[37] Natpapas Wiriyachaiporn, Hathainan Sirikett, Weerakanya Maneeprakorn, and Tararaj Dharakul. Carbon nanotag based visual detection of influenza A virus by a lateral flow immunoassay. *Microchimica Acta*, 184(6):1827–1835, June 2017.

[38] Martina Blažková, Pavel Rauch, and Ladislav Fukal. Strip-based immunoassay for rapid detection of thiabendazole. *Biosensors and Bioelectronics*, 25(9):2122–2128, May 2010.

[39] G. J. van Dam, J. H. Wichers, T. M. Falcao Ferreira, D. Ghati, A. van Amerongen, and A. M. Deelder. Diagnosis of Schistosomiasis by Reagent Strip Test for Detection of Circulating Cathodic Antigen. *Journal of Clinical Microbiology*, 42(12):5458–5461, December 2004.

[40] P. J. F. Harris and S. C. Tsang. A simple technique for the synthesis of filled carbon nanoparticles. *Chemical Physics Letters*, 293(1):53–58, August 1998.

[41] Cheng Zheng, Xichang Wang, Ying Lu, and Yuan Liu. Rapid detection of fish major allergen parvalbumin using superparamagnetic nanoparticle-based lateral flow immunoassay. *Food Control*, 26(2):446–452, August 2012.

[42] Yohei Watanabe, Madiha S. Ibrahim, Yasuha Arai, Kazuyoshi Ikuta, and Yasuo Suzuki. A novel immunochromatographic system for easy-to-use detection of group 1 avian influenza viruses with acquired human-type receptor binding specificity. *Biosensors and Bioelectronics*, 65:211–219, March 2015.

[43] Xun Mao, Wei Wang, and Ting E. Du. Dry-reagent nucleic acid biosensor based on blue dye doped latex beads and lateral flow strip. *Talanta*, 114:248–253, September 2013.

[44] Elisângela M. Linares, Lauro T. Kubota, Jens Michaelis, and Stefan Thalhammer. Enhancement of the detection limit for lateral flow immunoassays: Evaluation and comparison of bioconjugates. *Journal of Immunological Methods*, 375(1):264–270, January 2012.

[45] David J. You, Tu San Park, and Jeong-Yeol Yoon. Cell-phone-based measurement of TSH using Mie scatter optimized lateral flow assays. *Biosensors and Bioelectronics*, 40(1):180–185, February 2013.

[46] Nurul Hanun Ahmad Raston, Van-Thuan Nguyen, and Man Bock Gu. A new lateral flow strip assay (LFSA) using a pair of aptamers for the detection of Vaspin. *Biosensors and Bioelectronics*, 93:21–25, 2017.

[47] Niko Hildebrandt. Biofunctional Quantum Dots: Controlled Conjugation for Multiplexed Biosensors. *ACS Nano*, 5(7):5286–5290, July 2011. Publisher: American Chemical Society.

[48] O. D. D. Couto Jr., J. Puebla, E. A. Chekhovich, I. J. Luxmoore, C. J. Elliott, N. Babazadeh, M. S. Skolnick, A. I. Tartakovskii, and A. B. Krysa. Charge control in InP/GaInP single quantum dots embedded in Schottky diodes. *Physical Review B*, 84(12):125301, September 2011.

[49] Wikipedia contributors. Exciton, March 2021. Wikipedia, https://en.wikipedia.org/w/index.php?title=Exciton&oldid=1011092145, Accessed: 04/04/2021.

[50] W. Russ Algar, Kimihiro Susumu, James B. Delehanty, and Igor L. Medintz. Semiconductor Quantum Dots in Bioanalysis: Crossing the Valley of Death. *Analytical Chemistry*, 83(23):8826–8837, December 2011.

[51] Oleg D. Neikov and Nikolay A. Yefimov. Chapter 9 - Nanopowders. In Oleg D. Neikov, Stanislav S. Naboychenko, and Nikolay A. Yefimov, editors, *Handbook of Non-Ferrous Metal Powders (Second Edition)*, pages 271–311. Elsevier, Oxford, January 2019.

[52] Muhammad Safwan Zaini, Josephine Ying Chyi Liew, Shahrul Ainliah Alang Ahmad, Abdul Rahman Mohmad, and Mazliana Ahmad Kamarudin. Quantum Confinement

Effect and Photoenhancement of Photoluminescence of PbS and PbS/MnS Quantum Dots. *Applied Sciences*, 10(18):6282, January 2020. Number: 18 Publisher: Multidisciplinary Digital Publishing Institute.

[53] Yalong Bai, Chunyuan Tian, Xinlin Wei, Yuanfeng Wang, Dapeng Wang, and Xianming Shi. A sensitive lateral flow test strip based on silica nanoparticle/CdTe quantum dot composite reporter probes. *RSC Advances*, 2(5):1778–1781, February 2012.

[54] Markus Haase and Helmut Schäfer. Upconverting Nanoparticles. *Angewandte Chemie International Edition*, 50(26):5808–5829, 2011.

[55] Muhsin Ali, Memoon Sajid, Muhammad Asad Ullah Khalid, Soo Wan Kim, Jong Hwan Lim, Dongeun Huh, and Kyung Hyun Choi. A fluorescent lateral flow biosensor for the quantitative detection of Vaspin using upconverting nanoparticles. *Spectrochimica Acta Part A: Molecular and Biomolecular Spectroscopy*, 226:117610, February 2020.

[56] Gisela Ruiz-Vega, Maria Kitsara, Miguel Aller Pellitero, Eva Baldrich, and F. Javier del Campo. Electrochemical Lateral Flow Devices: Towards Rapid Immunomagnetic Assays. *ChemElectroChem*, 4(4):880–889, 2017.

[57] Tohid Mahmoudi, Miguel de la Guardia, Behnaz Shirdel, Ahad Mokhtarzadeh, and Behzad Baradaran. Recent advancements in structural improvements of lateral flow assays towards point-of-care testing. *TrAC Trends in Analytical Chemistry*, 116:13–30, July 2019.

[58] Zarini Muhammad-Tahir and Evangelyn C. Alocilja. A conductometric biosensor for biosecurity. *Biosensors and Bioelectronics*, 18(5):813–819, May 2003.

[59] Prima Dewi Sinawang, Varun Rai, Rodica E. Ionescu, and Robert S. Marks. Electrochemical lateral flow immunosensor for detection and quantification of dengue NS1 protein. *Biosensors and Bioelectronics*, 77:400–408, March 2016.

[60] Olivier Lazcka, F. Javier Del Campo, and F. Xavier Muñoz. Pathogen detection: A perspective of traditional methods and biosensors. *Biosensors and Bioelectronics*, 22(7):1205–1217, February 2007.

[61] Amanda Moyano, Esther Serrano-Pertierra, María Salvador, José Carlos Martínez-García, Montserrat Rivas, and M. Carmen Blanco-López. Magnetic Lateral Flow Immunoassays. *Diagnostics*, 10(5):288, May 2020. Number: 5 Publisher: Multidisciplinary Digital Publishing Institute.

[62] Alexandr E. Urusov, Anatoly V. Zherdev, and Boris B. Dzantiev. Towards Lateral Flow Quantitative Assays: Detection Approaches. *Biosensors*, 9(3), July 2019.

[63] Alexander O. Govorov and Hugh H. Richardson. Generating heat with metal nanoparticles. *Nano Today*, 2(1):30–38, February 2007.

[64] Zhenpeng Qin, Warren C. W. Chan, David R. Boulware, Taner Akkin, Elissa K. Butler, and John C. Bischof. Significantly Improved Analytical Sensitivity of Lateral Flow Immunoassays by Using Thermal Contrast. *Angewandte Chemie International Edition*, 51(18):4358–4361, 2012.

[65] Xiaolin Huang, Zoraida P. Aguilar, Hengyi Xu, Weihua Lai, and Yonghua Xiong. Membrane-based lateral flow immunochromatographic strip with nanoparticles as reporters for detection: A review. *Biosensors and Bioelectronics*, 75:166–180, January 2016.

[66] Raluca M. Fratila, Scott G. Mitchell, Pablo del Pino, Valeria Grazu, and Jesús M. de la Fuente. Strategies for the Biofunctionalization of Gold and Iron Oxide Nanoparticles. *Langmuir*, 30(50):15057–15071, December 2014.

[67] Nguyen T. K. Thanh and Luke A. W. Green. Functionalisation of nanoparticles for biomedical applications. *Nano Today*, 5(3):213–230, June 2010.

[68] Nandanan Erathodiyil and Jackie Y. Ying. Functionalization of inorganic nanoparticles for bioimaging applications. *Accounts of Chemical Research*, 44(10):925–935, October 2011.

[69] Tommy Haynes, Ovidiu Ersen, Vincent Dubois, Didier Desmecht, Keizo Nakagawa, and Sophie Hermans. Protecting a Pd/CB catalyst by a mesoporous silica layer. *Applied Catalysis B: Environmental*, 241:196–204, February 2019.

[70] Claudio Parolo, Alfredo de la Escosura-Muñiz, Ester Polo, Valeria Grazú, Jesús M. de la Fuente, and Arben Merkoçi. Design, Preparation, and Evaluation of a Fixed-Orientation Antibody/Gold-Nanoparticle Conjugate as an Immunosensing Label. *ACS Applied Materials & Interfaces*, 5(21):10753–10759, November 2013. Publisher: American Chemical Society.

[71] Veeradasan Perumal and Uda Hashim. Advances in biosensors: Principle, architecture and applications. *Journal of Applied Biomedicine*, 12(1):1–15, January 2014.

[72] Jeremy M. Fowler, Danny K. Y. Wong, H. Brian Halsall, and William R. Heineman. Recent developments in electrochemical immunoassays and immunosensors. *Electrochemical Sensors, Biosensors and their Biomedical Applications*, pages 115–143, 2008.

[73] Van-Thuan Nguyen, Seungri Song, Seungkyung Park, and Chulmin Joo. Recent advances in high-sensitivity detection methods for paper-based lateral-flow assay. *Biosensors and Bioelectronics*, 152:112015, March 2020.

[74] Mir Hadi Jazayeri, Hamed Amani, Ali Akbar Pourfatollah, Hamidreza Pazoki-Toroudi, and Bijan Sedighimoghaddam. Various methods of gold nanoparticles (GNPs) conjugation to antibodies. *Sensing and Bio-Sensing Research*, 9:17–22, July 2016.

[75] David A. Giljohann, Dwight S. Seferos, Weston L. Daniel, Matthew D. Massich, Pinal C. Patel, and Chad A. Mirkin. Gold Nanoparticles for Biology and Medicine. *Angewandte Chemie International Edition*, 49(19):3280–3294, 2010.

[76] Xun Mao, Yunqing Ma, Aiguo Zhang, Lurong Zhang, Lingwen Zeng, and Guodong Liu. Disposable Nucleic Acid Biosensors Based on Gold Nanoparticle Probes and Lateral Flow Strip. *Analytical Chemistry*, 81(4):1660–1668, February 2009. Publisher: American Chemical Society.

[77] Somayyeh Poshtiban, Muhammad Afzal Javed, Denis Arutyunov, Amit Singh, Graham Banting, Christine M. Szymanski, and Stephane Evoy. Phage receptor binding protein-based magnetic enrichment method as an aid for real time PCR detection of foodborne bacteria. *The Analyst*, 138(19):5619–5626, October 2013.

[78] Elif Burcu Bahadır and Mustafa Kemal Sezgintürk. Lateral flow assays: Principles, designs and labels. *TrAC Trends in Analytical Chemistry*, 82:286–306, September 2016.

[79] Andreas Elsaesser and C. Vyvyan Howard. Toxicology of nanoparticles. *Advanced Drug Delivery Reviews*, 64(2):129–137, February 2012.

[80] Gang Liu, Jinhao Gao, Hua Ai, and Xiaoyuan Chen. Applications and Potential Toxicity of Magnetic Iron Oxide Nanoparticles. *Small*, 9(9-10):1533–1545, 2013.

[81] L. Harivardhan Reddy, José L. Arias, Julien Nicolas, and Patrick Couvreur. Magnetic Nanoparticles: Design and Characterization, Toxicity and Biocompatibility, Pharmaceutical and Biomedical Applications. *Chemical Reviews*, 112(11):5818–5878, November 2012. Publisher: American Chemical Society.

[82] Yan-Peng Jia, Bu-Yun Ma, Xia-Wei Wei, and Zhi-Yong Qian. The in vitro and in vivo toxicity of gold nanoparticles. *Chinese Chemical Letters*, 28(4):691–702, April 2017.

[83] Ilaria Fratoddi, Iole Venditti, Cesare Cametti, and Maria Vittoria Russo. How toxic are gold nanoparticles? The state-of-the-art. *Nano Research*, 8(6):1771–1799, June 2015.

[84] Jiaqi Dong, Paul L. Carpinone, Georgios Pyrgiotakis, Philip Demokritou, and Brij M. Moudgil. Synthesis of Precision Gold Nanoparticles Using Turkevich Method. *Kona : powder science and technology in Japan*, 37:224–232, January 2020.

[85] John Turkevich, Peter Cooper Stevenson, and James Hillier. A study of the nucleation and growth processes in the synthesis of colloidal gold. *Discussions of the Faraday Society*, 11:55, 1951.

[86] Krishnendu Saha, Sarit S. Agasti, Chaekyu Kim, Xiaoning Li, and Vincent M. Rotello. Gold Nanoparticles in Chemical and Biological Sensing. *Chemical reviews*, 112(5):2739–2779, May 2012.

[87] Han-Wen Cheng, Zakiya R. Skeete, and Elizabeth R. Crew. Chapter 2 - Synthesis of Gold Nanoparticles. In *Comprehensive Analytical Chemistry*, volume 66 of *Gold Nanoparticles in Analytical Chemistry*, pages 37–79. Elsevier, January 2014.

[88] Asep Rohiman, Isa Anshori, Akhmadi Surawijaya, and Irman Idris. Study of Colloidal Gold Synthesis Using Turkevich Method. *AIP Conference Proceedings*, 1415:39–42, December 2011.

[89] Mathias Brust, Merryl Walker, Donald Bethell, David J. Schiffrin, and Robin Whyman. Synthesis of thiol-derivatised gold nanoparticles in a two-phase Liquid–Liquid system. *Journal of the Chemical Society, Chemical Communications*, (7):801–802, January 1994.

[90] M. K. Chow and C. F. Zukoski. Gold Sol Formation Mechanisms: Role of Colloidal Stability. *Journal of Colloid and Interface Science*, 165(1):97–109, June 1994.

[91] G. Frens. Controlled Nucleation for the Regulation of the Particle Size in Monodisperse Gold Suspensions. *Nature Physical Science*, 241(105):20–22, January 1973.

[92] NanoHybrids. Antibody Conjugation for Gold Nanoparticles. Nanohybrids, https://nanohybrids.net/pages/antibody-conjugated-gold-nanoparticles, Accessed: 08/04/2021.

[93] Paula Ciaurriz, Fátima Fernández, Edurne Tellechea, Jose F. Moran, and Aaron C. Asensio. Comparison of four functionalization methods of gold nanoparticles for enhancing the enzyme-linked immunosorbent assay (ELISA). *Beilstein Journal of Nanotechnology*, 8(1):244–253, January 2017.

[94] B. Devika Chithrani, Arezou A. Ghazani, and Warren C. W. Chan. Determining the Size and Shape Dependence of Gold Nanoparticle Uptake into Mammalian Cells. *Nano Letters*, 6(4):662–668, April 2006.

[95] Pier Paolo Pompa, Giuseppe Vecchio, Antonio Galeone, Virgilio Brunetti, Stefania Sabella, Gabriele Maiorano, Andrea Falqui, Giovanni Bertoni, and Roberto Cingolani. In Vivo toxicity assessment of gold nanoparticles in Drosophila melanogaster. *Nano Research*, 4(4):405–413, April 2011.

[96] Yu-Shiun Chen, Yao-Ching Hung, Ian Liau, and G. Steve Huang. Assessment of the In Vivo Toxicity of Gold Nanoparticles. *Nanoscale Research Letters*, 4(8):858, May 2009.

[97] Na Li, Pengxiang Zhao, and Didier Astruc. Anisotropic Gold Nanoparticles: Synthesis, Properties, Applications, and Toxicity. *Angewandte Chemie International Edition*, 53(7):1756–1789, 2014.

[98] Christopher Pöhlmann, Irina Dieser, and Mathias Sprinzl. A lateral flow assay for identification of Escherichia coli by ribosomal RNA hybridisation. *Analyst*, 139(5):1063–1071, 2014. Publisher: Royal Society of Chemistry.

[99] Wenbin Wang, Liqiang Liu, Shanshan Song, Liguang Xu, Hua Kuang, Jianping Zhu, and Chuanlai Xu. Identification and quantification of eight Listeria monocytogene serotypes from Listeria spp. using a gold nanoparticle-based lateral flow assay. *Microchimica Acta*, 184(3):715–724, March 2017.

[100] Adaris M. López_Marzo, Josefina Pons, Diane A. Blake, and Arben Merkoçi. High sensitive gold-nanoparticle based lateral flow Immunodevice for Cd2+ detection in drinking waters. *Biosensors and Bioelectronics*, 47:190–198, September 2013.

[101] Debapriya Mazumdar, Juewen Liu, Geng Lu, Juanzuo Zhou, and Yi Lu. Easy-to-use dipstick tests for detection of lead in paints using non-cross-linked gold nanoparticle–DNAzyme conjugates. *Chemical Communications*, 46(9):1416–1418, February 2010. Publisher: The Royal Society of Chemistry.

[102] Seyed-Fakhreddin Torabi and Yi Lu. Small-molecule diagnostics based on functional DNA nanotechnology: a dipstick test for mercury. *Faraday Discussions*, 149(0):125–135, July 2013. Publisher: The Royal Society of Chemistry.

[103] Zhiyuan Fang, Jing Huang, Puchang Lie, Zhuo Xiao, Chuanyan Ouyang, Qing Wu, Yixing Wu, Guodong Liu, and Lingwen Zeng. Lateral flow nucleic acid biosensor for Cu2+ detection in aqueous solution with high sensitivity and selectivity. *Chemical Communications*, 46(47):9043–9045, November 2010.

[104] Daniel Quesada-González, Grace A. Jairo, Robert C. Blake, Diane A. Blake, and Arben Merkoçi. Uranium (VI) detection in groundwater using a gold nanoparticle/paper-based lateral flow device. *Scientific Reports*, 8(1):16157, November 2018. Number: 1 Publisher: Nature Publishing Group.

[105] Jyoti Singh, Shivesh Sharma, and Seema Nara. Evaluation of gold nanoparticle based lateral flow assays for diagnosis of enterobacteriaceae members in food and water. *Food Chemistry*, 170:470–483, March 2015.

[106] Dong Yang, Jianzhong Ma, Qinlu Zhang, Ningning Li, Jiangcun Yang, Paul Ananda Raju, Mingli Peng, Yanling Luo, Wenli Hui, Chao Chen, and Yali Cui. Polyelectrolyte-Coated Gold Magnetic Nanoparticles for Immunoassay Development: Toward Point of Care Diagnostics for Syphilis Screening. *Analytical Chemistry*, 85(14):6688–6695, July 2013. Publisher: American Chemical Society.

[107] Ria Lassaunière, Anders Frische, Zitta B. Harboe, Alex C. Y. Nielsen, Anders Fomsgaard, Karen A. Krogfelt, and Charlotte S. Jørgensen. Evaluation of nine commercial SARS-CoV-2 immunoassays. *medRxiv*, April 2020. Publisher: Cold Spring Harbor Laboratory Press.

[108] Dong Hwan Choi, Seok Ki Lee, Young Kyoung Oh, Byeong Woo Bae, Sung Dong Lee, Sanghyo Kim, Yong-Beom Shin, and Min-Gon Kim. A dual gold nanoparticle conjugate-based lateral flow assay (LFA) method for the analysis of troponin I. *Biosensors and Bioelectronics*, 25(8):1999–2002, April 2010.

[109] Claudio Parolo, Alfredo de la Escosura-Muñiz, and Arben Merkoçi. Enhanced lateral flow immunoassay using gold nanoparticles loaded with enzymes. *Biosensors and Bioelectronics*, 40(1):412–416, February 2013.

[110] Wikipedia contributors. Magnetic domain, January 2021. Wikipedia, https://en.wikipedia.org/w/index.php?title=Magnetic_domain&oldid=999177662, Accessed: 09/04/2021.

[111] Wikipedia contributors. Magnetic moment, February 2021. Wikipedia, https://en.wikipedia.org/w/index.php?title=Magnetic_moment&oldid=1007067719, Accessed: 09/04/2021.

[112] Wikipedia contributors. Magnetic dipole, February 2021. Wikipedia, https://en.wikipedia.org/w/index.php?title=Magnetic_dipole&oldid=1006126033, Accessed: 09/04/2021.

[113] The Editors of Encyclopaedia. Magnetic dipole | physics, February 2019. Encyclopedia Britannica, https://www.britannica.com/science/magnetic-dipole, Accessed: 09/04/2021.

[114] U. Jeong, X. Teng, Y. Wang, H. Yang, and Y. Xia. Superparamagnetic Colloids: Controlled Synthesis and Niche Applications. *Advanced Materials*, 19(1):33–60, 2007.

[115] Tomas Scepka. Noninvasive control of magnetic state in ferromagnetic nanodots by Hall probe magnetometry, March 2016. PhD Thesis, Slovak University of Technology in Bratislava, Faculty of Electrical Engineering and Information Technology.

[116] Yi-Ting Chen, Arati G. Kolhatkar, Oussama Zenasni, Shoujun Xu, and T. Randall Lee. Biosensing Using Magnetic Particle Detection Techniques. *Sensors*, 17(10):2300, October 2017.

[117] An-Hui Lu, E. L. Salabas, and Ferdi Schüth. Magnetic Nanoparticles: Synthesis, Protection, Functionalization, and Application. *Angewandte Chemie International Edition*, 46(8):1222–1244, 2007.

[118] Wei Wu, Quanguo He, and Changzhong Jiang. Magnetic Iron Oxide Nanoparticles: Synthesis and Surface Functionalization Strategies. *Nanoscale Research Letters*, 3(11):397–415, October 2008.

[119] Kinga Mylkie, Paweł Nowak, Patryk Rybczyński, and Marta Ziegler-Borowska. Polymer-Coated Magnetite Nanoparticles for Protein Immobilization. *Materials*, 14:248, January 2021.

[120] Ahmed Al-Alawy, Entisar Alabodi, and Raya Kadhim. Synthesis and Characterization of Magnetic Iron Oxide Nanoparticles by Co-Precipitation Method at Different Conditions. *Journal of Engineering*, 24:60, 2018.

[121] Hong Deng, Xiaolin Li, Qing Peng, Xun Wang, Jinping Chen, and Yadong Li. Monodisperse magnetic single-crystal ferrite microspheres. *Angewandte Chemie (International Ed. in English)*, 44(18):2782–2785, April 2005.

[122] Ionela Andreea Neacşu, Adrian Ionuţ Nicoară, Otilia Ruxandra Vasile, and Bogdan Ştefan Vasile. Chapter 9 - Inorganic micro- and nanostructured implants for tissue engineering. In Alexandru Mihai Grumezescu, editor, *Nanobiomaterials in Hard Tissue Engineering*, pages 271–295. William Andrew Publishing, January 2016.

[123] Wikipedia contributors. Sol–gel process, March 2021. Wikipedia, https://en.wikipedia.org/w/index.php?title=Sol%E2%80%93gel_process&oldid=1012198445, Accessed: 10/04/2021.

[124] Chuanyan Li, Chao Ma, Fang Wang, Zhijiang Xi, Zhifei Wang, Yan Deng, and Nongyue He. Preparation and Biomedical Applications of Core–Shell Silica/Magnetic Nanoparticle Composites. *Journal of Nanoscience and Nanotechnology*, 12(4):2964–2972, April 2012.

[125] Nazila Eyvazzadeh, Ali Shakeri-Zadeh, Reza Fekrazad, Elahe Amini, Habib Ghaznavi, and S. Kamran Kamrava. Gold-coated magnetic nanoparticle as a nanotheranostic agent for magnetic resonance imaging and photothermal therapy of cancer. *Lasers in Medical Science*, 32(7):1469–1477, September 2017.

[126] Jeongin Hwang, Donghoon Kwon, Sanghee Lee, and Sangmin Jeon. Detection of Salmonella bacteria in milk using gold-coated magnetic nanoparticle clusters and lateral flow filters. *RSC Advances*, 6(54):48445–48448, 2016. Publisher: Royal Society of Chemistry.

[127] Pratim Biswas and Chang-Yu Wu. Nanoparticles and the Environment. *Journal of the Air & Waste Management Association*, 55(6):708–746, June 2005.

[128] Hanna L. Karlsson, Johanna Gustafsson, Pontus Cronholm, and Lennart Möller. Size-dependent toxicity of metal oxide particles—A comparison between nano- and micrometer size. *Toxicology Letters*, 188(2):112–118, July 2009.

[129] Ori Baber, Myoseon Jang, David Barber, and Kevin Powers. Amorphous silica coatings on magnetic nanoparticles enhance stability and reduce toxicity to in vitro BEAS-2B cells. *Inhalation Toxicology*, 23(9):532–543, August 2011.

[130] Daofeng Liu, Yanmei Huang, Shuying Wang, Kun Liu, Minghui Chen, Yonghua Xiong, Wanchun Yang, and Weihua Lai. A modified lateral flow immunoassay for the detection of trace aflatoxin M1 based on immunomagnetic nanobeads with different antibody concentrations. *Food Control*, 51:218–224, May 2015.

[131] Kristin Taton, Diane Johnson, Patrick Guire, Erik Lange, and Mark Tondra. Lateral flow immunoassay using magnetoresistive sensors. *Journal of Magnetism and Magnetic Materials*, 321(10):1679–1682, May 2009.

[132] Alexey V. Orlov, Vera A. Bragina, Maxim P. Nikitin, and Petr I. Nikitin. Rapid dry-reagent immunomagnetic biosensing platform based on volumetric detection of nanoparticles on 3D structures. *Biosensors and Bioelectronics*, 79:423–429, May 2016.

[133] C. Marquina, J. M. de Teresa, D. Serrate, J. Marzo, F. A. Cardoso, D. Saurel, S. Cardoso, P. P. Freitas, and M. R. Ibarra. GMR sensors and magnetic nanoparticles for immuno-chromatographic assays. *Journal of Magnetism and Magnetic Materials*, 324(21):3495–3498, October 2012.

[134] Taro Yonekita, Ryuji Ohtsuki, Eri Hojo, Naoki Morishita, Takashi Matsumoto, Tomoyasu Aizawa, and Fumiki Morimatsu. Development of a novel multiplex lateral flow assay using an antimicrobial peptide for the detection of Shiga toxin-producing Escherichia coli. *Journal of Microbiological Methods*, 93(3):251–256, June 2013.

[135] Chen-zhong Li, Katherine Vandenberg, Shradha Prabhulkar, Xuena Zhu, Lisa Schneper, Kalai Methee, Charles J. Rosser, and Eugenio Almeide. Paper based point-of-care testing disc for multiplex whole cell bacteria analysis. *Biosensors and Bioelectronics*, 26(11):4342–4348, July 2011.

[136] Erin M. Fenton, Monica R. Mascarenas, Gabriel P. López, and Scott S. Sibbett. Multiplex Lateral-Flow Test Strips Fabricated by Two-Dimensional Shaping. *ACS Applied Materials & Interfaces*, 1(1):124–129, January 2009.

[137] Yong Zhao, Haoran Wang, Pingping Zhang, Chongyun Sun, Xiaochen Wang, Xinrui Wang, Ruifu Yang, Chengbin Wang, and Lei Zhou. Rapid multiplex detection of 10 foodborne pathogens with an up-converting phosphor technology-based 10-channel lateral flow assay. *Scientific Reports*, 6(1):21342, February 2016. Number: 1 Publisher: Nature Publishing Group.

[138] Laura Anfossi, Fabio Di Nardo, Simone Cavalera, Cristina Giovannoli, and Claudio Baggiani. Multiplex Lateral Flow Immunoassay: An Overview of Strategies towards High-throughput Point-of-Need Testing. *Biosensors*, 9(1):2, March 2019.

[139] Francisco Mederos-Henry, Benoît P. Pichon, Yzaora Tchuitio Yagang, Arnaud Delcorte, Christian Bailly, Isabelle Huynen, and Sophie Hermans. Decoration of nanocarbon solids with magnetite nanoparticles: towards microwave metamaterial absorbers. *Journal of Materials Chemistry C*, 4(15):3290–3303, April 2016. Publisher: The Royal Society of Chemistry.

[140] Zhichuan Xu, Chengmin Shen, Yanglong Hou, Hongjun Gao, and Shouheng Sun. Oleylamine as Both Reducing Agent and Stabilizer in a Facile Synthesis of Magnetite Nanoparticles. *Chemistry of Materials*, 21(9):1778–1780, May 2009. Publisher: American Chemical Society.

[141] Shouhu Xuan, Yi-Xiang J. Wang, Jimmy C. Yu, and Ken Cham-Fai Leung. Tuning the Grain Size and Particle Size of Superparamagnetic Fe3O4 Microparticles. *Chemistry of Materials*, 21(21):5079–5087, November 2009. Publisher: American Chemical Society.

[142] Meizhen Gao. Synthesis and Characterization of Superparamagnetic Fe3O4@SiO2 Core-Shell Composite Nanoparticles. *World Journal of Condensed Matter Physics*, 1, January 2011.

[143] Jinmyung Cha, Ping Cui, and Jin-Kyu Lee. A simple method to synthesize multifunctional silica nanocomposites, NPs@SiO2, using polyvinylpyrrolidone (PVP) as a mediator. *Journal of Materials Chemistry*, 20(26):5533–5537, June 2010.

[144] Odile Crahay. Towards the design of a paper-based microfluidic sensor for water quality monitoring and comparative life cycle assessment, 2020. Master Thesis, Ecole polytechnique de Louvain, Université catholique de Louvain.

[145] Boris N. Khlebtsov, Roman S. Tumskiy, Andrey M. Burov, Timofey E. Pylaev, and Nikolai G. Khlebtsov. Quantifying the Numbers of Gold Nanoparticles in the Test Zone of Lateral Flow Immunoassay Strips. *ACS Applied Nano Materials*, 2(8):5020–5028, August 2019. Publisher: American Chemical Society.

[146] JEOL. Scanning Electron Microscopes (SEM) | Introduction to JEOL Products | JEOL Ltd. JEOL, https://www.jeol.co.jp/en/science/sem.html, Accessed: 10/05/2021.

[147] Jörgen Bergström. 2 - Experimental Characterization Techniques. In *Mechanics of Solid Polymers*, pages 19–114. William Andrew Publishing, January 2015.

[148] Brian J. Ford, David C. Joy, and Savile Bradbury. Transmission electron microscope, September 2019. Encyclopedia Britannica, https://www.britannica.com/technology/transmission-electron-microscope, Accessed: 11/05/2021.

[149] LS Instruments. Dynamic Light Scattering, 2021. https://lsinstruments.ch/en/theory/dynamic-light-scattering-dls/introduction, Accessed: 10/05/2021.

[150] Malvern Panalytical. Zetasizer Pro and Zetasizer Ultra: advance with confidence, 2018.

[151] Zhebo Chen, Todd G. Deutsch, Huyen N. Dinh, Kazunari Domen, and Keith Emery. UV-Vis Spectroscopy. In *Photoelectrochemical Water Splitting: Standards, Experimental Methods, and Protocols*, SpringerBriefs in Energy, pages 49–62. Springer, New York, NY, 2013.

[152] Wolfgang Ensinger and Wolfgang Dönner. Advanced Characterization Methods of Materials Science, Chap.1: UV-vis photometry, Technische Universität Darmstadt, 2020.

[153] Shimadzu Scientific Instruments. UV-Vis Frequently Asked Questions - Instrument Design, September 2019. Shimadzu, https://www.ssi.shimadzu.com/, Accessed: 10/05/2021.

[154] Neelakshi Gohain. Studies on the structure and function of phenazine modifying enzymes PhzM and PhzS involved in the biosynthesis of pyocyanin. January 2009.

[155] Liberal Dictionary. Scanning electron microscope, November 2018. https://www.tekportal.net/scanning-electron-microscope/, Accessed: 11/05/2021.

[156] Wikipedia contributors. Energy-dispersive X-ray spectroscopy, May 2021. Wikipedia, https://en.wikipedia.org/w/index.php?title=Energy-dispersive_X-ray_spectroscopy&oldid=1022014136, Accessed: 10/05/2021.

[157] Wikipedia contributors. X-ray crystallography, May 2021. Wikipedia, https://en.wikipedia.org/w/index.php?title=X-ray_crystallography&oldid=1021870333, Accessed: 07-05-2021.

[158] Kaliyamoorthy Venkatesan, Dhanakotti Rajan Babu, Mane Prabhu Kavya Bai, Ravi Supriya, Radhakrishnan Vidya, Saminathan Madeswaran, Pandurangan Anandan, Mukannan Arivanandhan, and Yasuhiro Hayakawa. Structural and magnetic properties of cobalt-doped iron oxide nanoparticles prepared by solution combustion method for biomedical applications. *International Journal of Nanomedicine*, 10(Suppl 1):189–198, October 2015.

[159] Li Shi, Eric Buhler, François Boué, and Florent Carn. How does the size of gold nanoparticles depend on citrate to gold ratio in Turkevich synthesis? Final answer to a debated question. *Journal of Colloid and Interface Science*, 492:191–198, April 2017.

[160] Kara Zabetakis and William E. Ghann. Sanjeev Kumar & Marie-Christine Daniel. *Gold Bull*, 45:203–211., 2012.

[161] Daniel Andreescu, Tapan Kumar Sau, and Dan V. Goia. Stabilizer-free nanosized gold sols. *Journal of Colloid and Interface Science*, 298(2):742–751, June 2006.

[162] Stefanos Mourdikoudis and Luis M. Liz-Marzán. Oleylamine in Nanoparticle Synthesis. *Chemistry of Materials*, 25(9):1465–1476, May 2013. Publisher: American Chemical Society.

[163] Ming Zhang, Brian L. Cushing, and Charles J. O'Connor. Synthesis and characterization of monodisperse ultra-thin silica-coated magnetic nanoparticles. *Nanotechnology*, 19(8):085601, February 2008. Publisher: IOP Publishing.

[164] Massimo Manuelli, Silvia Fallarini, Grazia Lombardi, Claudio Sangregorio, Cristina Nativi, and Barbara Richichi. Iron oxide superparamagnetic nanoparticles conjugated with a conformationally blocked alpha-Tn antigen mimetic for macrophage activation. *Nanoscale*, 6(13):7643–7655, June 2014. Publisher: The Royal Society of Chemistry.

[165] Robert Pązik, Anna Lewińska, Jagoda Adamczyk-Grochala, Magdalena Kulpa-Greszta, Patrycja Kłoda, Anna Tomaszewska, Andrzej Dziedzic, Grzegorz Litwienienko, Maciej Noga, Daniel Sikora, and Maciej Wnuk. Energy Conversion and Biocompatibility of Surface Functionalized Magnetite Nanoparticles with Phosphonic Moieties. *The Journal of Physical Chemistry. B*, 124(24):4931–4948, June 2020.

[166] Khatereh Faaliyan, Hassan Abdoos, Ehsan Borhani, and Seyyed Afghahi. Magnetite-silica nanoparticles with core-shell structure: single-step synthesis, characterization and magnetic behavior. *Journal of Sol-Gel Science and Technology*, 88, December 2018.

[167] Dae-Won Lee, Hira Fatima, and Kyo-Seon Kim. Preparation of Silica Coated Magnetic Nanoparticles for Bioseparation. *Journal of Nanoscience and Nanotechnology*, 18:1414–1418, February 2018.

[168] Won-Yeop Rho, Hyung-Mo Kim, San Kyeong, Yoo-Lee Kang, Dong-Hyuk Kim, Homan Kang, Cheolhwan Jeong, Dong-Eun Kim, Yoon-Sik Lee, and Bong-Hyun Jun. Facile synthesis of monodispersed silica-coated magnetic nanoparticles. *Journal of Industrial and Engineering Chemistry*, 20(5):2646–2649, September 2014.

[169] X. Xu, C. Deng, M. Gao, W. Yu, P. Yang, and X. Zhang. Synthesis of Magnetic Microspheres with Immobilized Metal Ions for Enrichment and Direct Determination of Phosphopeptides by Matrix-Assisted Laser Desorption Ionization Mass Spectrometry. *Advanced Materials*, 18(24):3289–3293, 2006.

[170] Yuri A. Barnakov, Minghui H. Yu, and Zeev Rosenzweig. Manipulation of the Magnetic Properties of Magnetite−Silica Nanocomposite Materials by Controlled Stober Synthesis. *Langmuir*, 21(16):7524–7527, August 2005.

[171] Yanqing An, Miao Chen, Qunji Xue, and Weimin Liu. Preparation and self-assembly of carboxylic acid-functionalized silica. *Journal of Colloid and Interface Science*, 311(2):507–513, 2007.

[172] Anthony J. Di Pasqua, Richard E. Mishler, Yan-Li Ship, James C. Dabrowiak, and Tewodros Asefa. Preparation of antibody-conjugated gold nanoparticles. *Materials Letters*, 63(21):1876–1879, August 2009.

[173] Carmen Vogt, Muhammet S. Toprak, Mamoun Muhammed, Sophie Laurent, Jean-Luc Bridot, and Robert N. Müller. High quality and tuneable silica shell–magnetic core nanoparticles. *Journal of Nanoparticle Research*, 12(4):1137–1147, May 2010.

[174] Vaishnavi Sureshkumar, Kiruba Daniel, Sivakumar Muthusamy, and Ruckmani Kandasamy. Fabrication of chitosan–magnetite nanocomposite strip for chromium removal. *Applied Nanoscience*, 6, March 2015.

[175] Massimo Pasquale, Elena S. Olivetti, Marco Coïsson, Paola Rizzi, and Giorgio Bertotti. Ferromagnetic resonance and superparamagnetic behavior of iron oxide nanoparticles injected in porous anodic alumina. *Journal of Applied Physics*, 103(7):07D527, March 2008. Publisher: American Institute of Physics.

[176] nanoComposix. Mesoporous Silica Nanoparticles, 2021. nanoComposix, https://nanocomposix.com/collections/material-mesoporous-silica, Accessed: 29/05/2021.

[177] Verónica Salgueiriño-Maceira, Miguel A. Correa-Duarte, Michael Farle, Arturo López-Quintela, Karl Sieradzki, and Rodolfo Diaz. Bifunctional Gold-Coated Magnetic Silica Spheres. *Chemistry of Materials*, 18(11):2701–2706, May 2006. Publisher: American Chemical Society.

[178] Masahiro Hotta, Miyuki Hayashi, and Kazuhiro Nagata. High Temperature Measurement of Complex Permittivity and Permeability of Fe_3O_4 Powders in the Frequency Range of 0.2 to 13.5 GHz. *ISIJ International*, 51(3):491–497, 2011.

[179] Scott MacKay, Gaser N. Abdelrasoul, Marcus Tamura, Donghai Lin, Zhimin Yan, and Jie Chen. Using Impedance Measurements to Characterize Surface Modified with Gold Nanoparticles. *Sensors (Basel, Switzerland)*, 17(9), September 2017.

[180] Christoph Ruppert, Navneet Phogat, Stefan Laufer, Matthias Kohl, and Hans-Peter Deigner. A smartphone readout system for gold nanoparticle-based lateral flow assays: application to monitoring of digoxigenin. *Microchimica Acta*, 186(2):119, January 2019.

[181] José Francisco Bergua, Liming Hu, Celia Fuentes-Chust, Ruslan Álvarez Diduk, Abdelrahim H. A. Hassan, Claudio Parolo, and Arben Merkoçi. Lateral flow device for water fecal pollution assessment: from troubleshooting of its microfluidics using bioluminescence to colorimetric monitoring of generic Escherichia coli. *Lab on a Chip*, 2021.

[182] Jyoti Singh, Shivesh Sharma, and Seema Nara. Nanogold based lateral flow assay for the detection of Salmonella typhi in environmental water samples. *Analytical Methods*, 7(21):9281–9288, 2015. Publisher: Royal Society of Chemistry.

[183] Günter Oberdörster, Vicki Stone, and Ken Donaldson. Toxicology of nanoparticles: A historical perspective. *Nanotoxicology*, 1(1):2–25, January 2007. Publisher: Taylor & Francis.

[184] Margo Hauwaert. Towards electro-chemical characterisation of paper-based sensors and usage perspectives: Responsible water quality sensor design, 2020. Master Thesis, Ecole polytechnique de Louvain, Université catholique de Louvain.

[185] Lia Diagnostics. Meet Lia - The First and Only Flushable and Biodegradable Pregnancy Test, 2021. Meet Lia, https://meetlia.com/, Accessed: 26/04/2021.

[186] Kevin L. Dreher. Health and Environmental Impact of Nanotechnology: Toxicological Assessment of Manufactured Nanoparticles. *Toxicological Sciences*, 77(1):3–5, January 2004.

[187] Laura Brzyski. A Pair of Penn Grads Created a Biodegradable and Flushable Home Pregnancy Test, April 2021. Philadelphia Magazine, https://www.phillymag.com/healthcare-news/2021/04/01/flushable-pregnancy-test-lia/, Accessed 26/04/2021.

[188] Sima Rezvantalab, Natascha Ingrid Drude, Mostafa Keshavarz Moraveji, Nihan Güvener, Emily Kate Koons, Yang Shi, Twan Lammers, and Fabian Kiessling. PLGA-Based Nanoparticles in Cancer Treatment. *Frontiers in Pharmacology*, 9, 2018. Publisher: Frontiers.

[189] M. L Hans and A. M Lowman. Biodegradable nanoparticles for drug delivery and targeting. *Current Opinion in Solid State and Materials Science*, 6(4):319–327, August 2002.

[190] S. Feijoo, S. González-García, Y. Moldes-Diz, C. Vazquez-Vazquez, G. Feijoo, and M. T. Moreira. Comparative life cycle assessment of different synthesis routes of magnetic nanoparticles. *Journal of Cleaner Production*, 143:528–538, February 2017.

[191] Weinan Leng, Pati Paramjeet, and Peter J. Vikesland. Room temperature seed mediated growth of gold nanoparticles: mechanistic investigations and life cycle assesment. *Environmental Science: Nano*, 2(5):440–453, October 2015. Publisher: The Royal Society of Chemistry.

[192] Zoya Javed, Kavya Dashora, Mansi Mishra, Vinayak Fasake, and Ayushi Srivastava. Effect of accumulation of nanoparticles in soil health-a concern on future. *Frontiers in Nanoscience and Nanotechnology*, 5:1–9, November 2019.

[193] Andrew F. Taylor, Elizabeth L. Rylott, Christopher W. N. Anderson, and Neil C. Bruce. Investigating the Toxicity, Uptake, Nanoparticle Formation and Genetic Response of Plants to Gold. *PLOS ONE*, 9(4):e93793, April 2014. Publisher: Public Library of Science.

[194] Mangesh Gharfalkar, Richard Court, Callum Campbell, Zulfiqur Ali, and Graham Hillier. Analysis of waste hierarchy in the European waste directive 2008/98/EC. *Waste Management*, 39:305–313, May 2015.

[195] DCN Diagnostics. Lateral Flow Assay Development, 2021. DCN Diagnostics, https://i.ytimg.com/vi/hp7kGrc8srM/maxresdefault.jpg, Accessed: 01/05/2021.

[196] Vincent Rossi, Nina Cleeve-Edwards, Lars Lundquist, Urs Schenker, Carole Dubois, Sebastien Humbert, and Olivier Jolliet. Life cycle assessment of end-of-life options for two biodegradable packaging materials: sound application of the European waste hierarchy. *Journal of Cleaner Production*, 86:132–145, January 2015.

[197] Wikipedia contributors. Isoelectric point, February 2021. Wikipedia, https://en.wikipedia.org/w/index.php?title=Isoelectric_point&oldid=1009442191, Accessed: 06/04/2021.

[198] Guadalupe Ruiz, Kiran Tripathi, Samuel Okyem, and Jeremy D. Driskell. pH Impacts the Orientation of Antibody Adsorbed onto Gold Nanoparticles. *Bioconjugate Chemistry*, 30(4):1182–1191, April 2019. Publisher: American Chemical Society.

[199] Robert T. Busch, Farzia Karim, John Weis, Yvonne Sun, Chenglong Zhao, and Erick S. Vasquez. Optimization and Structural Stability of Gold Nanoparticle–Antibody Bioconjugates. *ACS Omega*, 4(12):15269–15279, September 2019.

[200] Bio based Industries Joint Undertaking. Homepage, 2021. BBI JU, https://www.bbi.europa.eu/, Accessed: 20/05/2021.

UNIVERSITÉ CATHOLIQUE DE LOUVAIN
École polytechnique de Louvain
Rue Archimède, 1 bte L6.11.01, 1348 Louvain-la-Neuve, Belgique | **www.uclouvain.be/epl**